Acoustic confinement of Escherichia coli : the impact on biofilm formation

Salomé Gutierrez Ramos

To cite this version:

Salomé Gutierrez Ramos. Acoustic confinement of Escherichia coli : the impact on biofilm formation. Physics [physics]. Sorbonne Université, 2018. English. NNT : 2018SORUS599 . tel-02475812

HAL Id: tel-02475812
https://theses.hal.science/tel-02475812v1

Submitted on 12 Feb 2020

THÉSE DE DOCTORAT
DE SORBONNE UNIVERSITÉ

Spécialité: Physique

École doctoral n°564: Physique en Île-de-France

Présentée par:
Salomé Gutiérrez Ramos

sur le sujet:

Acoustic confinement of *Escherichia coli:*
The impact on biofilm formation.

sous la direction de:

Ramiro Godoy Diana

soutenue le 18 Octobre 2018

Devant le jury composé de :

M. Philippe Marmottant	**Rapporteur**
M. Harold Auradou	**Rapporteur**
Mme. Nelly Henry	**Examinatrice**
Mme. Sophie Ramananarivo	**Examinatrice**
M. Jean-Luc Aider	**Invité**
M. Jesús Carlos Ruiz Suaréz	**Invité**
M. Ramiro Godoy Diana	**Directeur de thèse**

It is not the voice that commands the story; it is the ear.

Acknowledgements

“Where is the wisdom we have lost in knowledge?
Where is the knowledge we have lost in information?”

This T.S. Elliot quote has followed me throughout my life, wondering constantly this was my basal state. Luckily, thanks to this work I met the people that gave me the answers.

Dr. Aimee Wessel and Dr. Ramiro Godoy-Diana I lack the words to acknowledge everything that you did for me and this work. Thank you for your academic support, guidance but above all thank you from make me believe in the possibilities of making good science.

Dr. Carlos-Ruiz Suarez thank you for giving me the opportunity to work in your team and letting me collaborate with people at PMMH-ESPCI Paris during these last years. Your support is immeasurable and I deeply appreciate it.

Also, I would like to acknowledge my old and new friends, you acted as a very efficient support system. And above all, to my family.

Finally, I appreciate the economical help provided by CONACYT and the "Aide spécifique aux doctorants boursier" provided by Sorbonne Université.

Acoustic confinement of *Escherichia coli:*
The impact on biofilm formation

Abstract

Brownian or self-propelled particles in aqueous suspensions can be trapped by acoustic fields generated by piezoelectric transducers usually at frequencies in the Megahertz. The obtained confinement allows the study of rich collective behaviours like clustering or spreading dynamics in microgravity-like conditions. The acoustic field induces the levitation of self- propelled particles and provides secondary lateral forces to capture them at nodal planes. Here, we give a step forward in the field of confined active matter, reporting levitation experiments of bacterial suspensions of *Escherichia coli*. Clustering of living bacteria is monitored as a function of time, where different behaviours are clearly distinguished. Upon the removal of the acoustic signal, bacteria rapidly spread, impelled by their own swimming. Trapping of diverse bacteria phenotypes result in irreversible bacteria entanglements and in the formation of free-floating biofilms.

Confinement acoustique de *Escherichia coli:*
L'impact dans la formation de biofilms.

Salomé Gutiérrez Ramos

Résumé

Les particules browniennes ou auto-propulsées dans des suspensions aqueuses peuvent être piégées par des champs acoustiques générés par des transducteurs piézoélectriques, généralement à des fréquences dans le mégahertz. Le confinement obtenu permet d'étudier des comportements collectifs riches tels que la dynamique de regroupement ou d'étalement dans des conditions de type microgravité. Le champ acoustique induit la lévitation des particules autopropulsées et fournit des forces latérales secondaires pour les capturer dans les plans nodaux. Dans cette thèse, nous allons plus loin dans le champ de la matière active confinée, en rapportant des expériences de lévitation de suspensions bactériennes d'*Escherichia coli*. La formation de grappes de bactéries vivantes s'effectue en fonction du temps, où différents comportements sont clairement distingués. Lors de la suppression du signal acoustique, les bactéries se propagent rapidement, entraînées par leur propre nage. Le piégeage de divers phénotypes bactériens entraîne des enchevêtrements irréversibles et la formation de biofilms flottant librement.

Table of contents

List of figures

List of tables

Chapter 1

Introduction

It has been four years since the World Health Organisation warned us of the imminent arrival of *a post-antibiotic era*–in which common infections and minor injuries could kill [1]. This year's reports show that, indeed, this was not an apocalyptic fantasy but rather a twenty-first-century reality [2, 3]. The presence of superbugs (drug-resistant microorganisms) has spread all over Earth; where deaths associated with diseases caused by antibiotic-resistant *Escherichia coli* (*E.coli*) [4, 5], *Pseudomonas aeruginosa* [6], *Mycobacterium tuberculosis* [7] or *Acinetobacter baumannii* [8, 9] are more common than ever.

The emergence of drug-resistant disease is often related to the presence of bacteria that "persist" after an antibiotic treatment (persistent cells) [10, 11]. The persistence phenotype is an epigenetic trait exhibited by a sub-population of bacteria, characterized by slow growth coupled with the ability to survive antibiotics [11, 12]. The phenotype is acquired via a spontaneous, reversible switch between normal and persister cells [10, 13]; it is suggested that the slow division rate of these cells is used in populations of clonal cells as an "insurance policy" against antibiotic encounters [11]. Likewise, the presence of complex bacterial communities affects the effectiveness of antibiotics against bacteria colonisation [14]. Switching to persistent cells or assembling in communities are traits that prove the social behaviours exhibit by bacteria [15–17].

The study of these communal characteristics, have lead to a better understanding of the dynamics of bacteria in more realistic environments [17]. In particular, the understanding of how bacteria transition from a planktonic to a sessile phenotype, organise and develop matrix-enclosed bacterial communities known as biofilms [17], has allowed the description of intricate communication capabilities of bacteria such as quorum sensing, chemotactic signalling and exchange of genetic information [17]. Similarly, it has helped to establish the characterisation of the features that can only emerge collectively during bacteria self-organisation, like sporulation, modification of complex architectures, and the distribution of tasks within the collective [17].

Often without realising it, and even when the term biofilm may not form part of the popular lexicon, people suggest that the general public are familiar with them. For example, Van Leeuwenhoek was the first person to observe the microorganisms (animalcules) constituting dental-biofilms; giving the first description of these bacterial communities and naming them scurfs [18]. Later, in 1940 it was recognised that surface-attached microorganisms exhibit different properties than they do as planktonic cells [19, 20]. Forty years later, J. W. Costerton came up with the term biofilm.

At that moment, the concept of biofilm-related infection and the importance of biofilms in medicine was initiated. Furthermore, the increased antimicrobial resistance of biofilm growing bacteria compared to planktonic growing ones was demonstrated [21].

Whilst there is a plethora of research on this topic, the details of each step involved in biofilm development is not yet well understood. Consequently there is a need of new techniques and approaches to studying them. Just by comparing the different definitions of biofilm that exist in the literature we can see the complexity of this phenomenon; small microbial aggregates [22, 23], small floccules [24], adherent population of bacteria within porous media [25] and bacteria streamers on microfluidic channels are all considered biofilms [26] despite having differences in the genes that are expressed.

The aforementioned examples consider biofilms as a phase separation, that is the formation a of dense cluster from a uniform initial population. Nevertheless, the general consensus in microbiology literature is that a microbial biofilm consists of mature aggregates of bacteria adherent to each other surrounded by a self-produced polymeric matrix with 3-dimensional architecture attached to a surface or present at interfaces [24]. Therefore the fundamental characteristics of biofilms are [27]:

- They form a 3-dimensional structure.
- There is a spatial heterogeneity withing them.
- Biofilms are often permeated by water channels also refereed as their "circulatory system."

- The microorganisms within biofilms exhibit a marked decrease in susceptibility to antimicrobial agents and the host defence system.

Biofilm formation is a dynamic multistage process occurring over a wide range of timescales set by concurrent hydrodynamics, mass transport, and biofilm growth processes [28, 29]. The first step in its formation is mediated by fluid flow, oriented normal or parallel to the surface, that transports planktonic bacteria to the surface by diffusion or advection and generates adhesive or frictional forces between bacteria and surfaces [30, 31]. Once bacteria dynamically or passively approach to surfaces they dramatically modify their gene expression switching from planktonic to a sessile lifestyle [29], increasing the production of appendages that drive surface-associated motility behaviours leading to irreversible attachment to the surface [29, 32].

How bacteria sense surfaces to modify themselves involves one or more mechanical, physical and chemical cues [33]. During this phenotypical transition most of the *Eubacteria* (i.e prokaryotic cells that have specific characteristics like flagella, pilus and asexual reproduction [34]) elongate, increase the number of flagella relative to planktonic cells, as depicted in Figure 1.1, and secrete a wetting agent to have a faster displacement over the surface [35].

For example, *Escherichia coli* elongates to twice its length, increases its mean speed (from $25\ \mu\mathrm{m}/s$ (planktonic cells) to $40\ \mu\mathrm{m}/s$) and reduces its tumbling rate [36]. The swarmer state is the fastest known bacteria mode of surface translocation and enables the rapid colonisation of a nutrient-rich surface or a host tissue [37].

Later, the cells are irreversibly attached to the surface and the local density increases. Next, the formation of bacteria colonies takes place marking the pace of cell-to-cell communication [32, 38] and the expression of the genes involved in the production of polymeric substances composing the extracellular matrix [32, 39]. At this point, the colonies should be considered as bacterial communities with complex dynamics that emerge due to their self-organisation [17].

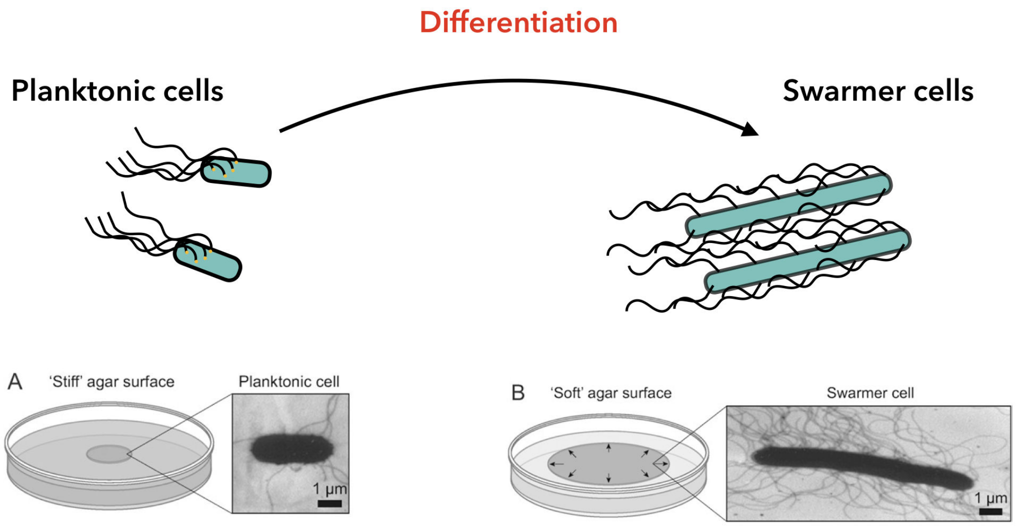

Fig. 1.1 **Differentiation from planktonic to swarmer cells.** Bacteria move by a range of mechanisms. When bacteria are close to a surface they tend to switch from the swimming state (planktonic state) to a swarming state, where bacteria displace in a multicellular manner. During this differentiation cells elongate, the number of flagella on the membrane increases and bacteria tend to secrete a wetting agent. These changes are strain dependant. The electron transmission microscopy (TEM) images show the differentiation of a planktonic *S. liquefaciens* cell (A) into its swarming phenotype (B), we can see that a over-expression of flagella and the elongation of the cells are present. In this case the phenotype change is dependent on the stiffness of the agar surface [35].

Finally, the maturation of these aggregates (colonies) into three-dimensional structures gives rise to a mature biofilm. The cycle restarts after a volume threshold is reached or at certain environmental cues (e.g. depletion of oxygen or lack of nutrients), at this moment some chunks or planktonic cells from the biofilm detached [32]. The growth and decay of mature biofilms are also influenced by fluid flows on the surrounding environment [29, 40].

The established techniques to evaluate biofilm development are summarised in table 1.1. All these techniques use diverse devices that provide a surface and some sort of confinement.

Table 1.1 Biofilm formation devices

Device	Technique	Biofilm type	Reference
Microtiter plates	S	SAB or ALI	[41–43]
Caligary device	S	SAB	[44–46]
Ring test	S	SAB	[47–49]
Robbins device	F	FFB	[50, 51]
Drip-flow reactor	F	SAB	[52, 53]
Rotary reactor	F	SAB	[53, 54]
Flat plate reactor	F	SAB	[55]
Flow chamber	F	FFB	[56]
Microfluidic devices	S/F	SAB or FFB	[26, 57]

Note: S: static. **F:** flow. **SAB:**Surface-attached **FFB:**Free-floating **ALIB:** air-liquid interface.

The coupling of these devices with optical and genetic tools has enabled a tremendous progress in biofilm research [32]. Prompting the elucidation of the genetic pathways, physiological responses or intracellular signal transduction pathways, such as those regulated by cyclic dimeric guanosine monophosphate (d-di-GMP) that underpin biofilm development [54, 58, 59]. In the same manner, these techniques allow focusing on the understanding of interface-biofilms (solid-liquid, liquid-liquid or gas-liquid) and on their eradication [29]. Nevertheless, how bacteria attach to, transport along and interact with the interfaces is not well understood. Microfluidic systems permit the control of diverse environmental settings, allowing to study how transport, attachment, and growth of bacteria and biofilms are modified by medium geometry, fluid flows, shear rate, and surface topology. The confinement provided by these microfluidic devices has enhanced the study of the effects of steady-state flows, and more recently, the study of transient flows and how they affect bacterial behaviour near surfaces and in confinement [60–62]

Collective behaviour of bacteria in confined spaces

Recently, the confinement of bacteria and their use as model organisms in the ever-growing field of *active matter* has afforded the opportunity to study the dynamic assembly and collective motility of living self-propelled agents [63, 64]. Bacteria are low Reynolds number swimmers (Re 10^5) [65] with motion dominated by the viscosity of the fluid in which they swim [66]. The great majority of bacteria swim using one or more flagella, consisting of a passive helical filament connected to a rotary motor. For example, as we will discuss in Chapter 3, *E.coli* bears many flagella, distributed around its body, that assemble into a bundle for swimming and unbundle to re-orient in a different direction [66] as in Figure 1.2. This type of motion is called run-and-tumble and is diffusive at large scale, just like Brownian motion [67, 68].

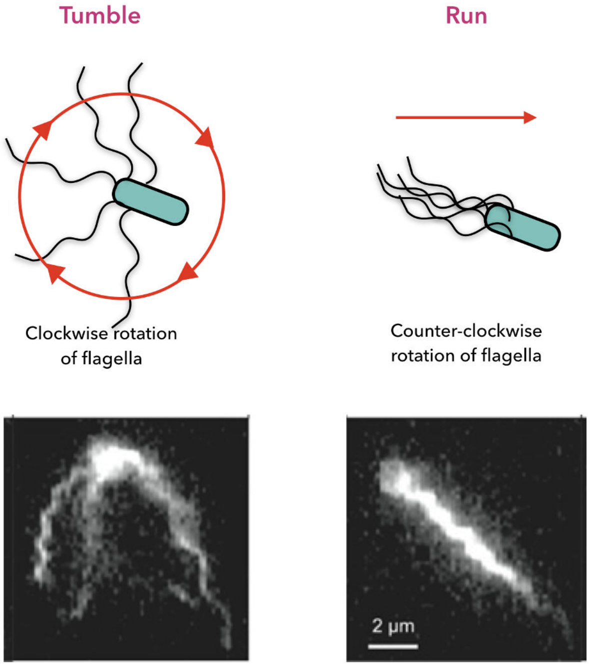

Fig. 1.2 ***Escherichia coli* motion.** Bacteria achieve directional movement by changing the rotation of their flagella. In a cell with peritrichous flagella, the flagella bundle when they rotate in a counter-clockwise direction, resulting in a run. However, when the flagella rotate in a clockwise direction, the flagella are no longer bundled, resulting in tumbles. The fluorescent microscopy images from swimming *E.coli* cells show the cells in the corresponding flagella configuration [69].

However, when bacteria are in a collective, fascinating properties are displayed, which normally originate via the interplay of individual self-propulsion and surfaces, fluid flow and surface interactions or the interaction among other individuals in the group [63, 64].

Typically, bacteria collective motion is studied under confinement with solid walls; using microfluidic chips, agar plates, Hella cells or any recipient with physical walls. More recently, these behaviours have been studied under magnetic or optical confinement using bacteria with specific phenotypes and properties.

Agar substrates

Culturing bacteria on agar plates, evaluating their growth into colonies and analysing their social behaviour is an everyday task in a microbiology lab. The use of this straightforward technique permitted the discovery of the genetic machinery of bacteria, the communication capabilities that enable the self-organisation of complex structured bacteria colonies [63] and their multicellular-organisms-like behaviours [70]. Bacteria within the colonies growing on wet agar surfaces produce a variety of collective motion patterns, see Figure 1.3.

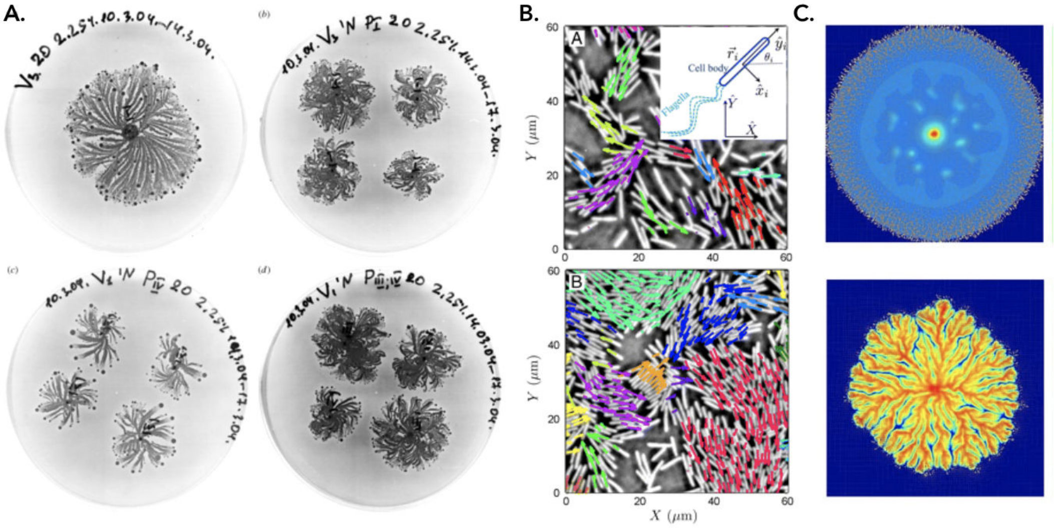

Fig. 1.3 **Collective motion on agar surfaces. A.** Vortices exhibit by *Paenibacillus vortex*. Each plate is inoculated with bacteria that grew on different zones of the mother plate [71]. **B.** Instantaneous configurations at two densities of *Bacillus subtilis*. The velocity vectors are over-layered on the raw images of bacteria. **C.** Two dimensional velocity fields superimposed on color plots of n-vectors, with zero magnitude vectors are represented by a dot [72].

Thin films

One method for observing active bacterial systems is to disperse a bacterial suspension in a free-standing soap with micro-metric thickness and use micron-sized particles to track the flow [73]. Under this configuration, it has been observed that the majority of the bacterial suspension fluid self-organises into an active bacterial-film [74].

Microfluidic chips

There is a myriad of experiments that characterise the orientation of cells in a confined and dense bacterial suspension using microfluidic devices [75–79]. For example, the analysis of dense suspensions of aerobic bacteria confined in a micro-channel showed that the bacteria collective exhibits convective plumes; and on scales much larger than a cell, the presence of high-speed jets straddled by vortex streets produced by the hydrodynamic interactions between swimming cells emerges [80]. Other experiments have enabled the direct measurements of the flow field generated by individual swimming *Escherichia coli* both far from and near to a solid surface. Also, the quantification of cell-cell interactions and its link with the assemblages of bio-filaments, and flocks [81]. The emergence of self-sustained mesoscale turbulence-like motion dominated by short-range interactions [82] and the existence of a transition from quasi-two-dimensional collective swimming to three-dimensional turbulent behaviour have been described [75, 83–85]. Additionally, the presence of the alignment of neighbouring bacteria (*Bacillus subtilis*) in nearly close-packed populations has been observed, and named "Zooming BioNematic" (ZBN) in analogy to the molecular alignment of nematic liquid crystals [86].

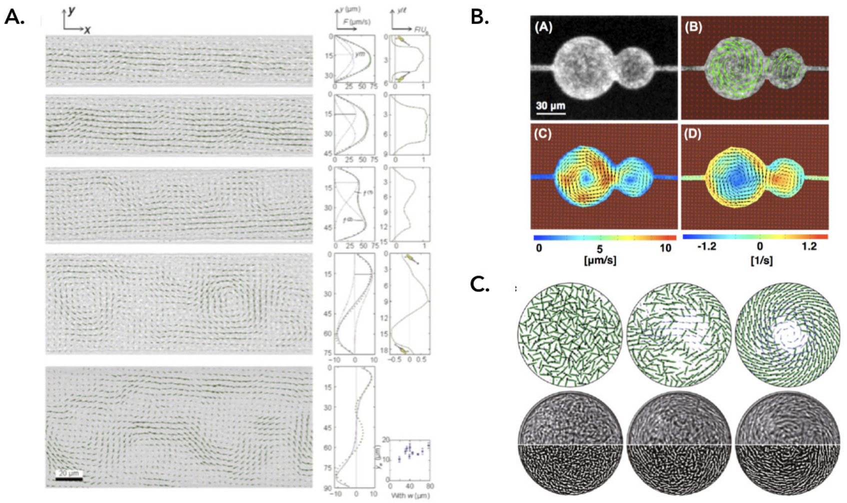

Fig. 1.4 **Fluid flows created by swimming bacteria in confined suspensions. A.** Wioland et al. experimental work demonstrated that the flow behaviour of an active bacterial suspension can be controlled by tuning the length scale at which bacteria are confined [85]. **B.** The geometry of confinement controls the emergent collective dynamics in bacteria suspensions [76]. **C.** Self-organization from simulations (green) and experiments with *Bacillus subtilis* dense suspensions [80].

Magnetic traps

Confining magnetotactic bacteria has provided information about the rheology of the system as a function of the magnetic field applied. It has been shown that in the limit of low shear rate, the rheology exhibits a constant shear stress, called actuated stress, which depends on the swimming activity of the particles and its induced by the magnetic field and it can be positive (brake state) or negative (motor state) [87]. Some other experiments showed that these bacteria can produce magnetic crystals that align with the external magnetic field. Also, at denser suspensions the increased interaction between magnetotactic bacteria alters the ability of an individual cell to align with an applied magnetic field [88].

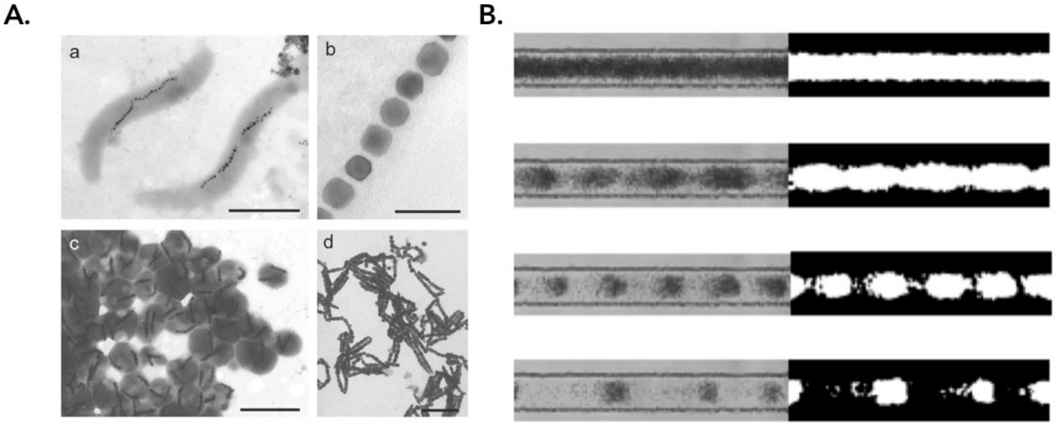

Fig. 1.5 **Collective motion mediated by magnetic fields. A.** Magnetotactic bacteria orient themselves and move along magnetic field lines. This positioning is possible because of the presence of magnetosomes, small organelles of magnetic iron material wrapped in a membrane. The alignment of the magnetosomes as a response to the magnetic field creates bacterial crystals [88]. **B.** Segregation of a magnetic bacteria flow in a microchannel due to the impose magnetic field.

The aforementioned techniques provide confinement and surfaces where bacteria can easily attach, and by varying the distance between walls (plates) the density of bacteria can be locally increased [89]. All of them are used to study arising collective behaviours of bacteria communities and could be used to study the transition to biofilm development on a long timescale [75, 83–85].

In this work, we addressed the feasibility of enhancing biofilm formation in a surface-less environment. Taking advantage of a relatively new confinement technique called acoustic levitation [90–92] we are able to levitate bacteria at a pressure node and confine them to form stable aggregates. The fact that acoustic levitation allows us to evaluate bacteria biofilm development without surface adherent cells as nucleation points is exciting as it changes the canonical model of biofilm development, that establishes the need of adhesion to surfaces or small cluster as nucleation points.

Acoustic trapping in levitation is defined as the immobilisation of particles and cells in the node (or antinode) of an ultrasonic standing wave field. It is a gentle way of performing contact-less manipulation [93, 94] inside cavities or other small confined spaces, creating pressure nodes that attract and hold particles and cells [95]. Commonly, acoustic frequencies in the MHz-range and structures in the range of a couple of 100 μm are used. The manipulation of the entities relies on their acoustic properties such as density and compressibility. This provides a robust technique that could manipulate basically any particle [94, 96]. The technique has already been used to trap latex beads [97], cancer cells [98], Janus particles [96] and even suspension of beads and bacteria [99]. Also, several studies have shown that ultrasonic levitation does not have any negative effects on living cells. Hultström et al. cultured cells that had been levitated for over an hour and studied the doubling times of the cells and no direct or delayed damage could be detected on them [95, 100]. Also, Bazou et al. performed studies on mouse embryonic stem cells and confirmed that they could see no changes in gene expression after ultrasonic treatments up to one hour and the cells maintained their pluripotency [98].

It is then evident that acoustic trapping can provide confinement of suspensions in a surface-less environment that is also biocompatible. The main goal of this work is to test this technique, which could become the best, to evaluate biofilm development with no surface-adhered cells as a starting point.

In the following Chapter, we described in detail the theory behind the acoustic trapping technique and the considerations that we took in the design and fabrication of the acoustic trap. We present the characterisation of the device and its ability to trap both beads and bacterial cells. Later, on Chapter 3, we present the details of the model strains of *Escherichia coli* we used to evaluate the clustering process that leads to a confinement of cells in levitation, followed by the disintegration processes of the floating bacteria clusters. We evaluated these processes for both motile and non-motile phenotypes of *Escherichia coli*, and conclude that self-propulsion affects the disintegration of the clusters. Also, it was noted that under the confinement in levitating conditions motile bacteria exhibited a turbulent-like behaviour within the cluster, whereas non-motile bacteria did not. This behaviour is characterised by probing the mean kinetic energy and the enstrophy within a floating cluster.

Finally, with guidance from our results in Chapter 3 we present experiments on forming floating biofilm-like structures. To do so we used two different strains of motile *Escherichia coli*; one carrying a mutation on the allele ompR234 resulting in an increase in CsgA proteins levels, therefore, promoting biofilm formation and the other with a knock-out of the same allele. The results, presented in Chapter 4, show that is possible to form floating biofilm-like structures that present phenotype-dependent characteristics.

Chapter 2

Acoustic confinement in levitation

Acoustic waves can exert forces on small particles, a fact that was discovered by August Kundt and presented as a way to measure the speed of sound in gaseous medium [101]. More than one hundred years later, in 1971, this effect was observed for biological particles in a liquid media. Dyson et al. [102] and later Baker et al. [103] reported red blood cells bands that appeared after their exposure to ultrasound. Today, this phenomenon is utilized primarily for air-levitators, where small droplets or particles can be held in air without contact [104], separation of bioparticles in a flow via *acoustophoresis*, as well as the capture and retention of cells or microparticles in fluids through acoustic trapping.

Acoustic trapping is based on the use of mechanical waves to manipulate particles, the parameters that allow their manipulation are density and compressibility–from the particles and the fluid. It is clear that the long wavelength, in the millimeter range, is an advantage as it allows capturing large groups of particles and also provides their capture and retention confining them away from the surface [94].

At this moment, there are several micro-systems used for acoustic trapping with a plethora of biological and non-biological applications [105, 106]. Nevertheless, the fact that these systems are complex and functional labs-on-a-chip does not imply that they are the only or most robust acoustic trapping systems. Therein, an emblematic acoustic trapping system is the multi-layered or planar resonator. The planar resonator is a vertical structure with three wavelength-matched layers (i.e. the layers should have an acoustic impedance and thickness that depends on the acoustic wavelength) [107]. The coupling layer, on the bottom of the resonator, provides efficient transmission of the waves from the piezo-ceramic transducer into the next layer of the system. The cavity or fluid layer is where the trapping of particles or cells takes place, on top of it a reflecting layer is placed to reflect the transmitted waves and avoid their dispersion. By using operational frequencies in the order of MHz and single or multiple nodes, the fluid layer can be scaled down sufficiently to allow laminar flow conditions inside the cavity of the system, as in the design pioneered by Bazou et al. [98]

One of the key goals of this thesis is to design and fabricate a trapping system based on acoustic resonances. Throughout this Chapter, an introduction to the theory behind these systems is presented, followed by the specifics of the design, fabrication and characterisation.

2.1 Acoustofluidics

Acoustofluidics is the linkage of ultrasonic waves with microfluidic systems to manipulate fluids and particles in the micro scale. In the 1930s a key study of incompressible particles in acoustic fields was published [108] and twenty years later, the forces on compressible particles in plane acoustic waves were calculated by Yosioka and Kawasima [109]. Later, these works were admirably summarized and generalized in a short paper by Gorkov [110]. At the beginning of the 1980s, a lot of work had appeared discussing the utility of acoustic waves to trap and transport passive systems. Unfortunately, as so often happens in science, the idea was left behind to experience a revival in the early 2000s, with what is known as *acoustofluidics*. After the new term was coined [94], seminal works from Coakley [111–114], Laurell [115, 116] and Bruus [117, 118] appeared, providing a detailed mathematical and experimental verification of how ultrasonic waves are applicable in microfluidics.

The main idea is that the wavelength (λ) generated by the coupling of the ultrasonic frequencies (f), in the low MHz-range, and the speed of sound in water c_w is typically less than 1 mm. For that reason, it may fit submillimetric cavities and result in the formation of resonance modes. Accordingly, it has been proved that it is advantageous to operate an acoustofluidic device in its acoustic resonances [119], as they are stable, reproducible, and the spatial patterns are controlled by the geometry of the device. Moreover, the maximum acoustic power released by the piezo-ceramic transducer to the system arises in resonant systems, where it results in the emergence of acoustic radiation forces and acoustic streaming [115, 119].

2.1.1 Acoustic waves

Acoustic waves are mechanical and longitudinal waves, i.e. same direction of vibration as the direction of propagation, that result from an oscillation of pressure that travels through a solid, liquid or gas in a wave pattern. They can be characterized by their wavelength $\lambda = v/f$ that depends on the media in which the wave is propagating, their frequency f, period $T = 1/f$ and amplitude. The acoustic wave is defined using a field that describes either the displacement itself ξ, the velocity of the displacement $\mathbf{v}$, the scalar velocity potential Φ such that $\vec{v} = \vec{\nabla}\Phi$, or the pressure changes p associated with displacing the matter. Regardless of which aspect is used to describe the acoustic wave, it will obey the wave equation, that for velocity is:

$$\frac{\partial^2 \mathbf{v}}{\partial^2 t} = c_0^2 \nabla \mathbf{v} \tag{2.1}$$

Here, c_0 is the speed of sound as it couples the change in position to the change in time. The speed of sound is a material-dependent parameter and can be found from the compressibility κ and the density ρ of the media using the following relation:

$$c_0 = \frac{1}{\sqrt{\kappa\rho}} \tag{2.2}$$

2.1.2 Acoustic waves interaction with suspensions

The linear wave equation for the acoustic field in a fluid can be derived using a first order perturbation theory. We recall here the derivation of Bruus [120] where the acoustic field is derived based on an equation of state describing pressure p in terms of density ρ (equation 2.3), the kinematic continuity equation for the density (equation 2.4), and the dynamic Navier-Stokes equation for the velocity $\mathbf{v}$ (equation 2.5):

$$p = p(\rho), \tag{2.3}$$

$$\partial_t \rho = -\nabla \cdot (\rho \mathbf{v}), \tag{2.4}$$

$$\rho \partial_t \mathbf{v} = -\nabla p - \rho(\mathbf{v} \cdot \nabla)\mathbf{v} + \eta \nabla^2 \mathbf{v} + \beta \eta \nabla(\nabla \cdot \mathbf{v}). \tag{2.5}$$

In the first order perturbation theory, a quiescent liquid with constant density ρ_0 and pressure p_0 is considered. At a given time, the fluid is disturbed by an acoustic wave-front and the small perturbations in the density, velocity and pressure fields are described respectively by:

$$\rho = \rho_0 + \rho_1, \quad p = p_0 + c_0^2 \rho_1 \quad \text{and} \quad \mathbf{v} = v_1. \tag{2.6}$$

Later, when the equation of state is derived, it has the dimension of a squared velocity c_0^2, where c_0 is considered as the speed of sound in the fluid. Using the previous equations, and neglecting the products of the first-order terms, the first-order continuity and Navier-Stokes equations are:

$$\partial_t \rho_1 = -\rho_0 \nabla \cdot v_1, \tag{2.7}$$

$$\rho_0 \partial_t v_1 = -c_0^2 \nabla \rho_1 + \eta \nabla^2 v_1 + \beta \eta \nabla(\nabla \cdot v_1) \tag{2.8}$$

Following Bruus [120] we assume that there is a harmonic dependence in all fields, such that:

$$\rho_1(r,t) = \rho_1(r) e^{-i\omega t}, \quad p_1(r,t) = c_0^2 \rho_1(r) e^{-i\omega t} \quad \text{and} \quad v_1(r,t) = v_1(r) e^{-i\omega t}, \tag{2.9}$$

with $\omega = 2\pi f$ as the angular frequency and, as stated before, f the frequency of the acoustic field. Inserting equation 2.15 into equation 2.7- 2.8 the equation of pressure is:

$$\nabla^2 p_1 = -k^2 p_1, \tag{2.10}$$

with k the complex wave-number given by:

$$k = (1 + i\gamma)k_0 = (1 + i\gamma)\frac{\omega}{c_0}. \tag{2.11}$$

On this manner, equation 2.10 is the Helmholtz equation for a damped wave with wave-number k and angular frequency ω. Since the damping factor is $\gamma \ll 1$ the viscosity on the bulk part of the acoustic wave is neglected, hence, the wave equation becomes:

$$\nabla^2 p_1 = \frac{1}{c_0^2}\partial_t^2 p_1. \tag{2.12}$$

This equation shows that a pressure perturbation propagates a distance $\pm c_0 t$ in a time t, therefore c_0 is indeed the speed of sound.

To assess the slowly evolving phenomena that arise due to acoustic waves it is necessary to use the second-order perturbation theory. According to this theory, the processes are governed by time-averaged fields, where the temporal averages of the first order fields are zero and an expansion in equations is needed:

$$\rho_0 \nabla \cdot \langle v_2 \rangle = -\nabla \cdot \langle \rho_1 v_1 \rangle, \tag{2.13}$$

$$\eta \nabla^2 \langle v_2 \rangle + \beta \eta \nabla(\nabla \cdot \langle v_2 \rangle) - \nabla \langle p_2 \rangle = \langle \rho_1 \partial_t v_1 \rangle + \rho_0 \langle (v_1 \cdot \nabla) v_1 \rangle. \tag{2.14}$$

The time-averaged second-order fields will, in general, be non-zero because of the time-averaged products of first-order terms acting as source terms on the right-side of the governing equations. It is important to emphasize that, physically, the non-zero velocity $\langle v_2 \rangle$ is the so-called acoustic streaming [121] and that from the non-zero pressure $\langle p_2 \rangle$ arises the acoustic radiation force. The acoustic radiation force emerges from the scattering of acoustic waves causing *acoustophoretic* motion of the particles [120].

2.1.3 Resonance modes

In a geometry confined by boundary conditions, the wave equation has *Eigenmodes*, corresponding to the pattern in the acoustic field that repeats over time, and *Eigenvalues*, that are associated with the repetition frequency. If the system is supplied with a matched frequency to the repeating patterns in the acoustic field, more energy can be added to the system–thereby creating a resonating system.

In other words, acoustic resonances occur for certain specific frequencies ω_j, j=1,2,3,(...) An acoustic resonance at a given ω_j is a state where the average acoustic energy density ($< E_{ac} >$) inside the cavity is several orders of magnitude larger than at other frequencies. By tuning the applied frequency to one of these resonance frequencies, the acoustic forces become strong enough to enable particle manipulation. The values of the frequencies depend on the geometry of the acoustic cavity and on the material of the layers and the fluid parameters.

The most relevant parameters are the speed of sound in the media c_0, the density of the media ρ_0 and, in the same manner, of the material composing the cavity. The amplitude of a resonance field, at a given actuation, is determined by the amount of energy that can be stored in the mode and transferred to the system. This is determined by the attenuation of the system and the coupling of the source of actuation.

In idealized systems, e.g. simulation, it is feasible to calculate possible modes for a given geometry and the use of experimental data makes predictions more accurate [122–124]. Also, there are *in silico* or experimental techniques to measure the acoustic field, such as the use of hydrophones [125]; but on closed systems a suitable method to measure these properties directly has not yet been invented. However, the acoustic field can be measured indirectly using the movement of particles coupling particle tracking velocimetry (PTV) in combination with mathematical models [126] as in Figure 2.1.

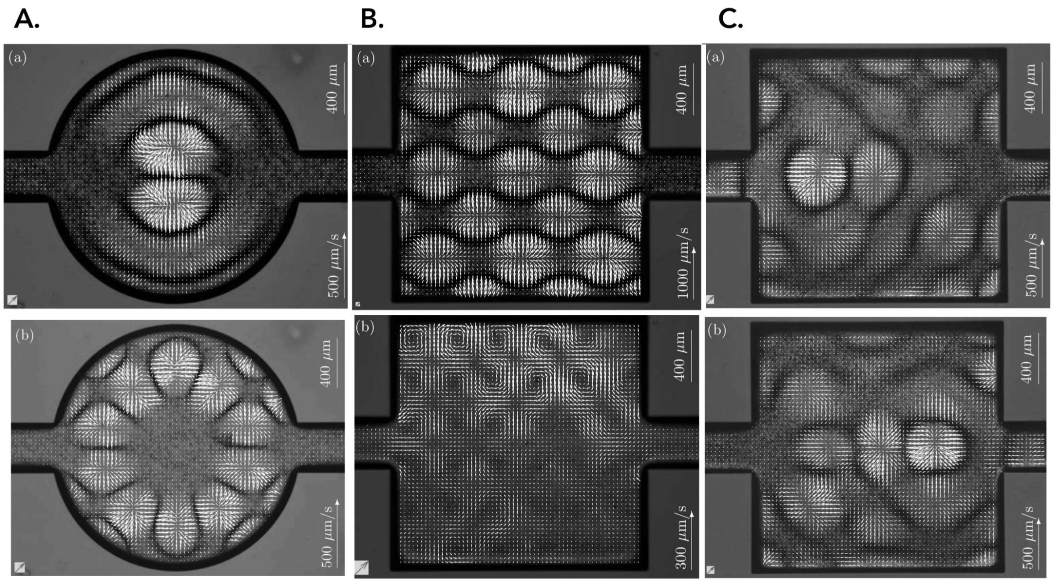

Fig. 2.1 **Acoustic resonances in microfluidic chips.** Three sets of experiments performed by Hagsater et al. [126] **(A.)** Experiments with 5 μm beads at 1.936 MHz acoustic resonance. The white vectors indicate the initial bead velocities pointing away from pressure anti-nodes immediately after the piezo-actuation is applied. On the bottom, the distribution of the beads on a different acoustic resonance is depicted. **(B.)** The acoustic and radiation forces at a 2.7 MHZ resonance show that with 5 μm particles (top) acoustic streaming can be neglected, whereas for 1 μm (bottom) it overcomes acoustic forces and the particles act as tracers of the flow. **(C.)** Experiments with 5 μm beads show that the geometry asymmetries on the micro-devices can change completely the energy distribution for different acoustic resonances.

2.1.4 Acoustic radiation force on small particles

A spherical micron-sized particle with radius $a \ll \lambda$, density ρ_p and compressibility κ_p suspended in an inviscid fluid with density ρ_0 and compressibility κ_0 under the influence of an ultrasonic field of wavelength λ, will act as a weak point-scatterer of acoustic waves. The incoming wave described by a velocity potential ϕ_{in} will result in a scattered wave ϕ_{sc} propagating away from the particle as depicted in 2.2. As a result, the total first order acoustic field ϕ_1 is the sum of the two and it is valid for weak incoming and scattered waves.

Mathematically we have:

$$\phi_1 = \phi_{in} + \phi_{sc}, \tag{2.15}$$

$$v_1 = \nabla\phi_1 = \nabla\phi_{in} + \nabla\phi_{sc}, \tag{2.16}$$

$$p_1 = i\rho_0\omega\phi_1 = i\rho_0\omega\phi_{in} + i\rho_0\omega\phi_{sc}. \tag{2.17}$$

Once the first-order scattered field by a given incoming field is calculated, the acoustic radiation force F^{rad} on the particle is determined by the surface integral of the time-averaged second-order pressure p_2 and a momentum flux tensor $\rho\langle v_1 v_1\rangle$ at a fixed surface outside the oscillating sphere, represented by the yellow arrows in Figure 2.2. The expression for the radiation force becomes [120]:

$$F^{rad} = -\int_{\delta\Omega} da\,\{\langle p_2\rangle \mathbf{n} + \rho_0\langle(\mathbf{n}\cdot v_1)v_1\rangle\} \tag{2.18}$$

$$= -\int_{\delta\Omega} da \left\{ \left[\frac{1}{2}\kappa_0\langle p_1^2\rangle - \frac{1}{2}\rho_0\langle v_1^2\rangle\right] \mathbf{n} + \rho_0\langle(\mathbf{n}\cdot v_1)\, v_1\rangle \right\}, \tag{2.19}$$

where **n** is a unit vector pointing outwards perpendicular to the element of an area *da*.

In this problem there are no body forces, thus, any fixed surface $\partial\Omega$ encompassing the spherical particle experiences the same force. To derive the rest of the equations, scattering theory is used; for a detailed description of this, see [127]. The scattered field ϕ_{sc} from a point scatterer (particle) at the centre of the system is represented by a time-retarded multi-pole expansion. In the far field region, the monopole (ϕ_{mp}) and dipole (ϕ_{dp}) components dominate and according to the first-order scattering theory ϕ_{sc} the field must be proportional to the incoming field ϕ_{in}.

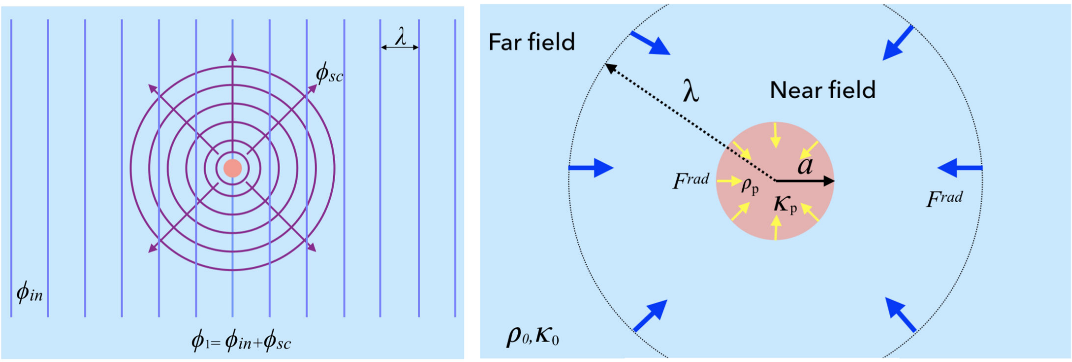

Fig. 2.2 **Acoustic radiation force.** On the left, a sketch of the far-field region $r \ll \lambda$ of an incoming acoustic wave ϕ_{in} (vertical purple line) of wavelength λ scattering off a small particle (pink dot) with radius $a \ll \lambda$, prompting the outgoing scattered wave ϕ_{sc} (purple circles and arrows). The resulting first-order wave is $\phi_1 = \phi_{in} + \phi_{sc}$. On the right it is shown a compressible spherical particle (pink) of radius a, compressibility κ_p, and density ρ_p, surrounded by the compressible inviscid bulk fluid of compressibility κ_0 and density ρ_0. The fluid is divided into the near-field region for $r \ll \lambda$, with the instantaneous field $\phi_{sc}(t)$, and the far-field region with the time-retarded field $\phi_{sc}(t - \frac{r}{c_0})$. The radiation force, F^{rad} (blue arrows), evaluated at any surface in the far-field region (dashed circle), equals that evaluated at the surface of the sphere (yellow arrows) [120].

The implementation of the scattering theory allows the radiation force to be expressed in terms of the incoming acoustic wave evaluated at the particle position and can be used to derive two complex scattering coefficients f_1 and f_2 that represent, respectively, a monopolar scattering due to the presence of a compressible particle, and a dipolar scattering related to the translation of the particle. Thus f_2 depends on the viscosity of the fluid. Thanks to this implementation, the equation for the radiation force acting on a small particle $(a \gg \lambda)$ is:

$$F^{rad} = -\frac{4\pi}{3} a^3 \nabla \left[\frac{1}{2} \mathrm{Re}[f_1] \kappa_0 \left\langle p_{in}^2 \right\rangle - \frac{3}{4} \mathrm{Re}[f_2] \rho_0 \left\langle v_{in}^2 \right\rangle \right], \tag{2.20}$$

with:

$$f_1(\tilde{\kappa}) = 1 - \frac{\kappa_p}{\kappa_0} \tag{2.21}$$

$$f_2(\tilde{\rho}) = \frac{2(\rho - 1)}{\rho + 1}. \tag{2.22}$$

In summary, the resulting radiation force F^{rad} on a small, spherical particle in an inviscid fluid is the gradient of an acoustic potential:

$$F^{rad} = -\nabla U^{rad}. \tag{2.23}$$

In the case of a 1D planar standing $\lambda/2$-wave with, $p_1(z) = p_a \cos(kz)$ where: $k = 2\pi/\lambda = \omega/c_0$ and $w = \lambda/2$ being w the channel width, the radiation force from such field is given by:

$$F_z^{rad} = 4\pi\Phi(\kappa, \rho) k a^3 E_{ac} \sin(2kz), \tag{2.24}$$

where E_{ac} the acoustic energy density is:

$$E_{ac} = \frac{P_a^2}{4\rho_0 c_0^2}, \tag{2.25}$$

and the so-called acoustophoretic contrast factor:

$$\Phi(\tilde{\kappa}, \tilde{\rho}) = \frac{1}{3}\left[\frac{5\tilde{\rho} - 2}{2\tilde{\rho} + 1} - \tilde{\kappa}\right]. \tag{2.26}$$

2.1.5 Energy density in a piezo-transducer

In applications of the acoustic radiation force in trapping systems is important to remember the linear relation that exists between the applied peak-to-peak voltage U_{pp}, that produces the ultrasonic resonances and induce acoustic pressure amplitude p_a, and the acoustic energy density that is generated.

By tracking the y-position over time of polystyrene micro-beads Barnkob et al. [117] showed that at a fixed driving frequency ($f = 1.99 MHz$) the acoustic energy density (E_{ac}) as a function of the peak-to-peak value U_{pp} (0.5-1.9 V) scales as a power law of the form $E_{ac} \propto (U_{pp}^{2.07})$ as depicted in Figure 2.3. This is close to the power law of two, which is expected since the acoustic pressure delivered by the piezo-transducer is proportional to the applied voltage and, the acoustic energy density proportional to the square of the pressure [119, 128]:

$$E_{ac} \propto p_a^2 \propto U_{pp}^2 \tag{2.27}$$

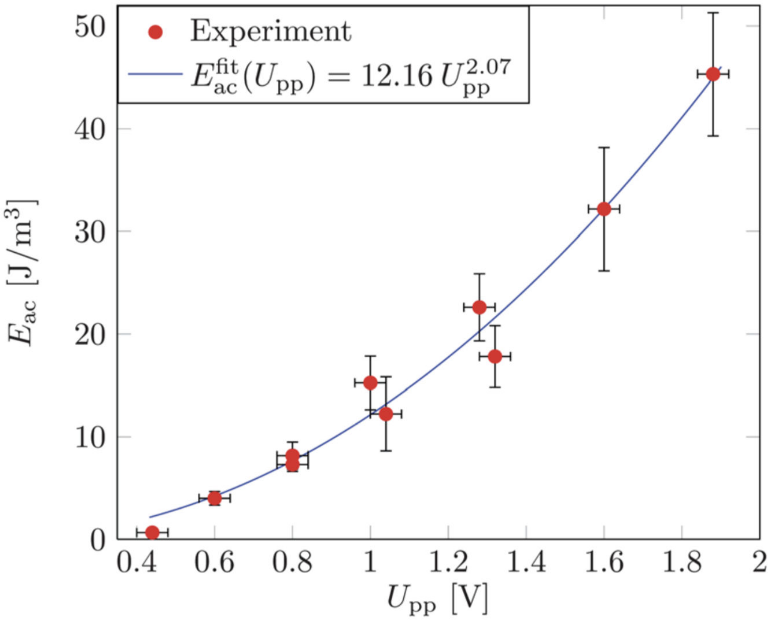

Fig. 2.3 Measured acoustic energy density E_{ac} versus applied peak-to-peak voltage U_{pp} on the piezo -transducer (points) for $\alpha = 1$. A power law fit (full line) to the data is close to the expected square law, $E_{ac} \propto U_{pp}^2$. From this figure, Barnkob et al. [117] were able to extract reliable values for E_{ac} which in this case was found to be 6.69 J/m^3

2.1.6 Secondary radiation force

The secondary radiation force–also known as Bjerkness force when acting on gas bubbles or Köning forces when acting on solid particles–is an inter-particle force [129]. It can be attractive or repulsive and depends on the distance between particles. In addition, its amplitude is two orders of magnitude smaller than the primary radiation force (F^{rad}). We already discussed that a particle acts as a scattering point, hence, the acoustic waves coming from the emitter will scatter in all the particles on the suspension. The secondary force in the case of a plane wave incident field in a suspension is given by [130]:

$$F_{sec} = 4\pi a^6 \left[\frac{(\rho_p - \rho)^2 (3\cos^2\theta - 1)}{6\rho d^4} v^2(x) - \frac{\omega^2 \rho (\kappa_p - \kappa)^2}{9d^2} p^2(x) \right]. \tag{2.28}$$

Here ω is the angular frequency, d is the distance between particles (centre-centre) and θ is the angle between the axis of the incident wave and the centre-line connecting the two particles.

This definition of the force is such that a negative sign should be interpreted as an attractive force between the particles [131]. The secondary radiation force scales heavily with the distance between the particles as the magnitude drops off so rapidly with particle spacing, the effects of the secondary radiation force can be ignored in many cases. Nevertheless, when particles are trapped in a tight cluster the force has a significant contribution [132].

Interestingly, the secondary radiation force has two terms; one that is always attractive, and one that is angle-dependent. As the angle-dependent term decreases faster with the distance between particles there will be an equilibrium-distance to which a particle is drawn. The equilibrium distance will be angle dependent, such that at some angles the particles will tend to be as close as possible, whereas at other angles a small separation will be preferential. While the formula for the force is given for two identical particles, in reality, there will be, of course, secondary forces between particles with different sizes and properties [133].

2.1.7 Acoustic streaming

The acoustic field imposed on a suspension will not only create forces on the particles but it will also create forces on the media itself. This phenomenon is called acoustic streaming, and it is defined as the generation of fluid flows by sound. Here, the sound plays the leading role and the flow is a by-product [121]. Furthermore, acoustic flow generation shows features symmetrical with those of aerodynamic sound generation, i.e. not only can a jet generate sound, but also sound can generate a jet.

The first theoretical model to thoroughly describe acoustic streaming flows was derived by Rayleigh in 1884 [134]. In his work, Rayleigh treats the cases of streaming that were observed experimentally by Faraday [135] and Dvorak [136]. Two cases of streaming that were observed by Faraday are related to the observations on the patterns assumed by sand and fine powders on Chladni's vibrating plates [137]. Also, Rayleigh analysed Dvorak's observations which consisted on the circulation of air currents in a Kundt's tube [134, 135].

Streaming flows vary greatly depending on the mechanism behind the attenuation of the acoustic wave. The variations include the velocity of the flow, the length scale of the flow and the geometry of the same. The velocity variation could be from being on the order of mm, as in the case of slow streaming, up to velocities on the order of cm or more for fast streaming. For example, in the case of microstreaming the length scale variations are in the order of mm, whereas in bulk streaming up to the order of cm where the flow geometry may take the form of a jet or of vortices [138].

Another example is the boundary-layer driven acoustic streaming. This type of streaming is formed by the viscous dissipation of the acoustic energy into the boundary layer of a fluid along any solid boundary that has a length greater (in the direction of acoustic propagation) than a quarter of the acoustic wavelength [139]. In addition, the streaming flow is typically observed in fluid cavities where at least one dimension, perpendicular to the direction of acoustic propagation, is comparable in size to the acoustic wavelength.

The main types of streaming flows that have been described in the literature can be classified as:

i. Schlichting streaming. Described as the viscous dissipation that results in a steady momentum flux that arises in a system that has a standing wave parallel to the surface. It is typically oriented from the pressure anti-nodes to the pressure nodes close to the solid boundary, see Figure 2.4A [140].

ii. Rayleigh streaming This type of streaming, depicted in Figure 2.4A, appears once Schlichting streaming is established. The powerful inner boundary layer streaming flow generates counter rotating streaming vortices within the bulk of the fluid [134].

iii. Eckart streaming. Formerly called "quartz wind" is the flow formed by the dissipation of acoustic energy into the bulk of a fluid, as seen in Figure 2.4B. As an acoustic wave propagates through a fluid, a part of the acoustic energy is absorbed by the fluid at a rate proportional to the square of its frequency. The amplitude of the acoustic wave becomes attenuated causing the acoustic pressure amplitude to decrease with distance from the acoustic source [138]. The loss of acoustic energy results in a steady momentum flux, forming a jet of fluid inside the acoustic beam in the direction of the acoustic propagation. When a fluid jet is formed within the confinement of a micro chamber vorticity ensue, resulting in a fluid circulation either within the entire chamber or just on a specific region [138]. Matsuda, Kamakura and Maezawa showed that the Eckart streaming will only take place in microfluidic devices when high-frequency ultrasound is propagated along a dimension on the order of a millimetre long [141].

iv. Cavitation microstreaming. This particular form of boundary-layer-induced streaming arises by the viscous dissipation of acoustic energy in the boundary layer of a stable oscillating microbubble [142]. The forced oscillation of microbubbles, sonicated at or near their resonance frequencies, results in the local amplification of the first order velocity [139]. It is an altogether different concept from that of a fluid jet formed by the destructive cavitation of a bubble, which despite being an acoustically induced flow is not a form of acoustic streaming, see Figure 2.4C [138, 139].

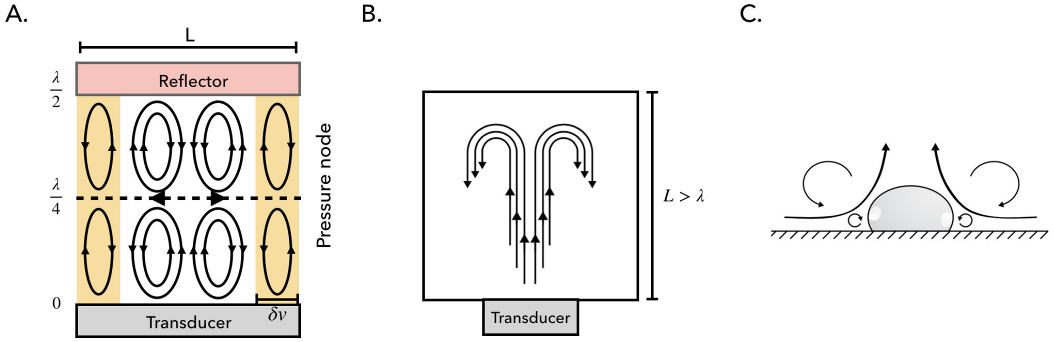

Fig. 2.4 **Types of streaming described in literature A.** A $\frac{\lambda}{2}$ resonator with inner Schlichting boundary layer streaming within the viscous boundary layer (yellow regions) with thickness δv and outer (Rayleigh) boundary layer streaming within the bulk of the fluid (white region). In the plane of the pressure node, the outer boundary layer streaming is directed outwards counteracting the lateral component of F^{rad}. **B.** Eckart streaming in a resonator much larger than the wavelength ($L > \lambda$). The forward streaming jet induces backflow typical for Eckart streaming. [143] **C.** Cavitation microstreaming due to spherical volume oscillations of a gas bubble resting on a solid boundary. Here the cross-section through the centre of the bubble is shown. Due to the hemi-spherical shape of the bubble only half of the typical streaming pattern is formed [144].

As we can see, acoustic streaming is a well-known phenomenon that depends on the geometry of the cavity where arises (see Figure 2.5). Nevertheless, due to its many forms, it is often considered a nuisance since it is present inside many acoustically driven microfluidic devices where it could be counter-productive. While in some cases it is indeed a problematic phenomenon [145–147], when used correctly it can be very useful and could help overcoming some of the challenges presented by low Reynolds number flows in microfluidics [138, 143].

Rayleigh streaming plays an important role on half-wavelength chambers setting a lower limit on the particle size that can be manipulated by the primary radiation force in a standing wave [138]. This is particularly relevant when the streaming direction is opposite to the direction of the radiation force. For example, Spengler et al. [148] observed that whilst larger (10 µm) particles became agglomerated in the centre of the pressure nodal plane, smaller particles of the order of one micrometre did not, as the drag from the streaming flow overcame the lateral radiation force. Later, it was shown that beads of intermediate size are able to overcome the drag from Rayleigh streaming only after they have formed mini-aggregates off-axis at the edges of the acoustic fields, implying that the depletion of beads in that plane is caused by the increase of the effective volume of the mini-aggregates relative to single beads [99]. Therefore, the increase in volume has a stronger effect on the volume-dependent radiation force than on the radius-dependent viscous drag from acoustic streaming [148–150].

In addition, Martin and Minor found that an increase either on the frequency or pressure amplitude resulted in an increase of the streaming velocity, whereas halving the chamber thickness (to obtain a $\frac{1}{4}\lambda$ resonance) had as a consequence a reduced streaming velocity [151]. Posterior to this, a more detailed analysis of the size-dependent cross-over from radiation force dominance to streaming dominance was carried out by Barnkob et al. [117] see Figure 2.5.

They concluded that the theoretical threshold, based on experimental data, defined as the particle size for which the two forces were equal in magnitude, corresponds to a particle with diameter of 2.6 µm at a driving frequency of 2 MHz. Also they found that the threshold particle size is proportional to $\frac{1}{\sqrt{f}}$, where f is the driving frequency [152].

As discussed before Eckart streaming is not the dominant form of acoustic streaming observed in microfluidic devices, however, if the dimensions of the channel, or chamber, parallel to the propagation direction of the acoustic wave are of scale > 1 mm it may occur. When it comes to cavitation micro-streaming, typical applications are the generation of whole scale flows and the generation of highly targeted flows used in micromixing and cell membrane sonoporation.

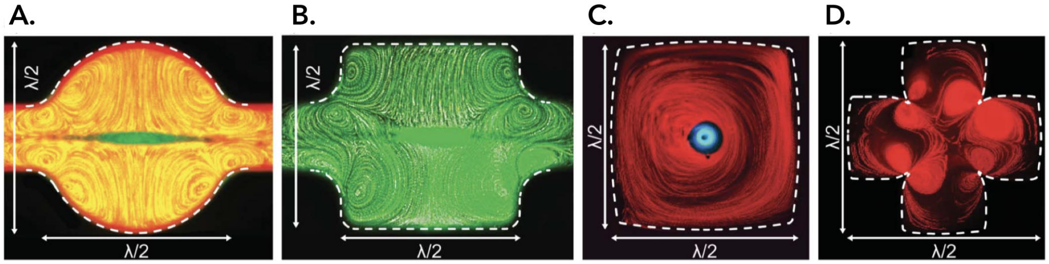

Fig. 2.5 Acoustic streaming patterns in different geometries of the acoustic resonant cavity, visualized by making an overlay of a series of frames from a video clip. The width is between 300 and 350 µm in all cavities, and the driving frequency is between 2.1 and 2.6 MHz. The streaming is tracked by 1 µm fluorescent beads and the trapped cluster in the centre of each cavity contains 5 µm beads in **(A)** and **(B)**, and 10 µm cells in **(C)**. There are only 1 mm beads present in **(D)**. These experiments correspond to Rayleigh streaming [138, 153]

2.2 Acoustic confinement

To confine living or non-living matter in microgravity like conditions, acoustic trapping systems work under the basis of the acoustic radiation forces that arise when a standing wave is set up in a microchannel or in the cavity where a suspension is placed. To create a standing wave inside a cavity or micro-channel, the driving frequency must meet a resonance criterion as follows:

$$w = n\frac{c_0}{2f} = n\frac{\lambda}{2}. \tag{2.29}$$

Where w is the width of the channel or cavity, n is the number of pressure nodes in the standing wave, c_0 is the speed of sound in the fluid, f is the acoustic frequency and λ the wavelength of the acoustic input. The acoustic radiation forces will promote the displacement of objects either to the point of maximum or minimal acoustic potential in the standing wave (Figure 2.6), depending on the acoustic properties of the species being handled.

On a 1D planar standing wave, the acoustic radiation force, as expressed in Equation 2.22, shows that the radiation force can be expressed as the gradient of the acoustic potential U^{rad} where the acoustic potential is given by:

$$U^{rad} = \frac{4\pi}{3}a^3\left[f_1\frac{1}{2}\kappa_0\langle P_{in}^2\rangle - f_2\frac{3}{4}\rho_0\langle v_{in}^2\rangle\right], \tag{2.30}$$

where $\langle P_{in}^2\rangle$ and $\langle v_{in}^2\rangle$ are the time averages of the incoming pressure and velocity fields squared, and the scattering coefficient f_1 and f_2 relate compressibility and density, of the particles and the medium, respectively. These characteristics determine the position of the entities to be handled in the potential. Most cells and micro particles with density and compressibility lower than the surrounding medium will move to the point of minimal acoustic potential, implying that they will displace towards the pressure node of the standing wave.

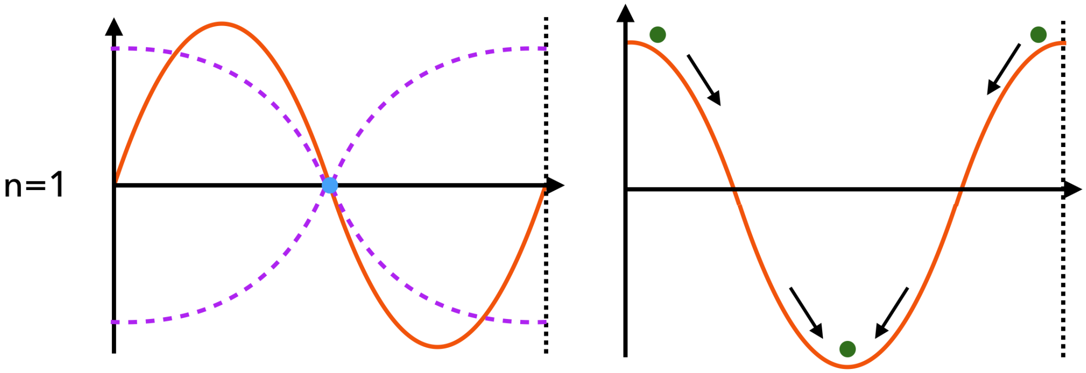

Fig. 2.6 Left: Distribution of the force(solid-line) and pressure (dotted-line) in a standing wave when the distance between the emitter and the reflector is such that a node can be created n=1. Right: the corresponding acoustic potential.

An effective trapping requires a local acoustic potential with high gradient so it can provide trapping even against a background flow. The secondary forces (short distance forces) attract the particles to each other and enhance the formation of stable particle clusters [130].

2.3 Design and fabrication of the acoustic resonator

An important part of this work has been device design. It is a key engineering challenge, due to the fact that in order to make efficient acoustic devices (for ultrasonic cell manipulation), there are several considerations that need to be taken into account. When designing an ultrasonic manipulation device, especially for half-wavelength layered resonators, like the one used throughout this thesis or the ones used by Ohlin et al. [143] or Bazou et al. [98], the first consideration to bear in mind is the size range of the cells to be manipulated. Smaller particles (or cells) require higher operating frequencies to attain the same acoustic radiation forces than the one required by larger particles.

The principal aim of this work is to confine bacteria cells in a levitating environment. Therefore we took into account the dimension of bacteria which are: 3 µm long and 1 µm width. Generally 1-10 MHz ultrasound is suitable for manipulation of 1-20 µm entities, that is the reason why the resonators were designed to work in a 2-5 MHz frequency interval. This implies that the nominal frequency of the transducer needs to be between this range.

Also, it is important to heed whether to work in a single-pressure-node or a multi-node configuration. The desired configuration, no matter which, is given by the distance (w) between the emitter (matching layer) and the reflector (top layer), and it is also related to the frequency at which the resonator is driven, as the wavelength of the emitted wave is given by:

$$\lambda = \frac{c_0}{f}, \tag{2.31}$$

and the distance between emitter and reflector layers relates the number of nodes n with the wavelength as in Equation 2.29

Typically the layered resonator is structured by different layers as seen in Figure 2.7. First, the piezo ceramic transducer that generates the sound is attached to the coupling layer, which is needed to get good acoustic transmission into the system and acts as the bottom of the resonator chamber. Next, the fluid layer containing the cells or beads suspension. This layer either can have inlets and outlets or be completely sealed. At the other end of the system the reflector layer it is placed. This last layer is responsible for reflecting the incoming wave back into the fluid layer. The interference of the incoming and the reflecting wave gives rise to a standing wave [115]. Sometimes a second transducer can be used as the reflection layer [154].

It has been shown in simulations that a good resonator should have a matching layer of a quarter wavelength, a fluid layer of half a wavelength and a reflector layer of a quarter wavelength thickness. This configuration results in a pressure minimum in the centre of the cavity and a pressure maximum at the channel wall [155].

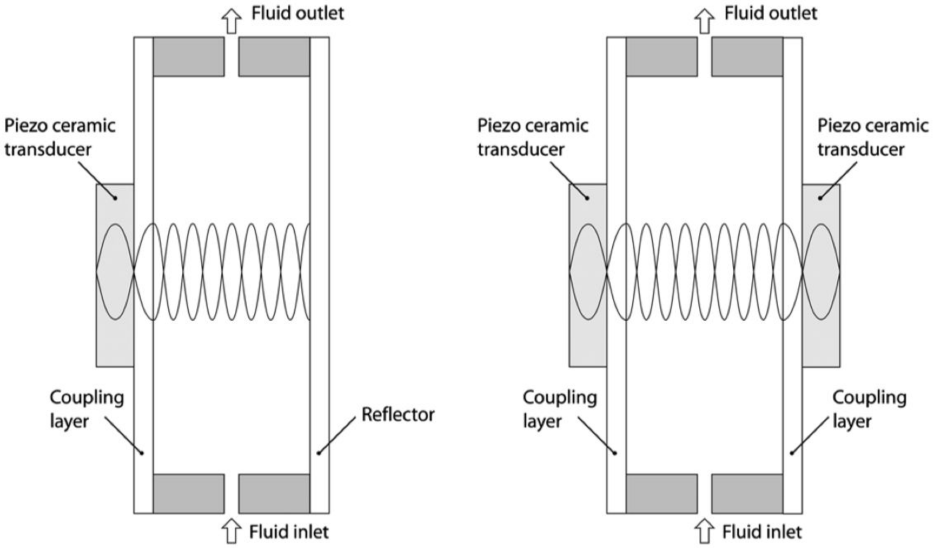

Fig. 2.7 **Components of the acoustic resonator.** Classic configurations of a layered resonator with either a single transducer and a reflector layer or two opposing transducers [115].

To summarize, for our designs we kept in mind the aforementioned characteristics. We selected the single pressure node configuration because this makes imaging less complicated and prevents the interaction between bacteria clusters at different nodal planes. Additionally, since the choice of material plays an important role as well, we used a *well-balanced* combination of materials to achieve a quality system as described by Lenshof et al. [115]

We designed two different resonators, the first one has a fixed distance and frequency; within its cavity a standing wave with a single-pressure node is created. The second one has a removable spacer, by changing the thickness of the spacer the distance between parallel plates can be modified. The thickness of the spacer determines the number of pressure nodes that arise within the cavity of the resonator. The detailed configurations of our layered resonators are presented next (see Figure 2.8):

Fixed distance

The resonator is composed by three main layers: the reflection layer is a 3D-printed lid that wraps half of the resonator and holds in place a circular Quartz-slide 250 µm thick. The emission layer, includes a circular Wrap-around Feedback Piezo-ceramic transducer (Pz-26) from Meggit, with a nominal frequency of 4.6 MHz, that is glued with a water soluble conductive adhesive gel (Tensive) to a 3 cm ^{2} circular silicon (Si) wafer with 250 µm thickness. The wafer is fixed, with Epoxy, to a hollow cylindrical shape made of stainless-steel. The cylinder has 161 µm height (h) and a 1.3 cm radius (r). The Si wafer creates the bottom of the cavity, where the fluid layer is deposited, and the wall is the stainless-steel cylinder. At the bottom, a hat-like stainless-steel structure with a slot acts as a support for the complete resonator. This bottom layer keeps the system level and eases the manipulation on the microscope; the slot provides a place for the wires and cables that connect the transducer.

Adjustable distance

The resonator has five components: the emission plate, where another Wrap-around transducer (Pz-26) this time with a nominal resonance of 3 MHz is glued, as described before, to a circular Si wafer with a 5 cm^2 area and 200 µm thickness. This wafer is firmly fixed into the hollow cilynder structure whose base is a stainless-steel disk. On top of it a Mylar spacer is placed. The thickness of the spacer has to be half the wavelength of sound in water at the resonant frequency, which in our case was 250 µm thick. Over the Mylar spacer, a stainless steel ring is placed, the ring creates a cavity between the emission and the reflection layer that comes on top. The reflection layer is a 500 µm thick Quartz-slide permanently attached to an acrylic lid. As on the previous design, at the bottom a hat-like structure is placed.

It is important to remember that the resonators where fabricated from scratch. The stainless-steel structures were performed at the machine-shop from the laboratory and the assembly of the pieces was done by hand. For these reasons, the dimension that were planned for each design sometimes were not completely accurate. In table 2.1 the theoretical dimensions versus the experimentally obtained (gray columns) ones are summarised:

Table 2.1 Dimensions of the resonators.

Type of device	Driving frequency		Emitter-reflector distance	
Fixed distance	3 MHz	2.7 MHz	250 µm	300 µm
Changeable distance	4 MHz	4.4 MHz	185 µm	170 µm
Fixed distance	2 MHz	2.5 MHz	370 µm	330 µm
Fixed distance	4 MHz	4.1 MHz	180 µm	180 µm

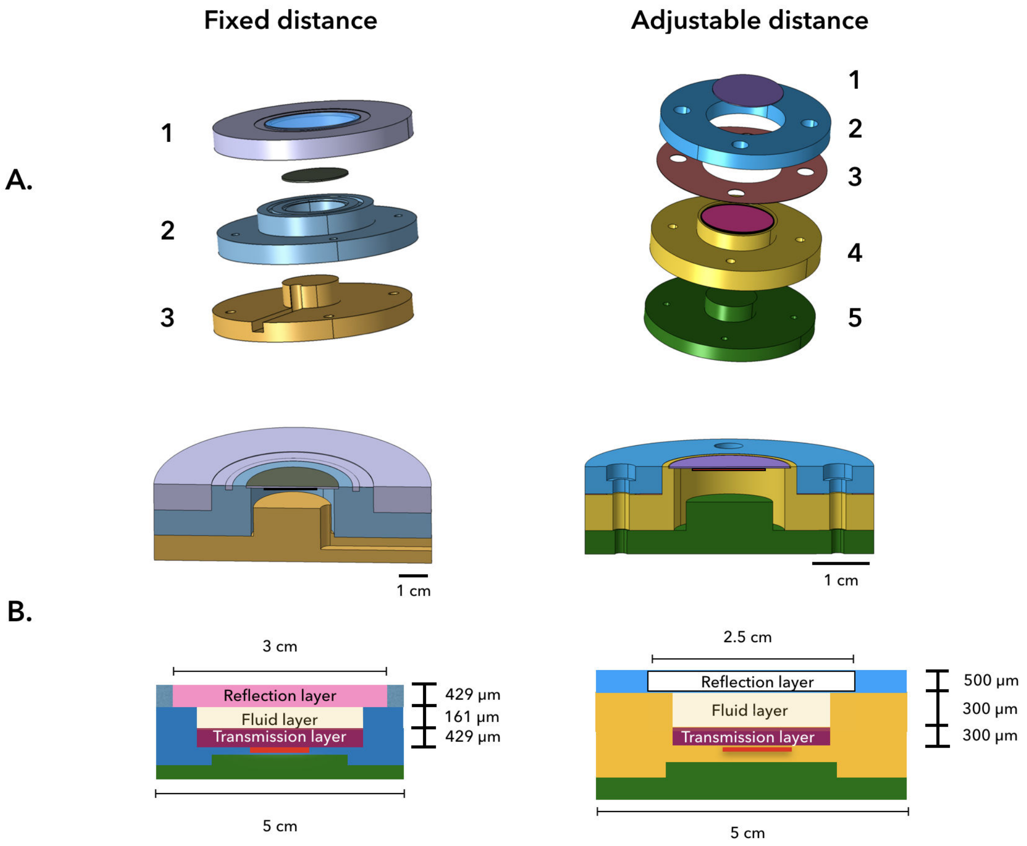

Fig. 2.8 **Components of the acoustic resonator. A.** 3D drawings of the two types of layered resonators designed for this work: a fixed distance one and another with modifiable transmission-reflector layer distance (*w*). The fixed distance configuration comprises three main layers. 1. The reflector layer, that corresponds to a 3-D printed lid that has a permanently fixed Quartz-slide. The Quartz-slide permits optical access for microscopic visualization. 2. Next, the transmission layer that comprises the Si wafer holding the transducer, the wafer is fixed to a hollow cylinder with h=161 µm and r=1.3 cm. 3. At the bottom a hat-like stainless steel supporting structure that holds the system and makes the manipulation on the microscope easier. On the right, the second configuration shows the adjustable distance resonator. The resonator is formed by five layers: 1. The reflection layer is a quartz-slide permanently attached to an acrylic lid. 2. A stainless steel ring is placed on top of the Mylar spacer (3.) that is placed on top of the steel framework holding the emission plate. 4. The emission plate comprises a transducer with a 3MHz nominal resonance glued to a circular Si wafer with a 5 cm^2 area and 200 µm thickness. The wafer is firmly fixed into a stainless-steel structure. 5. Finally, at the bottom, the same hat-like structure as on the other design. Note that in both resonators there is a cavity (or pool) where the suspension is poured. **B.** Schematic diagram showing the real thickness of the three main layers for the resonators that we made. Not always they match the theoretical ones, nevertheless, because stainless steel and quartz have high-quality values the systems works and can trap beads in levitation.

2.4 Characterization of the acoustic trap

The first part of this section was performed in concert with Ludovic Bellebon as part of his master thesis [156] developed during the summer of 2017. The main goal was to measure the acoustic energy density of our acoustic resonator. The approach that was used is based on the z-position temporal tracking of latex and silica micro-beads in the cavity of the resonator. To get to know the acoustic energy density (equation 2.25) it is necessary to know the velocity of the particle during its z-displacement from the bottom of the resonator's cavity towards the pressure node of the standing wave. For that reason, a well known optical phenomenon known as Airy patterns was used. Airy disks are a bright region in the centre of the diffraction pattern resulting from a uniformly-illuminated circular aperture, which together with the series of concentric bright rings around it, is called Airy pattern [157].

When we observe an object in the microscope and it is completely sharp it implies that it is localized on the observation plane. Whereas, when it is not, the object appears out of focus, blurry and some out-of-focus-halos surrounding it appear (Airy patterns). From these observations, we can get that the further an object is from the observation plane the blurriest it gets and the diameter of the surrounding halos increases.

This optical aberration phenomenon was used to characterized the acoustic trap that has a transducer working at a nominal frequency of 3 MHz (λ=500 µm). Since, as stated before, the resonator has a configuration that gives a single-pressure node standing wave. In theory, the distance that should exist between the plates of the resonator is w=(λ/2)=250 µm. Nevertheless, due to fabrication constraints the distance between plates is 300 µm. The best driving frequency, found experimentally, is 2.7 MHz, that matches with a 277 µme inter-plates distance. Even with these slight changes in the configuration, we can be sure that the pressure node is near the cavity centre as we measure the focal plane experimentally using optical microscopy.

Remembering equations 2.24- 2.26 we can see that the acoustic contrast factor Φ characterizes the compressibility and density of the particles. Their values determine the position of the particles in the potential well (Figure 2.6); if, for example, $\Phi > 0$ particles will migrate toward the nodes whereas if it is $\Phi < 0$ they will migrate to the anti-nodes. The properties playing a central role in the characterization of the resonator are the density ρ of the particles and the fluid, and their compressibility κ.

Considering that a particle in a suspension subjected to an acoustic field is affected by the buoyancy force, the Stokes force F_S and the acoustic radiation force F^{rad}. Following the description made by Dron et al. [158] the buoyancy force can be neglected, therefore:

$$F^{rad} = F_S. \tag{2.32}$$

$$\frac{\pi}{A} E_{ac} k_p^3 \Phi \sin(2kz) e_z = 3\pi d_p U_F e_z. \tag{2.33}$$

Re-arranging the terms the focusing speed of a particle within the cavity is:

$$u_F(z) = \frac{E_{ac} d_p^2 \Phi k}{12\mu} sin(2kz). \tag{2.34}$$

The focusing speed was determined experimentally by following the changes in the diameter of the Airy disks for several particles. The diameter of the ring was followed from the bottom of the cavity (out of focus ring) towards the nodal plane (sharp particle) as in Figure 2.9.

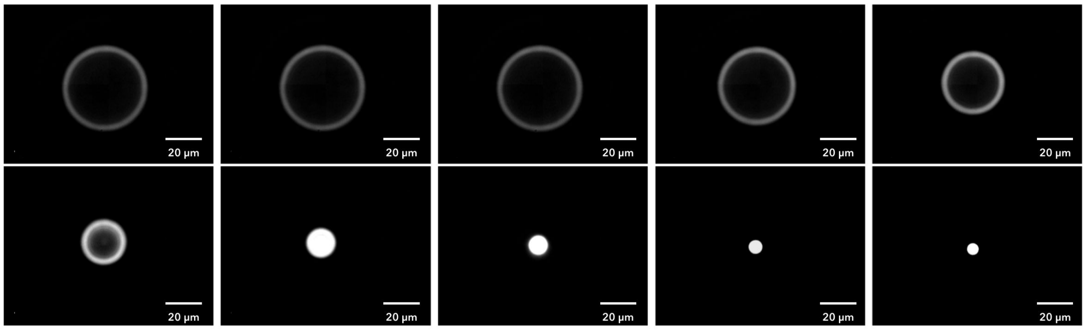

Fig. 2.9 Airy disk evolution during the migration of a latex bead towards the levitation-plane (nodal plane). Just one latex bead was selected for the z-migration, each image was taken 1 second apart, the Voltage applied during this experiment was 10 U_{pp}.

Later using the following equation [158] the focusing speed was deduced: :

$$D_e(z) = \sqrt{M^2 d_p^2 + 5.95(M+1)^2 \lambda_{fluo}^2 f^2 + \frac{M^2 z^2 {D_a^2}^2}{s+z}} \tag{2.35}$$

Which relates the effective diameter of the particle $D_e = d_e M$, which is the relation between the diameter of the halo emitted by the particle d_e and the magnification used in the microscope M. The distance between the objective and the observation plane s, the focal number of the objective f its focal distance F and the relation that exist between them to obtain the aperture of the lens D_a. Finally, the excitation wavelength (λ) of the tracked fluorescent particles.

It was observed that the focusing speed depends on the voltage that is applied to the transducer, at higher voltages the higher focusing speed [156]. As expected, the acoustic energy density in the resonator also varies linearly with respect to the applied voltage see Figure 2.10 as it has been proved experimentally by Bruss et al [94].

Later, the acoustic energy density E_{ac} was obtained, see Figure 2.10. Note that the obtained energy is just for a particular point of the system, and does not describe the complete energy distribution in the resonator's cavity.

The difference in E_{ac} between latex (blue dots) and silica beads (red dots) shown in Figure 2.10 can be explained because the energy distribution on the surface of the resonator is not homogeneous. It is known that the pressure field distribution on the surface of the transducer fluctuates [94]. Later, the acoustic radiation force was calculated and found to be in the order of pico-Newtons, as the energy density the force also increases with the applied voltage [156].

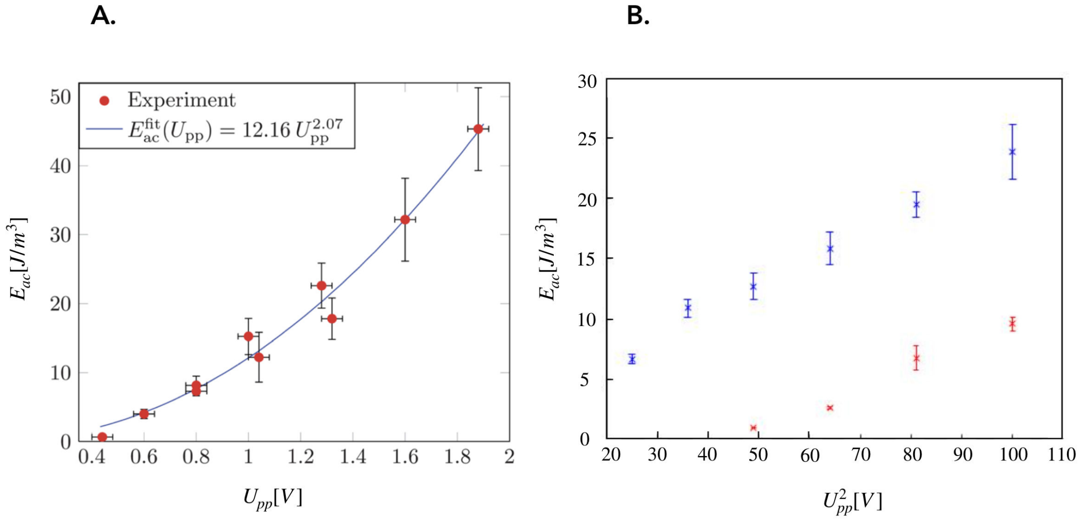

Fig. 2.10 **Acoustic energy density versus applied square peak-to-peak voltage. A.** Measured acoustic energy density E_{ac} versus U_{pp} on the piezo transducer (each point) for a $\frac{1}{4}\lambda$ resonator. Measured on the micro-resonator used by the Barnkob et al [117]. The full line is a power law fit to the experimental data. **B.** E_{ac} vs U_{pp}^2 measured on our self-made resonator with adjustable inter-plane distance. The blue dots represent the measurement obtained with latex particles and the red ones with silica beads. Each point is the average of five measurements. The points without error bars correspond to single measurements [156].

Also, we evaluated the macro distribution of aggregates in the cavity of the resonator. To perform the study we used bacteria, both motile cells and non-motile cells. We poured 500 µm in the cavity and found experimentally the best driving frequency for each resonator that was evaluated.

Once the driving frequency was found, small floating aggregates of bacteria start to form in specific regions of the cavity. For each resonator we repeated the experiment at least three times. We found that when using an acoustic resonator with a 4.1 MHz driving frequency (at 20 U_{pp}), inoculated with motile *Escherichia coli*, the average number of aggregates was 4±1. Whilst the number of aggregates was not always the same, the region where they gather was fixed as in Figure 2.11. For non-motile bacteria we found that the region where the aggregates formed remained the same but the number of aggregates increased three times.

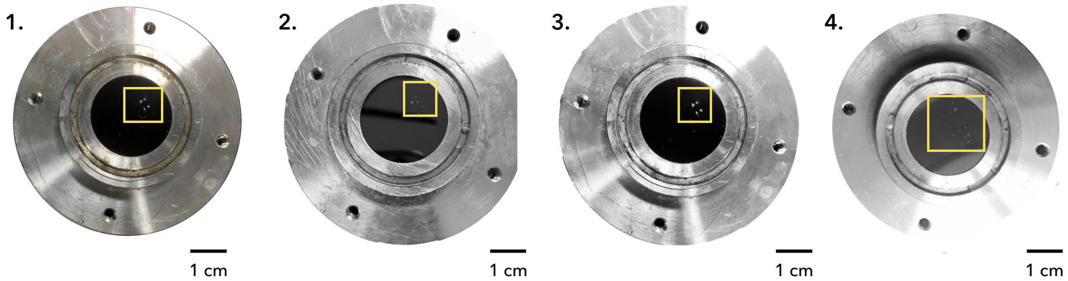

Fig. 2.11 **Macro distribution of bacteria aggregates.** The acoustic resonator working at 4.1 MHz driving frequency inoculated with motile *Escherichia coli* (1-3) and inoculated with non-motile cell exhibited the formation of small aggregates in the same region (yellow squared). The number of aggregates that arise in each experiment was found to be phenotype-dependent.

2.5 Discussion

The interaction between acoustic waves and suspensions is a well documented phenomenon. As previously described, its theory establishes that the acoustic radiation forces, both the primary and the secondary, arising due to this interaction permit the contact-less control of the entities within the suspension, either cells or particles.

Normally the manipulation of these entities takes place inside the cavity of an acoustic resonator (e.g. layered or half-wavelength resonator). Inside the cavity a standing wave is created due to the interference of the emitted and reflected waves. In there, the primary radiation force enhances the displacement of particles or cells towards the pressure nodes of anti-nodes. The position where they gather is dependent of the acoustic properties of the particles. Later, the secondary force stabilises the clusters that are formed at this position.

In this work we have designed two types of layered resonators, one with a fixed emitter-reflector distance and a second one with adjustable distance. In both cases the distance was such that, according to the nominal frequency of the transducer on the emitter layer, a standing wave with a single pressure node arises. Whilst for the first type the number of pressure nodes cannot be changed, for the second one is tunable by modifying the thickness of the Mylar-spacer that determines the distance of the layers. The latter can easily be used to explore interactions between aggregates at different nodal planes, situation that we do not evaluate in this work.

The characterisation of the resonators, in particular that of the fixed-distance resonator, provided a corroboration of the linear relation between the acoustic energy density and the applied voltage. Also, the magnitude of the primary radiation force was found to be in the order of pico-Newtons. Even when this characterisation does not provides the total energy distribution within the cavity it gave us an idea of the forces and the energy at a specific point of the trap. On the same manner, the macro evaluation showed that the trapping of *Escherichia coli* is possible. Also, due to the geometry and configuration of our acoustic resonator, a single-point confinement is not possible, rather several aggregates are formed in different hot-spots at the nodal plane. This is in accordance with previous works that report the non-homogeneity of acoustic energy in the cavity of the layered resonator [159, 160].

Finally, we found that while the number of aggregates is not always the same the regions where they formed are consistent. This allowed us to determine a region of interest in the cavity surface for further experiments, knowing that aggregates will always arise in the region. Furthermore, the number of aggregates is a phenotype-dependent phenomenon. For example, for non motile cells the number of formed aggregates is bigger than that of the ones formed with motile cells.

It is then evident that acoustic trapping provides a good way to confine bacteria cells, like *E.coli*, away from the surface and can be use to evaluate the formation of floating biofilms. The literature on half-wavelength resonators tells us that the frequencies at which our resonators work do not damage cells providing bio-compatibility

In the following chapter we use the acoustic resonators to evaluate the trapping of bacteria, where we characterised the clustering and disintegration phenomena.

Chapter 3

Escherichia coli under acoustic confinement

Acoustic trapping provides a robust technique to trap and confine almost any entity. As discuss before the properties of the particles or cells to be manipulated that are of particular interest are their density ρ and their compressibility κ [127].

For this reason, and as our aim is to confine bacteria in levitation, we have the opportunity to choose from the vast diversity of bacterial cells. However *E. coli*'s hardiness, versatility, broad palate and ease of handling attracted us. On top of that, it is the most intensively studied and best understood organism on the planet [161]. So from this moment whenever we refer to bacteria we will be referring to *Escherichia coli*.

In this Chapter we discuss the standardised protocols for platting and culturing bacteria; also, the inoculation of the acoustic resonators and their sterilisation protocols. Moreover, the clustering and the first approaches to explain the spreading dynamics of bacterial cluster for both motile and non-motile bacteria. Likewise, we examine the characterisation of the collective motion that arise within the cluster of motile cells.

3.1 Generalities on *Escherichia coli*

Escherichia coli has lurked within our ancestors for millions of years, before they were even human [162]. The story of *Escherichia coli* begins with a German pediatrician, Theodor Escherich, who while isolating bacteria from the diapers of healthy babies noticed a rod-shaped microbe that could produce a "massive, luxurious growth" and called it *Bacterium coli commune* [163]. *Escherichia coli* lives in our gut. Its breed has been studied intensively for a century, it is versatile and quite sophisticated. Through *E. coli* a shared ancient history can be seen. A history that includes the origin of complex features in the common ancestor of all living things, cells. It take us back in time and hint us about the evolutionary pressures that shape important cues for our present existence [162].

The morphogenesis of this microorganism is considerably simple; a cylindrical tube with hemispherical caps 2.5 µm long by about 0.8 µm in diameter [164]—as Howard Berg said: "it resembles a microscopic cocktail sausage" [68].

The Gram-negative bacteria cell division comprises three major steps: the first step involves the replication of DNA, followed by an elongation where the cell becomes twice as long. The last step comprehends a constriction of the elongated cell in the middle and the separation of the two daughter cells. The detailed process is complex and involves several proteins and interactions among them that are not yet fully understood [165–167].

3.2 Motility of *Escherichia coli*

Peritrichously-flagellated bacteria, such as *Escherichia coli*, self-propel in fluids by using specialised motors to rotate multiple helical filaments. The rotation of each motor is transmitted to a short flexible segment called the hook which in turn transmits it to a flagellar filament, enabling swimming of the whole cell [168, 169]. The nanomachine that drives the motion of the flagella is called Bacterial Flagellar Motor (BFM), whose basal body spans the cellular envelope and is comprised of several trans-membrane rings [74]. The rotation of the motor takes place via an interaction between one or more membrane-embedded torque-generating stator units and spore-like proteins along the periphery of the rotor rings. The interaction is powered by the ion-motive force arising from the transit of protons [168, 170].

This bacterial nanomotor is extraordinarily efficient, it can convert the free energy stored in the transmembranal electrochemical gradient into mechanical work. Typically it rotates at approximately 30 Hz, and it can propel the bacteria at speeds up to 100 µm/s, that is 100 body lengths per second [168, 171–173].

The dynamics of a bacterium, considered in the area of active matter as a run-and-tumble particle (RTP), consists of periods of persisting swimming motion called runs, punctuated by sudden changes of direction known as tumbles [174]. During a run, all the flagella are rotating counter-clockwise wrapping into a bundle that pushes the cell along at speeds of 20-35 µm/s [168, 175]. Due to the chirality of the flagella their clockwise motion an their counter-clockwise do not produce the same displacement. If one or more of the motors reverse, the corresponding flagella will leave the bundle and undergo a polymorphic transformation in which the handedness of the helix changes modifying the swimming direction of the cell, that is, the bacteria experiences a tumble [168].

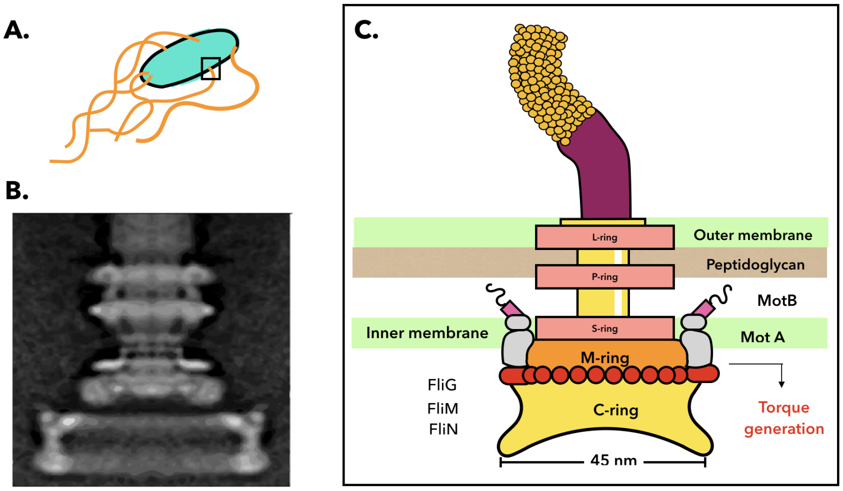

Fig. 3.1 **Bacterial Flagellar Motor A.** *Escherichia coli*, as any other member of the *Enterobacteriaceae* family, is motile via peritrichous flagella, this implies the presence of multiple randomly distributed flagella over the entire bacteria cell. *E. coli* self-propulsion depends on the direction of rotation of its flagella. During a run all the filaments rotate in the same counter-clockwise direction and in a tumble not only the direction of the rotation changes but also the handedness and pitch. The rotary nano-machine driving the self-propulsion–swimming–is known as bacterial flagellar motor. In the micrography (**B**) a part of the motor that is attached to the hook is shown. The image depicts what would be seen in this part of the motor as it rotates [176]. **C.** Structures outside the cell wall include the filament, which can be up to 10 µm long and circa 20 nm of diameter; the hook, a flexible coupling or universal joint. The elements embedded in the cell wall comprise the basal body and include several rings and a rod. The outer pair of rings (L-ring and P-ring) serve as a bushing that gets the rod through the outer membrane. The rod is a drive shaft. In the inner part the rings M-ring and S-ring as just a M-S ring since they are product of the same gene FliF Additionally, the C-ring comprises part of a motor switch complex (FliG, FliM, FliN) that controls the direction of flagellar rotations and has an impact in the torque generation [177, 178].

Thus, the displacement of *E.coli* consists of periods of assumed straight line swimming interrupted by brief burst of rotational motion (see figure 3.2). A typical run lasts about 1 s; to a reasonable approximation the duration of runs is Poisson-distributed, so that tumbles can be viewed as random events occurring with a fixed rate α each of which decorrelates the swimming direction. On the other hand, tumbles are normally shorter, of duration $\tau \simeq 0.1s$, and often treated as instantaneous $(\tau \to 0)$ [179].

At time and length scales much larger than α^{-1} and $l\ \frac{v}{\alpha}$ this motion is a diffusive random walk. The diffusivity in d dimensions is given as [179]:

$$D = \frac{v^2}{\alpha d} \tag{3.1}$$

This diffusivity is hundreds of times larger than what would arise by the Brownian motion of colloidal particles of the same size-as can be experimentally checked using deflagellated mutants [179].

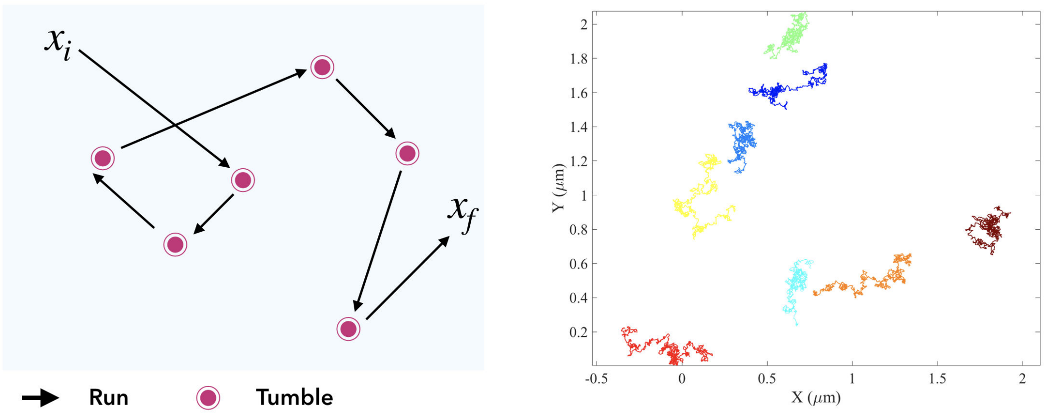

Fig. 3.2 **Schematics of run-and-tumble behaviour.** General description of run-and-tumble behaviour and reconstructions of the swimming trajectories for *Escherichia coli* MG1655-Jovanovic-GFP.motile+.

3.2.1 Density-dependent motility

On systems in which run-and-tumble parameters (v,α) vary in response to the local density of bacteria a true many-body problem arises [179]. To address this case it is necessary to derive an equation for the collective density field [179], following Cates derivation:

$$\rho(r) = \sum_i g(r - r_i), \tag{3.2}$$

where the sum over N particles and g is in principle a delta function in which a finite range of g is introduced. At this point it should be chosen whereas to define a probability density in the N-body configuration space and derive a Fokker-Planck equation or work with the Langevin equations for N particles. The typical approach is to set the Langevin equations with spatially varying run-and-tumble parameters and then allow this variation to occur through a functional dependence on the density field [179]. Where, after the functional of density for the diffusivity $D([\rho],x)$ and the drift velocity $V([\rho],x)$ enter a many-body functional Langevin equation reads in 1D:

$$\dot{\rho} = \left(-\rho V + D\rho\prime + (2D\rho)^{\frac{1}{2}}\Lambda\right)\prime, \tag{3.3}$$

with Λ as a unit for white noise. The last term goes by fixing $\rho = NP$. Through their numerical simulations Cates et al. [89] established that the interacting run-and-tumble system can be mapped at large scales onto a set of interacting Brownian particles. Also, that when $v(\rho)$ and $\alpha(\rho)$ are the same for right and left-moving particles depend on density in a purely local way that the system is equivalent to a fluid whose free energy density $K_B T$ is:

$$f(\rho) = \rho\left(\ln\rho - 1\right) + \int_0^\rho \ln v(u)du \tag{3.4}$$

This implies that when $v(\rho)$ is a sufficiently rapidly decreasing function of ρ the local free energy density $f(\rho)$ has negative curvature in an intermediate range of densities. At which the system is predicted to show a spinodal instability, separating into domains of two coexisting binodal densities ρ_1 and ρ_2 corresponding to a common tangent construction f as shown in Figure 3.3

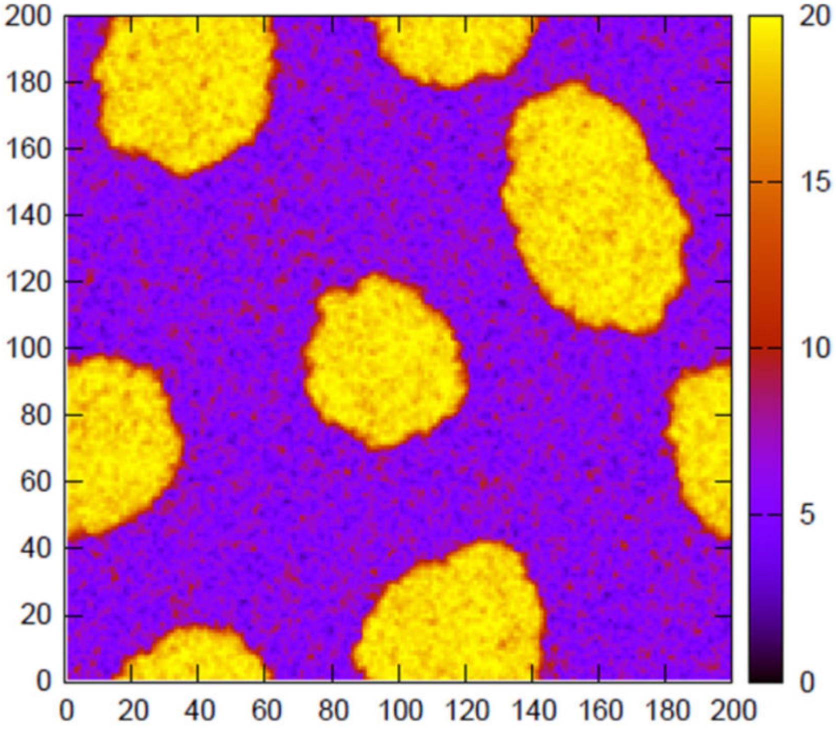

Fig. 3.3 **A 2D run-and-tumble system undergoing motility-induced phase separation.** Simulated via a lattice model (200 × 200 sites) as detailed in [179, 180], with local density (particles per site) colour-coded on the scale to the right

In these numerical simulations [89, 179, 181], domains also form by a different mechanism, such as nucleation and growth, in the density range that lies between the binodal and the spinodal. In this range the system is stable to local perturbations but unstable globally [179]. The physics behind such motility-driven phase separation established that run-and-tumble particles accumulate (i.e. increase in ρ) wherever they slow down reducing their v [89, 179, 181]. But if the velocity is a decreasing function of density, this implies that bacteria also slow down on encountering a region of higher than average density creating a positive feedback loop.

When this numerical approach is compared to normal microbiological phenomena, it matches the aggregation bacteria encounter when they form dense clusters from a uniform initial population. In microbiology this down-regulation of bacteria motility is related to the formation, from planktonic swimmers in dilute suspension to complex communities such as aggregates and biofilms [182].

3.3 *Escherichia coli* under confinement

The presence of boundaries can influence the dynamics of swimming microorganisms, the existence of nearby cells has the same effect. Confinement highly impacts cell locomotion because the concentration of chemical species that affect the motility of the micron sized organisms changes as for the hydrodynamic stresses acting on the cells. In general the four distinct types of wall-influence on the swimming kinematics, in some microorganisms,are [60]:

i. Decrease of swimming speed near the wall

Since viscous drag increases as a body comes closer to a boundary, it might be expected that a cell would slow down. However, since the propulsion method is also drag-based this is not always the case [60].

ii. Changes in their swimming trajectories

In an infinite fluid, *E. coli*, on average, swims in a straight line. On the contrary, near a wall, the helical flagella rotate, creating a net force on the cell at a right angle with respect to the motion and parallel to the surface. There is an exact and opposite force acting on the cell body, which rotates in the opposite direction as the flagella and the net effect is a wall-induced torque. Since a swimming bacterium is in fact torque-free, the cell cannot swim straight but instead rotates at a rate such that the viscous torque from that rotation exactly balances the wall-induced torque, and therefore swims along circles on the surface [60].

iii. Attraction and re-orientation

A single cell swimming near a solid wall sets up a bipolar flow field [183], which does not satisfy the non-slip boundary condition on the wall and images of the cell arise. Due to these images, the cell is subject to the gradients of the image flow field and rotates in the direction parallel to the surface and perpendicular to the cell body [60]. In a confined environment, these cells are therefore always swimming toward a surface, a result which also leads to their accumulation [60].

iv. Potential reduction of cell-cell hydrodynamic interactions

Swimming cells typically behave as force dipoles in an infinite fluid, but when near a solid surface, configurations exist where the total flow field (dipole + images) end up decaying as $1/r^3$ or $1/r^4$, and the hydrodynamic interactions with other cells are weaker as a result [60].

3.4 Acoustic confinement of *Escherichia coli*

As discussed before, the effects produced on bacterial cells by confinement or boundaries are well known and greatly discuss in the literature. Nevertheless, not all the clustering of bacteria arrives due to the presence of boundaries. For example, motility-induce phase separation also known as aggregation in microbiology [89]. Moreover, biological locomotion near boundaries includes surface-associated bacterial communities [184, 185] and thus biofilm formation [32, 186]. Our principal aim is to study the feasibility of producing free floating biofilms; to do so, the first step was studying the clustering process of bacteria in levitation and its phase transition towards complex communities such as aggregates or biofilms.

3.4.1 Model microorganisms

Escherichia coli has proven to be a great model to study motility and biofilm development. For this reason, was selected as the model microorganism for the experiments throughout this work. Several considerations were made to select the *Escherichia coli* strains suitable for our experiments. First, motility is considered an important parameter in the analysis of phenomena arising under confinement of microorganisms; second, a highly motile strain was selected (Jovanovic-GFP.motile+) and thirdly, a motility mutant (Jovanovic-GFP.non-motile) of such strain was constructed.

Motile strains

Escherichia coli*-RP437-*pzA3R-YFP

Considered as a wild-type strain for motility and chemiotaxis assays. It is a *E.coli-K12*derivative with an average swimming speed of 20±3 when supplemented with a motility buffer.µm/s [187].

***Escherichia coli* MG1655-Jovanovic.Motility+**

This bacteria strain is considered as a wild-type, it is also a derivative of *E.coli-K12* with a MG1655 genetic background. The strain is highly motile due to an insertion in the genome that disrupts the gene *yeaJ* (dgcT encoding a diguanylate cyclase); the deletion of *yeaJ* determines the reduction in cyclic diguanosine monophosphate (c-di-GMP) production that results in increased swimming motility. The cells have an average swimming speed of 30±3 µm/s [188].

***Escherichia coli* MG1655-Jovanovic_IATT:Amp*GFPmut3*.Motility+**

This strain is the fluorescent version of the latter via a chromosomal integration of the green fluorescent protein (GFP). The integration vector, allows the introduction of the *gfp* gene into the chromosomes of the bacteria. The average speed is the same as its non-fluorescent counterpart.

Non-motile strains

***Escherichia coli* MG1655-Jovanovic-IAAT:Amp-GFPmut3∆ fliE-R::Cm**

Non-flagellated version of the Jovanovic-GFP motility+ via a deletion of the gene fliE-R, that codifies the flagellar hook-basal body complex protein FliE, inhibiting the production of flagella.

Note: The wild-type Jovanovic strain and the fluorescent and deflagellated strains were kindly donated and constructed, respectively, by our collaborator Dr. Aimee Wessel at the Génétique des biofilms group at Institute Pasteur).

We re-named the strains to ease their reference throughout the manuscript:

***E.coli*-RP437**: *E.coli*-RP437-*pzA3R-YFP*

Jovanovic-motile+: *E.coli* MG1655-Jovanovic.Motility+

Jovanovic-GFP.motile+: *E.coli* MG1655-Jovanovic_IATT:Amp*GFPmut3*.Motility+

Jovanovic-GFP.non-motile:*E. coli*MG1655-Jovanovic-IAAT:Amp-GFPmut3∆fliE-R::Cm

3.4.2 Bacteria cultures

Short-term stock of bacteria strains

Escherichia coli Jovanovic-motile+,Jovanovic-GFP.motile+ and *Escherichia coli* Jovanovic-GFP.non-motile cells were streaked in Lysogeny broth (LB) agar plates. For the non-fluorescent motile strain the agar plates did not contained antibiotics, whereas for the fluorescent strains, both motile and non-motile, the plates were supplemented with 100 $\mu g/ml^{-1}$ of Ampicillin (AMP).

note Ampicillin was added because the bacteria are resistant to it.Also, it is a way to obtain information regarding contamination of the plate, since in a plate with antibiotics only Jovanovic cells can arise–or a resistant phenotype. The agar plates were incubated overnight at 30 °C and later placed inside the fridge at 4°C. The agar plates were made in duplicate for each strain and they served as ready-to-use weekly stocks.

Planktonic cultures

To avoid having bacteria cells in the so called adhesive-sedentary lifestyle we started from over-night cultures and prepared fresh cultures each day.This takes approximately three hours of incubation.

1. *Escherichia coli*-RP437-pzA3R-YFP

E.coli-RP437 cells (from -80°C stock) were cultured in M9 minimal media(Sigma Aldrich) supplemented with casamino acids (Sigma Aldrich). The sample was incubated overnight at 30°C and aerated with orbital shaking (250 rpm) until mid-exponential phase.The next day, the overnight suspension was centrifuged for 5 minutes and a pellet (sedimented bacteria cells) was obtained. Next, the supernatant was discarded and the pellet re-suspended in a motility buffer [189] supplemented with DL-Serine that inhibits cellular division [190]. Subsequently, a dilution of the sample is made and a working suspension with $\mathrm{O.D}_{600} = 0.1$ is obtained.

2. *Escherichia coli* Jovanovic MG1655

For each strain plated on the agar surfaces, a single isolated colony was used to inoculate 5 ml of LB medium. The suspension was incubated overnight at 30°C on a rotary shaker at

250 rpm. The typical optical density (O.D) reached by the suspensions after the overnight growth is higher than 1.5 which corresponds to the stationary phase in the growth curve of these microorganisms [191]. From the overnight suspension, a fresh culture was re-started with an $OD_{600} = 0.05$, it was incubated under the same conditions as before until it reached mid-exponential phase (O.D=0.5). The latter liquid culture was diluted five times. The diluted suspension is *the working one* and it is the one used to inoculate the cavity in all the experiments. According to the McFarland standard the number of colony forming units (CFU) at the working optical density is around $1.5\ X10^8$ [192]

3.5 Experimental set-up

The set-up used for all the experiments performed throughout this thesis is composed by three major sections and the acoustic trapping system (see figure 3.4).

Acoustic trapping system

As previously described (see Chapter 2), the major components of the acoustic resonator are an emission plate, where a piezo-ceramic transducer is glued to a circular Si wafer; a cavity where the bacteria suspension is poured (fluid layer) and on top, a quartz reflector plate that is permanently attached to a plastic lid. The specifics of the components are described in Figure 2.8

Acoustic input control

This part of the set-up supplies the sinusoidal voltage to the piezo-ceramic transducer. Composed by a function generator (LXI Keithley 3390 50 MHz) connected to an amplifier (E Tabor Electronics Dual/Differential wide-band 9250) to increase 10 times (10X) the amplitude of the signal. The output signal is sent to the acoustic resonator and also, to a LeCroy Oscilloscope (WaveAce 214). The oscilloscope allows the observation of the supplied wave form and eases the experimental localisation of the resonance frequency of the transducer.

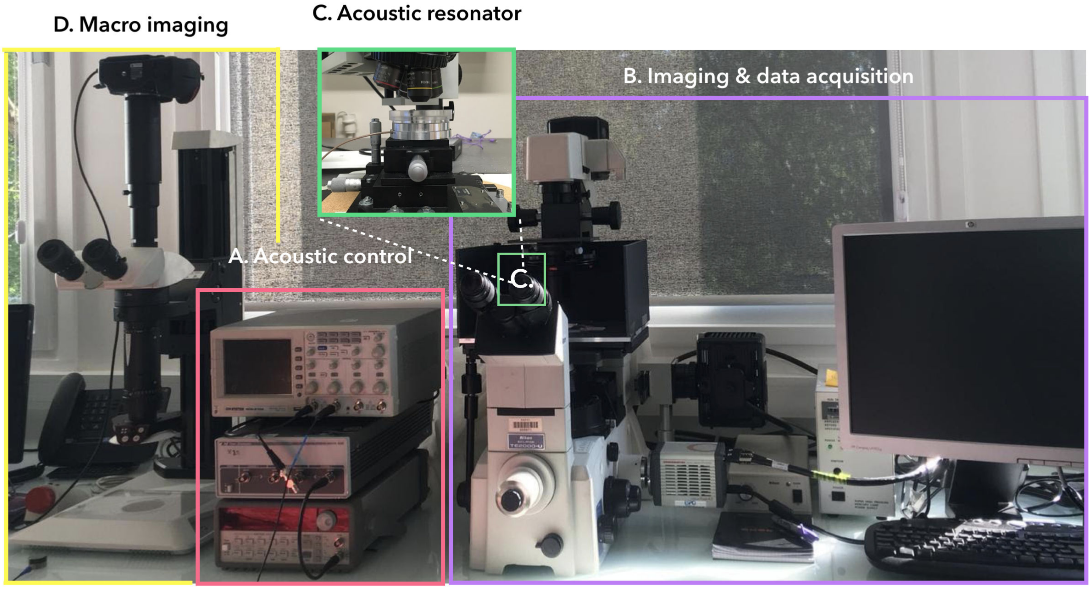

Fig. 3.4 **Experimental set-up.** Colour-coded the four blocks of the set-up.**A.** The acoustic input control (pink) composed by a wave form generator, working in the continuous mode, a signal amplifier (10X) and a oscilloscope. **B.** As the imaging system (violet), a reflection optical microscope coupled with a Hamamatsu camera. The camera is controlled on the computer with the Image HC software. **C.** On top of the microscope stage the acoustic trapping resonator (green) is placed. **D.** The macro imaging block composed by a digital camera connected to a stereo-microscope (yellow).

Imaging and data acquisition

The visualisation of the clustering process was done with an Olympus reflected microscope to which an Hamamatsu Orca flash 4.0 camera is coupled; also, a XYZ-stage (Thorlabs) is used to place the acoustic resonator and control the imaging zones. The control of the microscope and the stage was done manually and the camera was controlled with the HCI Software.

Macro imaging

A stereo-microscope (Leica) coupled with a D850 Nikon digital camera was used to acquire the macro view of the cluster on the resonator during and before the trapping process.

3.6 Material and Methods

3.6.1 Inoculation of the cavity

Two acoustic resonators with the same dimension and previously sterilised—via ultraviolet germicidal irradiation for 20 minutes—were inoculated with 500 μl of the working suspension and sealed with the reflector lid. The control resonator is placed on the bench and left there until the experiments are done; immediately the other resonator, used to perform experiments, is place on the microscope stage.

3.6.2 Clustering and spreading

The clustering process entails a competition between the pressure induced by the acoustic radiation force, described in Chapter 2, which confines cells into a quasi-2D levitation zone at the nodal plane, and the swim pressure of bacteria [193].

To evaluate this dynamics the inoculated acoustic resonator was placed on the microscope stage. The well-known self-propulsion of the motile bacteria or the Brownian motion of the non-motile cells were recorded in a 30 seconds video–with a frame rate of 50 Hz and an exposure time of 20 ms–which serves as a control of the bacteria activity. The control video is useful, as it has been reported that some *E. coli* strains can experience a change in phenotype due to the over-expression of antigen 43, which is an outer-membrane protein that mediates auto-aggregation in liquid culture [194]. That is the case of all Jovanovic strains. A similar case takes place on the RP437 strain, where non-motile variants arise in room temperature stab cultures [195].

Immediately afterwards—to avoid attachment of the cells to the cavity surface—the acoustic resonator was connected to the acoustic input control block. The standing wave is created inside the cavity and the acoustic forces arise (see Chapter 2), prompting the displacement of bacteria towards the node of the wave (i.e. levitation of bacteria) and once at the pressure node the secondary forces enhance the consolidation of the levitated cluster (see Figure 3.5).

The recording of the evolution of the clustering process presented several difficulties. Firstly, the energy distribution in the trap is not uniform, therefore, it is likely that several bacteria clusters form in zones where the local energy density is high, as in Figure 2.11.

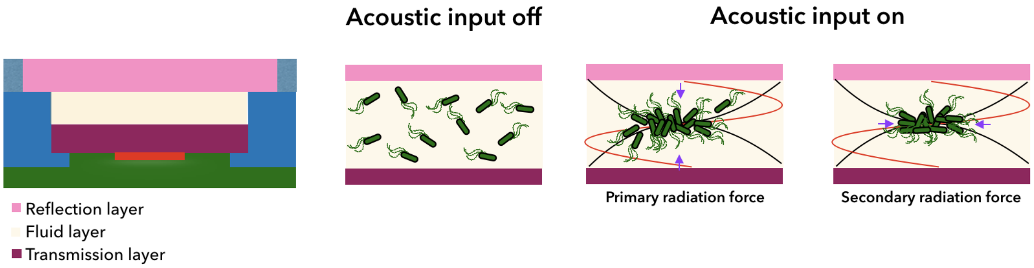

Fig. 3.5 **Schematics of the clustering process.** At the left a representation of a fixed distance resonator prior to inoculation, followed by a representation of the clustering process inside the cavity of the same. When no acoustic input is present (acoustic input off) the bacteria cells are distributed in the entire cavity. Immediately after the acoustic input is send the acoustic waves interact with the bacteria suspension and the F^{rad} arises, prompting the displacement of bacteria towards the nodal plane followed by the consolidation of a cluster in levitation via the secondary forces.

Moreover, the system is sensitive to the slightest modification in the parallel plates and this will have an impact in the acoustic energy distribution and hence, in the position and numbers of clusters [193].

The zones that we picked to record from the quasi-homogeneous distribution of the cells in the cavity to the clustering at the pressure nodal plane were selected based on the macro characterisation of the resonator. As the specific areas, in the resonator, where the clusters formed remained the same for all the strains—when using the same resonator and frequency and voltage conditions. The cluster can change position but within a delimited zone, therefore these were chosen as the regions of interest for all experiments unless is stated the contrary.

Later, in order to characterise the clustering dynamics we use an approach similar to the one used to study the processes of aggregation and disintegration of clusters of non-Brownian paramagnetic beads [196]. The radial distribution function describes how density varies as a function of distance from a reference particle–in our case the density is considered as the number of bacteria-pixels that are just bright pixels–as follows:

$$g(r) = \frac{[M(r+\Delta) - M(r)]}{[\pi(r+\Delta^2) - r^2]}, \tag{3.5}$$

where M is the dimensionless mass (intensity of the pixels) normalised by the total area of the ring with radius r and thickness Δ.The temporal evolution of $g(r)$ was obtained from the acquired videos. For the acquisition the recording settings were Binning 1, image size as 1024×1024, 16 bits depth at 50 Hz.

Afterwards, using a custom-made Matlab code, the grey scale images were improved using a median filter that replaced each pixel with the median value in its 3×3 neighbourhood–the filter reduced the background noise. Later, we performed a background correction where the first frame of the video, corresponding to the nodal plane where no bacteria are in focus, was considered as the background and it was subtracted from the rest of the frames. For each video frame, the intensity of the pixels contained in a annular mask, positioned at the centre, was measured and then divided by total area of the ring. The ring-shaped mask grows radially with a step Δ, corresponding to the average length of a bacteria, covering the entire video frame.

3.6.3 Analysis of the collective motion within a levitating cluster

When bacteria displacement is constricted by walls, either physical as in the case of PDMS microchambers or Hela cells, or virtual, like magnetic, optical or acoustic traps, and the cell density is high bacterial suspensions collective [63, 78, 76] or turbulent behaviours arise [26]. In our case, when the cells are as a consolidated cluster, at the nodal pressure plane they exhibit such a turbulent state. In order to characterise the global dynamics within the cluster we use particle image velocimetry (PIV), a well known non-intrusive method normally used for the bacterial flow visualisation.

Particle image velocimetry (PIV) is an experimental flow measurement technique. The measurements are carried out through the addition of tracer particles (fluorescent beads) to gain insight into the surrounding fluid flow. The tracking of the particles is accomplished by illuminating them, using a laser light source, and capturing their displacements using one or more cameras. The image sequence, capturing the particles displacement over a time, are processed using a correlation algorithm to determine the spatial displacement of the particle. The spatial displacement and the known time interval between images is used to generate positions vector fields representing the particle movement and the corresponding flow. There are different types of PIV measurements classified by the needed equipment and resolution.

We are particular interested in using Micro PIV, as the velocity resolutions are on the scale of micrometers, which is the range of the mean speed of bacteria.

Taking into account the dimensions of our acoustic resonator and the physical phenomena arising in the cavity (acoustic forces and streaming) we realised it is not possible to use particles as tracers, due to the fact they are also responsive to the acoustic field. Instead of providing the visualisation of the flow they tend to accumulate at the centre of the bacterial cluster. Since our aim is to visualise the bacterial flow within the cluster and not the flow generated by ultrasound in the surrounding fluid we decided to use a mixture of fluorescent and non fluorescent bacteria cells. The fluorescent bacteria will act as tracers of the flow generated by them and non-fluorescent ones.

Inoculum preparation

Planktonic liquid cultures were prepared in the same manner described above in subsection 3.4.2, please note the cells used in these experiments are all from the Jovanovic strain. In accordance with the protocol, both working suspensions– of non-fluorescent and fluorescent bacteria–have an OD_{600nm}: 0.1. The final inoculum is a mixture (7:3) of the working suspensions corresponding to Jovanovic motility+ and Jovanovic-GFP motility+. The mixture was swirled and the cavity was inoculated as stated in previous sections. Note that the final concentration of the *mixed-inoculum* is again OD_{600nm}: 0.1

Evaluation of the in-plane kinetic energy E_{xy} versus the applied voltage U_{pp}

In Chapter 2 we established there is a linear relationship between the applied peak-to-peak voltage U_{pp} on the transducer and the acoustic energy density E_{ac}. This implies that decreasing or increasing the applied voltage changes the magnitude of the acoustic forces interacting with the particles, hence the confinement strength. This situation is analogous to the study of how the inter-wall distance, on microfluidic channels, modifies the emergence of collective behaviours on bacterial suspensions [75] but in our case we can neglect the hydrodynamics interactions of the bacteria and the walls.

To evaluate the effect of the confinement strength on the emergence of the turbulent flow within a cluster in levitation, the cavity was inoculated using the established protocol. The transducer driving frequency, with and applied voltage set at 20 U_{pp}, was found experimentally and the clustering process took place; then we waited for 20 minutes until the consolidation of a cluster. Afterwards, a 90 minutes video with the same characteristic described before was recorded. Immediately the applied voltage was reduce by a factor of two and a second video was then acquired, this process was repeated until reached weak confinement i.e. 10 U_{pp} . The first 20 seconds correspond to confinement at 20 U_{pp} and the remaining 70 s with a 18 U$_{pp}$ input.We selected as lower limit 10 U_{pp} since is the threshold value prior to spreading of the cells into the bulk.

Quantification of bacterial flows

The images were analysed considering that the acoustic confinement yields quasi-2 dimensional clusters and also that, from the acquired in-plane images, 2D projected velocities of 3D suspension motion can be analysed. A Matlab code, inspired on the PIVLAB Matlab toolbox, made in collaboration with Dr.Alexandre Vilquin was used to determine the bacteria flow velocity (v_x,v_y). In the aforementioned code, a temporal filtering, which permits to avoid non-physical velocity gaps between two frames is applied to all the images. Later, we can manually validate the vectors that were assigned followed by interpolation for the missing data. Several values of a median filter were evaluated and plotted, the one that do not remove importat data but yet smoothed it was chosen and then applied to reduce noise. Later, the velocity of the flow and its rotational is calculated to obtain the velocity and the vorticity fields, see Figure 3.6. Next, the global bacterial flows were quantified by the in-plane kinetic energy E$_{xy}(t)$ and enstrophy $\Omega_z(t)$ defined by [197]:

$$E_{xy}(t) = \langle \frac{v_x^2 + v_y^2}{2} \rangle, \tag{3.6}$$

$$\Omega_z(t) = \langle \frac{\omega_z^2}{2} \rangle, \tag{3.7}$$

where $\omega_z = \partial_x v_y - \partial_y v_x$ y the vertical component of vorticity and $\langle \cdot \rangle$ is spatial average.

To further analyse the collective motion of bacteria in a surface-less environments we calculated the transverse 2-dimensional correlation function and the correlation length.

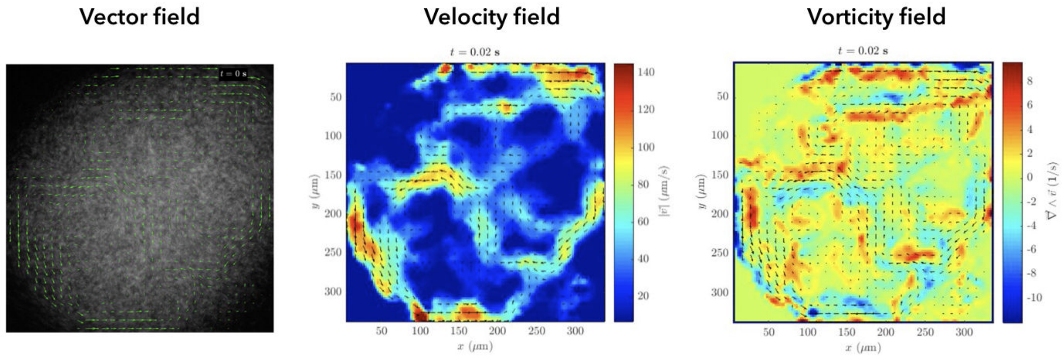

Fig. 3.6 **PIV characterisation of the global flow for a given experiment.** The vector field provides a representation of the flow, where a vector is associated to a point in space providing the position coordinates U_x and Uy; the green arrows indicate the direction and magnitude of the bacterial flow. From the temporal evolution of these coordinates, given by the time between frames, the velocity field was calculated and the distribution of the velocity in the cluster is shown, from fast movement (red) to slow movement (blue). As we can see on the periphery of the cluster the displacement is higher and a pump-like motion is present. Next, then rotational of the velocity vector is calculated to obtained the vorticity field. Form the later we can get a description of the local spinning motion at some point in the flow of bacteria.

3.6.4 First approach on the characterisation of the spreading dynamics

In the case of the spreading dynamics, firstly, we selected a consolidated cluster based on the following aspects: the cluster should be dense, which implies that it was formed in a spot of maximum energy density; and it should fit the working area of the microscope to be able to record the re-distribution of cells. Later, the same acquisition and video treatment protocols used for the clustering process were implemented.

3.7 Results

3.7.1 Clustering

Clustering process using *Escherichia coli*-RP437 strain

The first set of experiments regarding clustering and spreading dynamics were performed using *E.coli*RP437-YFP as model microorganisms and the results are part of the work developed at the Acoustofluidics group; it has already been published at the beginning of 2018 [193].

To study the acoustic trapping of bacteria at the nodal plane the resonators were inoculated with bacteria, always at mid-exponential phase, the volume and optical density were the same for all experiments (see Materials and Methods). After the inoculation, and prior to the acoustic confinement, the bacteria cells were distributed in the entire volume of the cavity, as we can see in the first image of Figure 3.7. At this point, bacteria perform their typical reorientation displacement (run and tumble), constantly modifying the swimming trajectories. Afterwards, when the sample was exposed to the acoustic field, that is, the emission plate was excited with a continuous sinusoidal signal at 2 MHZ and 20 U_{pp}, the field promotes the bacteria displacement towards the nodal plane followed by focusing and confinement of the sample via the scattering of the acoustic waves.

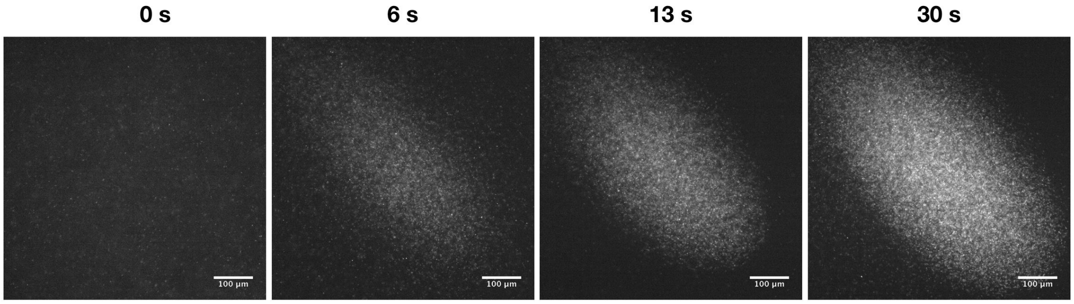

Fig. 3.7 **Clustering of *E. coli*-RP437-YFP in the acoustic trap.** Photographs of the induced clustering in the acoustic levitation trap. The pictures correspond to different times; the first one to the suspension in the cavity and the following photographs correspond to the effects after the acoustic field interacts with the bacterial cells and the clustering takes place. The white dots correspond to the bacteria, we can see than not all off them have the same intensity, this is determined by the position respect to the nodal plane, as the pictures focus at the nodal plane.

As stated before, the bacteria driven by the radiation force—and possibly due to the streaming generated by the waves-fluid interaction—towards the levitation plane which for this experiments was located at 185 μm above the surface of the emission plate ($t = 30s$). During this process, the fluid was dragged and a back flow was immediately established in the cavity, triggering an advective flow that enables the competition between the bacteria activity and the transversal and axial components of the acoustic radiation force as portrayed in [193]. This generated a perturbation in the initial concentration profile similar to the perturbation observed in a system of highly active colloids [96]. Thereafter, bacteria got close to each other prompting cell to cell interactions inside ellipsoidal clusters that take approximately two and a half minutes to consolidate (see Figure 3.8).

Figure 3.8 shows the changes of the normalised bacteria-pixels density (coloured bar) as a function of time. The x-axis represents the position from the centre of the image towards its edge, where 85 concentric rings with a δr thickness. In each one of them the density of bacteria-pixels was calculated following equation 3.7. For example, if we fixed the temporal evolution in the inner ring (radius 6px=2 μm) we can see than the change in bacteria density increases with time as in the first picture there where no bacteria and once the cluster is consolidated bacteria are contained within the region—which corresponds to a clustering process.

After we analysed the experiments performed with this $E.coli - RP437$ strain we found out that there are some biological shortcomings that we did not considerate previously. For example, our microbiological protocol was not robust enough to provide motile cells all the time so a lot of experiments needed to be discharged. Later, we found that the reason is that non-motile variants arise if the cells are not culture on soft agar. The improved protocol, to keep working with this cells, was more tedious and also, there was not a standardisation or enough background information of the cell construct, at least the one that was available in the laboratory. In order to save time and facilitate the handling of microorganisms we decided to change the model strain.

From now on, all the experiments were performed using the Jovanovic strains (*Escherichia coli*) all the results henceforth presented are the ones obtained for this bacteria strains.

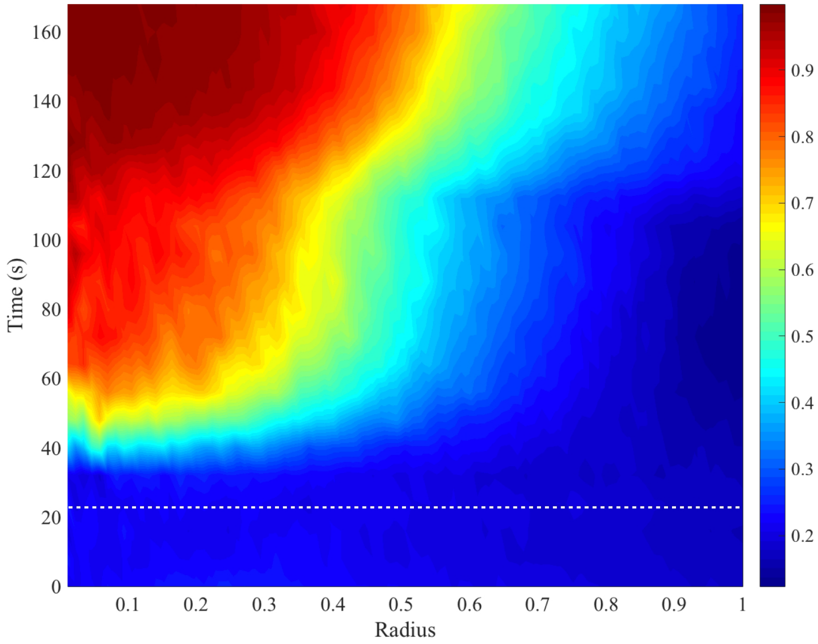

Fig. 3.8 **Spatiotemporal distribution of the area fraction in the clustering process.** The bacterial concentration increases in the centre of the region once the acoustic trapping begins (indicated by the white dotted line). It takes 20 s to form a highly dense aggregate (red) from an initial homogeneous distribution (blue). When the cluster is stable, in other words, when there is no input of bacteria towards the centre, we can distinguish three regions. As we can see in the image: the red region with the highest concentration, the yellow-blue part with an intermediate concentration, and the dark blue with a gas-like phase, where bacteria cells are still free to move in their run and tumble fashion (see movie 1 [193]). The colour bar (from blue to red) depicts the increasing values of bacteria occupying an area fraction.

Clustering process using the Jovanovic strains

In this section we evaluated the impact of motility in the clustering process. For that reason our new model microorganisms are a positive control (motility) and a negative control (non-motile). The strain are: Jovanovic-GFP.motile+ and its de-flagellated variant; Jovanovic-GFP.non-motile. The bacteria cells were cultured following the standardised protocol in 3.4.2, the same for the inoculation of the resonator.

We inoculated with a suspensions of Jovanovic-GFP.motile+ , or Jovanovic-GFP.non-motile depending on the experiment, using the same growth phase and optical density as in the previous experiments (mid-exponential phase and OD 0.5). In this case we inoculated two similar resonators one as a control and one for the experiment. Everything was done under sterile conditions. Once the resonator (for the experiment) was inoculated it was placed on the microscope stage, the best driving frequency at 20 U_{pp} was found experimentally, it varied from 4.1 MHz to 4.6 MHz. Remember that this occurs due to small differences on the parallel plates.The clustering process was recorded and analysed as described in the methods section.

The analysis of the clustering process yielded similar results for the Jovanovic-GFP.motile+ and Jovanovic-GFP.non-motile strains to the ones obtained with *E. coli*-RP437, see Figure 3.9.

However, it is important to remark that the number of cluster obtained when inoculating with the non motile variant were higher that the ones for the motile cells, as depicted in Figure 3.10. So far we have assumed that our bacterial floating clusters are two dimensional. The Confocal micro-graphs showed that on the contrary, our clusters are 3-dimensional structures with a gallete-like shape, see Figure 3.10.

We hypothesis that all these could be due to the fact that motile strains can counteract the effect of the acoustic forces by they own propulsion (swim pressure), whereas the non motile bacteria can be seen as Brownian particles being confined.

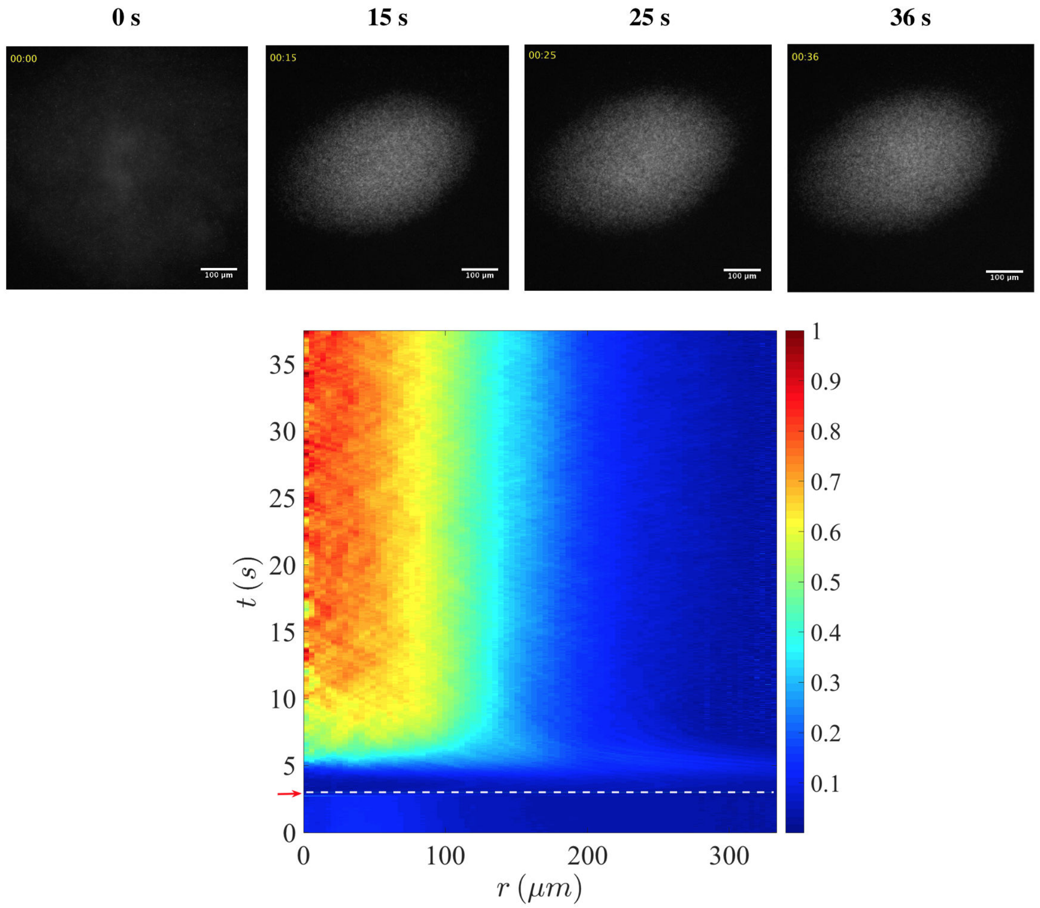

Fig. 3.9 **Spatiotemporal analysis of the clustering process for Jovanovic motile strain** On the top, four representative images of the clustering process. Starting at time zero (0 s) where the inoculation of the resonator just took place and the cells are distributed within the cavity of the resonator. The acoustic input was turn on at 3 s (red arrow and dotted white line), the gathering of bacteria started and at 15 s; we can see a clusters that evolves slowly until it reaches it consolidated state at 36 s. The heat map (on the bottom), shows the temporal evolution of the concentration (colour bar) at different position from the centre con the cluster (x-axis) determined by r in µm. No matter the x-position the clustering started from a quasi homogeneous distribution that gather in the centre of the image, we can then see that the approximate size of the cluster in this example is around 200 µm.

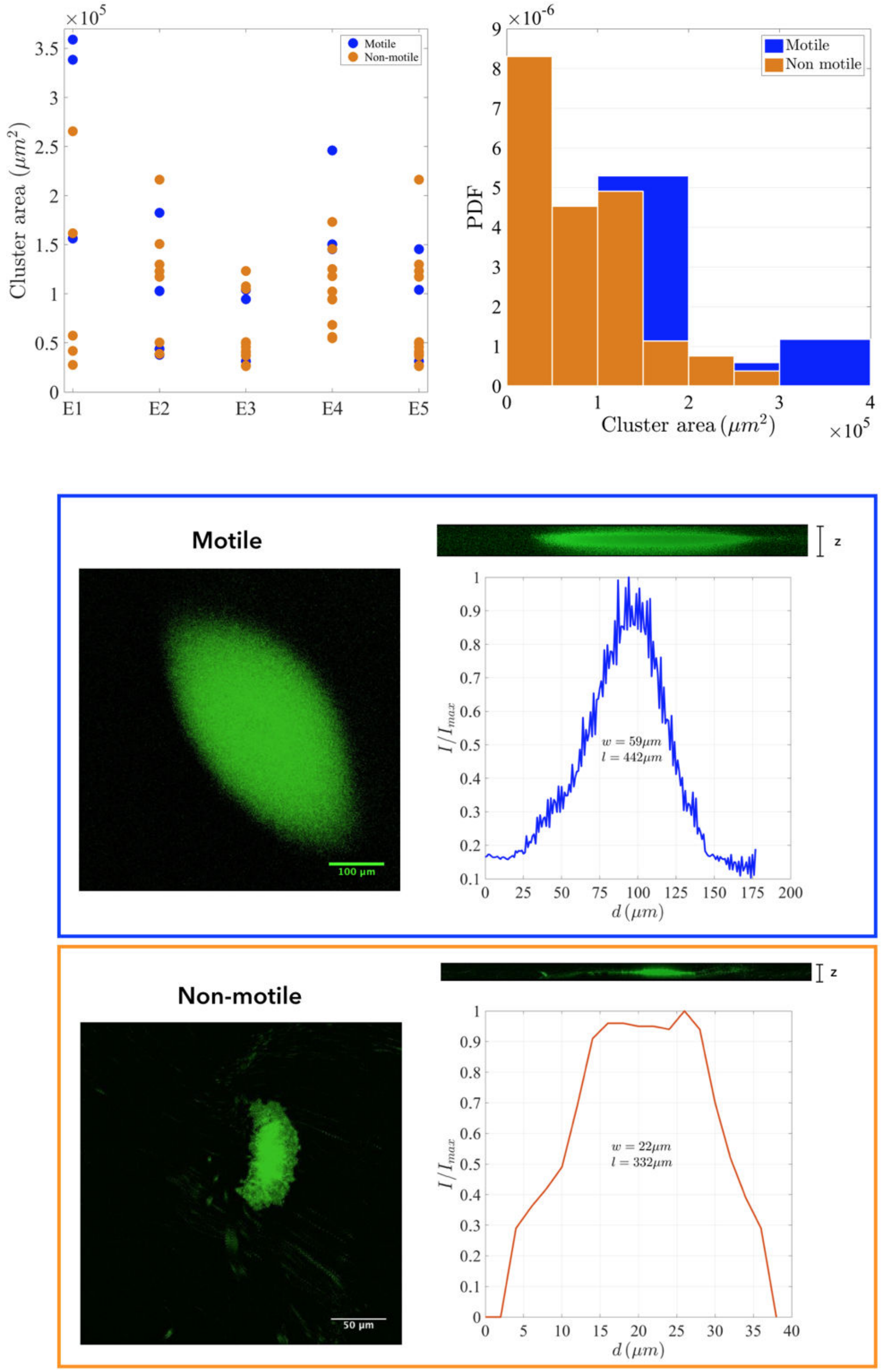

Fig. 3.10 **In-plane area distribution and thickness of motile and non motile clusters.** The apparent size of the clusters do not present considerable variation depending on the phenotype, however the number of cluster obtained is phenotype dependent. The mean values are 9 for non motile and 2 for motile cells. Preliminary, experiments shows that the thickness depends also on the phenotype.

3.7.2 Collective motion within the levitating cluster

Within the clusters where the motile cells are the forming units a swarm-like collective motion aroused. However it was only present when the forming units are active (self-propped). At the beginning, we considered that this phenomenon could be happening because the clusters were positioned in a high energetic spot and as a consequence it was and artefact of the acoustic streaming within our cavity. But since it is only present from motile cells we can conclude that the emergent dynamics is not due to acoustic streaming, but rather, it is mediated by bacteria self-propulsion.

In the bacteria collective motion literature there is vast research on how the confinement affects the emergence of this dynamics. In our system, besides being able to get ride of the hydrodynamic interaction of the cells with the walls, that normally produce drawbacks, the confinement is given by the radiation forces—primary and secondary—and to the applied voltage. We then considered as strong confinement when 20 U_{pp} were applies and weak confinement when the input was 10 U_{pp}.

To analyse the changes in the global bacteria flow properties as a function of the strength of confinement; a cluster confined with the strongest trap, which in our configuration is an input of 20 U_{pp}, was later release in a controlled manner. The magnitude of the acoustic constrains was reduced with a 2 U_{pp} step from 20 U_{pp} to 10 U_{pp}. A minute and a half video was acquired for each magnitude of confinement (each applied voltage). For each experiment (n=5), the video images were processed to enhance their contrast by a 0.3 % (see Figure 3.12).

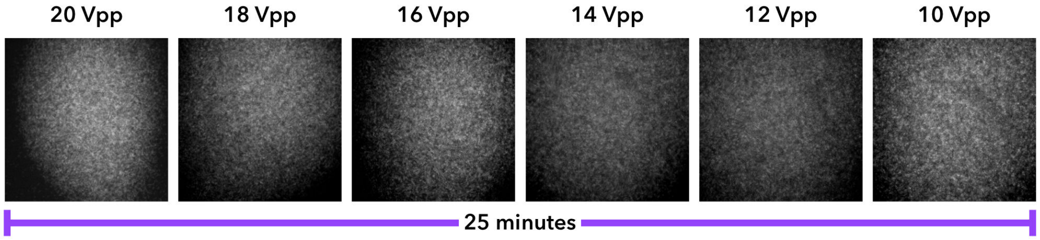

Fig. 3.11 **Change of confinement strength modifies the cluster in-plane area.** Sequence of images from strong confinement (20 U_{pp}), where the cluster was more compact, to weak confinement (10 U_{pp}) where the apparent in-plane are increased. We can see how the bacteria (white pixels) distribution expands occupying a well defined region at when strongly confined to become complete disperse int he image area at weak confinement. The temporal scale for this type of experiments was 25 minutes.

The first thing that we can see is the evolution of the in-plane area as a function of confinement. As it was expected, the cluster area increased as the confinement decreased (see Figure 3.12), as the bacteria where no densely packed and regain their degrees of freedom enabling their displacement in the new width of the acoustic potential.

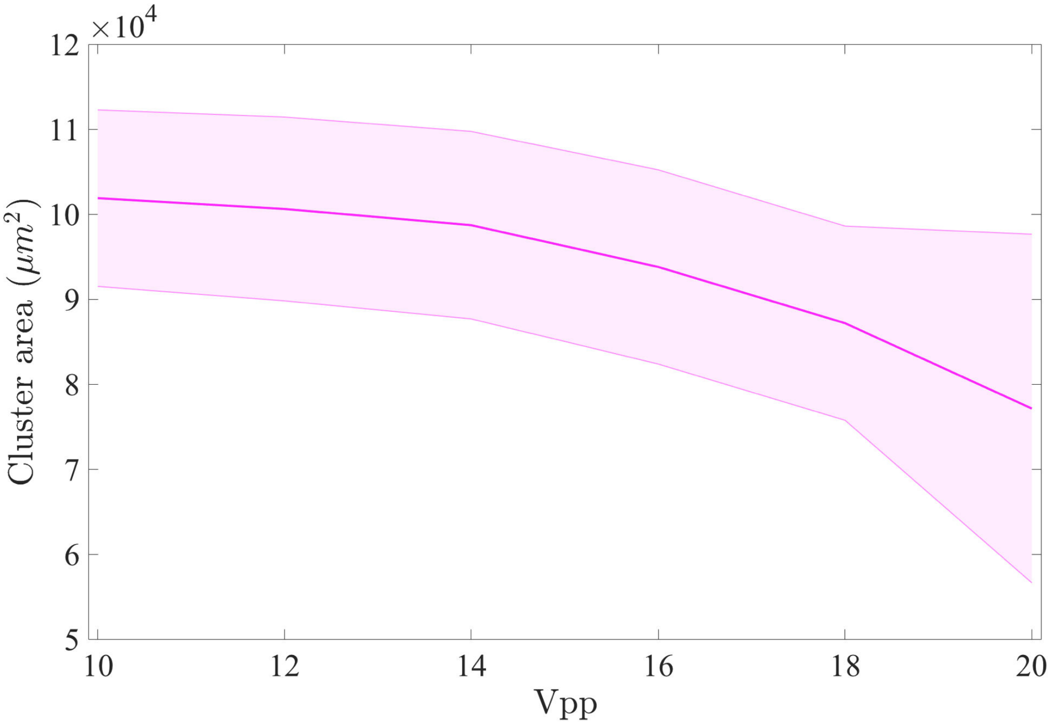

Fig. 3.12 **In-plane area varies with the applied confinement.** The mean in-plane cluster area decreases with confinement. The plot shows the mean values (solid line) for n=5 the shaded area correspond to the standard deviation and the lines correspond to the maximum and minimal values. The same behaviour is observed in all cases.

The acquired videos (see virtual appendix) tell us about the evident changes in the displacement of bacteria when they are subjected to weaker acoustic confinement (i.e. less applied voltage). The characterisation of the global flow using PIV gave us the vector field of the bacteria flow. Considering the vector positions in (x,y) and the time between frames the velocity and vorticity fields were calculated. Later, adopting standard statistical measures from classical turbulence analysis, the global bacterial flow was quantified by the in-plane kinetic energy $\langle E_{xy} \rangle$ using equation 2.6 and the in-plane enstrophy Ω_z equation 2.7.

To have general information of the bacterial flow we defined three regions in each cluster under strong confinement (20 U_{pp}). The regions were determined taking as first consideration the shape of the confined cluster at strong confinement. For each experiment the shape of the cluster was fitted with an ellipse and the values of the centroid and the minor and major axis were obtained.

The regions corresponded to the centroid of the fitted ellipse and the two others at the periphery of the cluster (top and bottom), see Figure 3.13–circular masks delimited the regions.

The centroid has as coordinates the values (x,y) and a radius r such that the area cover by the circular region corresponds to 10% of the total area of the cluster. The (x,y) values for the other regions are such that they are localised at a distance corresponding to half the length of the minor axis of the ellipse. The regions for each experiment are summarised in table 3.1 where in each column the coordinates, as in (x,y,r), of the circular regions are presented.

Table 3.1 Regions analysed within bacterial clusters.

Experiment	Top	Centroid	Bottom
E_1	(200,200,150)	(553,484,150)	(800,870,150)
E_2	(700,250,117)	(458,473,117)	(300,760,117)
E_3	(718,126,160)	(502,447,160)	(814,690,160)
E_4	(170,210,160)	(512,447,160)	(875,650,160)
E_5	(600,220,109)	(493,481,109)	(670,700,109)

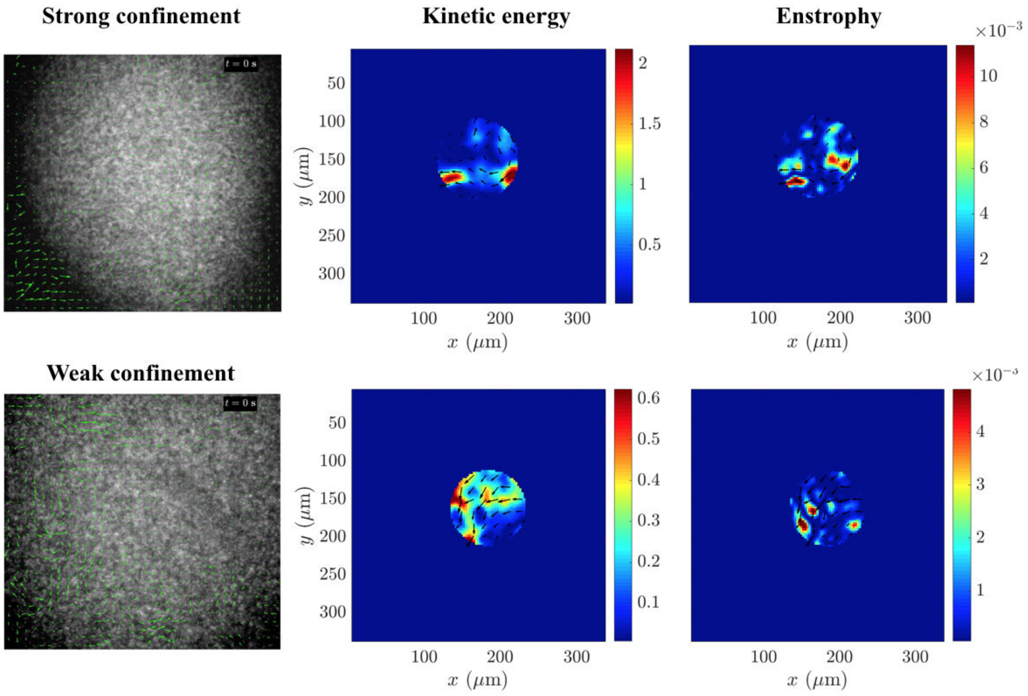

Fig. 3.13 **Regions of analysis for a given experiment, especial focus on the centroid.** Example of computed in-plane kinetic energy and in-plane enstrophy for a given experiments at the centroid region. On the same manner it was computer for the other two region and the distribution in each region was obtained. Note that the values of the mean kinetic energy (colour bar) dropped significantly from strong confinement to weak as for the enstrophy values.

The mean kinetic energy $\langle E_{xy} \rangle$ of each region and each experiments was calculated. The mean of these values was obtained and was plotted versus the applied voltage U_{pp}, the error bars correspond to the standard deviation. We found out that for all our experiments, no matter the initial size of the cluster, $\langle E_{xy} \rangle$ increases as a function of confinement. That is at strong confinement greater kinetic energy. The same is truth for the mean in-plane enstrophy of all the regions and Ω_z, see Figure 3.14.

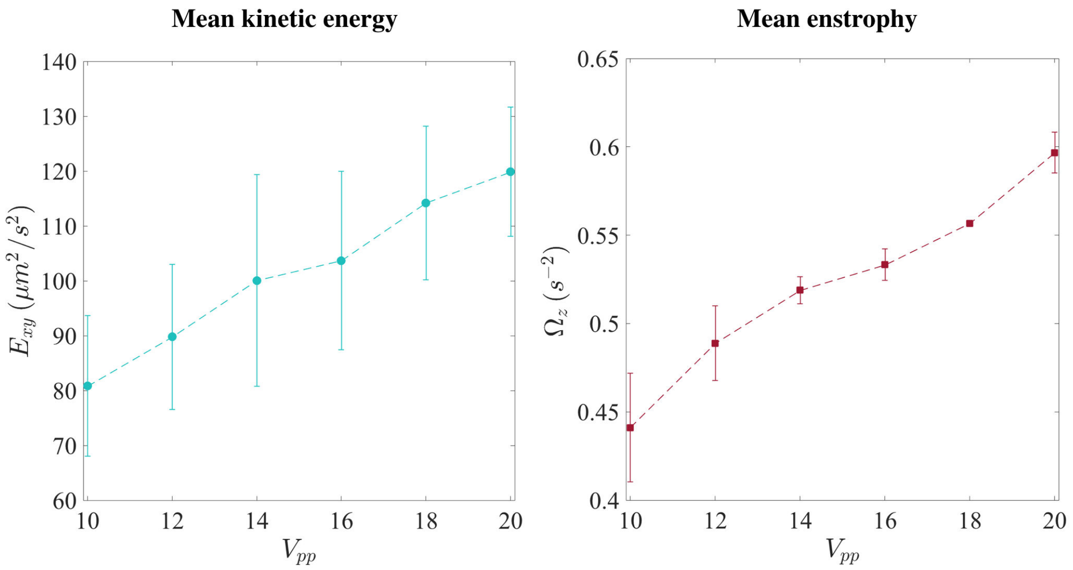

Fig. 3.14 **Mean values of the of $\langle E_{xy} \rangle$ and Ω_z as a function of confinement** The mean kinetic energy and the mean enstrophy (n=5) exhibited the same behaviour; in both cases the values increases as a function of confinement.This invite us to think that the cell-cell interaction, that increases at strong confinement, promotes a rapid displacement of the cells and also a more pronounce swirling. The error bars in both cases correspond to the standard deviation and each point is the mean value of five experiments.

To further characterised the collective dynamics we took a bigger region within the cluster neglecting the edges to make sure that the effects that we were quantifying were due to bacteria and not as due to streaming in the cavity. We calculated the velocity distribution in the region and also observed a decrease of the velocity values as a function of time. Implying that when bacteria are strongly confined they formed patches that can move as swarms an thence displace in the same direction at higher velocities,see Figure 3.15.

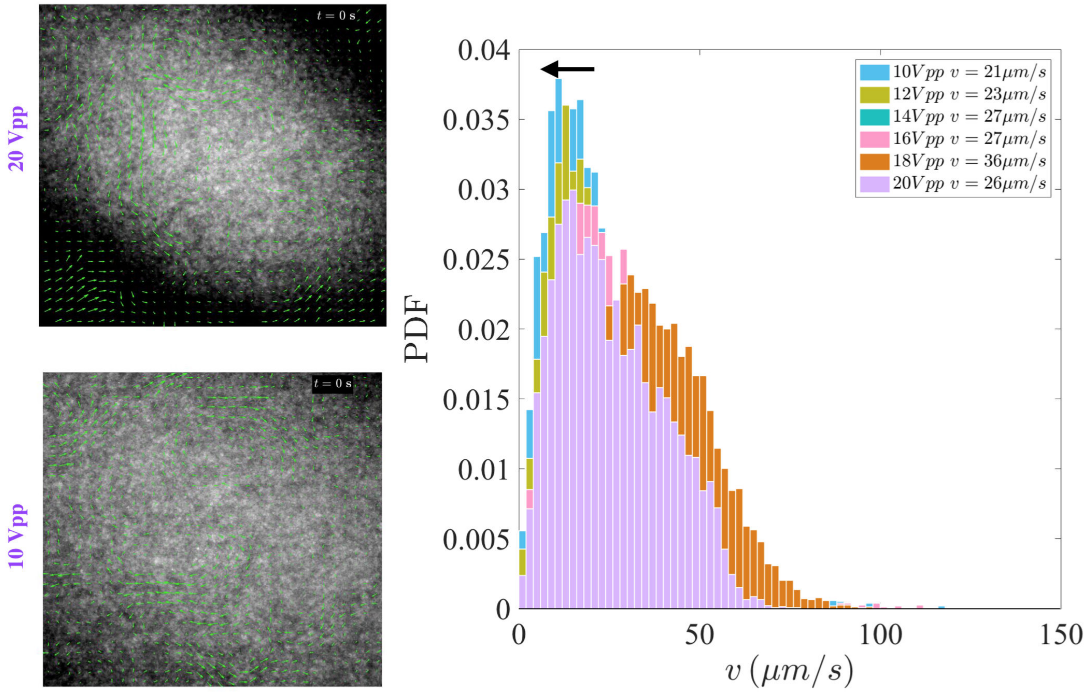

Fig. 3.15 **Velocity distributions, from weak to strong confinement** The analysis of the velocity distribution took place neglecting the edges of the clusters since the high values of velocities could be mediated by the streaming of the surrounding. The selected region occupies three-quarters of the cluster. The velocities distribution shift to the left, to lower values of velocities when the confinement forces are reduces. Corroborating the fact that cell-cell interaction promotes higher velocities.

Afterwards, we calculated the two-dimensional spatial correlation function in each cluster at each magnitude of confinement. We evaluated how the v_x changed in the y directions and how the v_y evolved in the x direction as follows:

$$C_{v_y}(\Delta x) = \frac{\left\langle V_y(x,y)V_y(x+\Delta x,y)\right\rangle}{v_y^2}, \tag{3.8}$$

$$C_{v_x}(\Delta y) = \frac{\left\langle V_x(x,y)V_x(x,y+\Delta y)\right\rangle}{v_y^2}. \tag{3.9}$$

The correlations that we found for each experiment at different confinement strengths helped us to characterised the swarms of bacteria within the flow, see Figure 3.16.

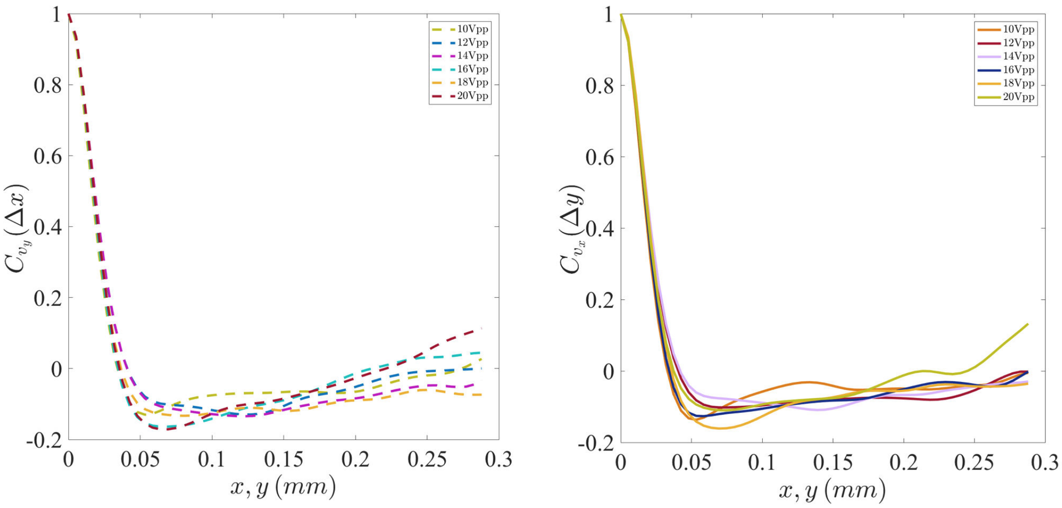

Fig. 3.16 **Two-dimensional spatial correlation** On the left the transverse correlation $C_{v_y}(\Delta x)$ at each confinement magnitude and on the left $C_{v_x}(\Delta y)$.The cut-off value of our examination was at 0.1 for both cases.

Later we measured the the correlation distance in terms of space The integral scale that we found was 20 bacteria bodies width and it also changes with the confinement (Figure **??**).

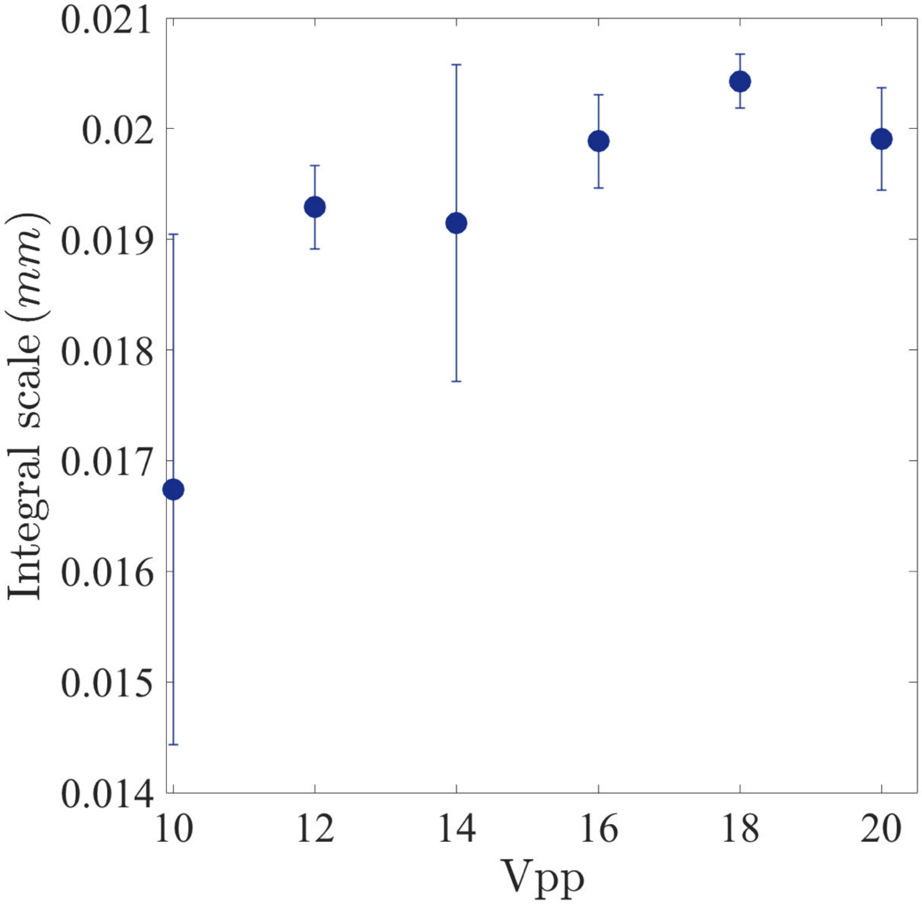

Fig. 3.17 **Mean correlation length** The mean values of the two dimensional spatial correlations put in evidence that the correlation length increases with confinement as it was expected.The number of cell-cell interaction and hence the number of swarm-like patches increases at highly dense cluster and and and diluted clusters is not present.

3.7.3 First approach to characterise the spreading dynamics

As before, the first experiments regarding the spreading dynamics were performed using the RP437 strain as the model organism. The clustering process that lead to consolidated clusters in levitation was previously evaluated. However,as soon as the acoustic forces were removed, the bacteria dispersed back into the bulk. In other words, the withdrawing of the acoustic forces liberated the bacteria and a spreading process occurred. In Supplementary Movie 2 [193], we showed how the highly concentrated cluster expands after an implosion—where patters that could be related to the swarming-like and collective behaviour, discuss in the section above, remained at the nodal plan. Afterwards a relaxation process took place and the cluster diluted, leaving bacteria in and out of focus. This means that the levitating bacteria community diffused either horizontally or out of plane towards the walls of the resonator (z-axis).

The quantification of the spreading dynamics as a function of time is portrayed in Figure 3.18. The entire cluster in divided in 85 thin rings, as described in the methods section. The use of this technique, allowed us to follow the dynamics at different radii of the spreading process, clearly observing a transient marked by the inflow and outflow ring by ring. This behaviour persists for all the cluster we analysed, although the transient reduces when the circularity of the cluster increases. To describe the spreading kinetics of the bacteria contained in each ring (i.e. a given distance from the centroid of the ellipse) we denoted C as the concentration within a ring at an specific time. The initial value C_0 corresponds to the bacteria being acoustically trapped at a time $t_0 = 0$ and a final concentration C_f when bacteria are fully dispersed in the complete area at $t_f = \infty$.

The spreading is assumed to be a first order process, in accordance to the order of reaction determination described by Panikov [], with a rate proportional to $C - C_f$:

$$\frac{dC}{dt} = -k(C - C_f), \tag{3.10}$$

and its solution:

$$C = (C_0 - C_f)e^{-kt} + C_f. \tag{3.11}$$

The solution shows that C reduces exponentially with a characteristic time k that depends on the distance from the centroid of the cluster. Firstly, we noticed that all curves converged at C_f, indicating that bacteria spread homogeneously. Secondly, for the last five rings $C_0 - C_f$ is negative, meaning that the rings have empty segments due to the elliptical shape of the cluster and our analysis technique which might not be the best approach. We can also see that it takes less than 5 seconds for these rings to be replenished by bacteria from the inside creating a in-flow. Thereafter, the decay is exponential.

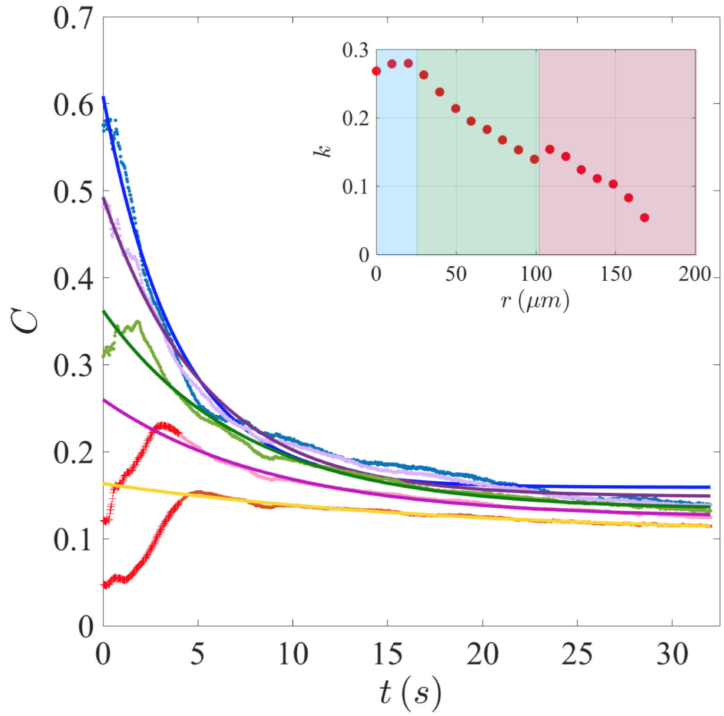

Fig. 3.18 **Bacteria concentration decays as a function of r.** The bacterial cluster is divided in 85 concentric rings of thickness q (for clarity, only 5 are shown in Figure 3.18). In each one of them we estimated the bacteria concentration in terms of the intensity in grey scale normalised by the area of the ring. The temporal evolution of the concentration in each right was then assessed. Top-to-bottom curves correspond to inner-to-outer rings, i.e. from the centroid to the periphery. Note that the decay in the inner rings is faster. Whereas, closer to the edge of the cluster is almost constant. In the inset the decay rate for each ring as a function of the ring radius is plotted. We see three different behaviours with fast (blue), medium (green) and slow decaying rates (red).

The values of k, which are plotted in the inset of Figure 3.18, clearly revealed three decaying behaviours: constant with a fast decaying rate **(blue)**, concavely decreasing with a medium rate **(green)** and convexly decreasing with a slower rate **(red)**. The averaged rate in these regions are 0.3, 0.2, and 0.1 s^{-1}, respectively, we estimated the characteristic spreading speeds, $s = qk$ (the product of the ring thickness and decaying rates) to be 1.2 µm/s, 0.78 µm/s and 0.39 µm/s.

The spreading dynamics is phenotype dependent. This was corroborated when we switch to the Jovanovic strains in our experiments. When we analysed the cluster formed by Jovanovic-GFP.motility+ cells we observed the same implosion followed by a relaxation and a diffusion process as for the RP437. On the contrary, the spreading process for non-motile bacteria did not followed the same dynamics. Once the acoustic input was removed the cell did not dispersed back into the bulk, rather the consolidated cluster sedimented towards the surface of the cavity,see Figure 3.20.

Again we analysed the spreading dynamics following the same approach used for RP437 and we also found the same exponential decay and characteristics k rates plotted in the input of the Figure 3.20. Nevertheless the three characteristic rates were not evident.
The Jovanovic strains also displayed the same implosion and relaxation process after the release from the acoustic confinement. Following the approach used by Takatori et al. [96]to evaluate the"explosion" of active crystals trapped with and acoustic trap. In our analysis, we used the same assumption proposed by Takatori et al. [96] neglecting the fact that our cluster is 3-dimensional and again focusing only the in-plane spreading only after the relaxation of the same took place.

The spreading as a function of the distance to the centre of the cluster was a analysed and it can be described as a diffusion process that can be described by a Gaussian function of the type $e^{\frac{-r^2}{nDt}}$ with r the distance t the centre of the cluster, D the diffusion coefficient and t the time.

It is important to remark that the spreading for motile cells did not took place. The clusters remain entangled even when the acoustic input was removed, they did not diffuse back rather they just sedimented towards the surface of the resonator.Nevertheless, we consider that this approaches to evaluate such complex phenomena come short, and a deeper analysis should be performed. We are sure only this topic is complex enough to be a single thesis topic,

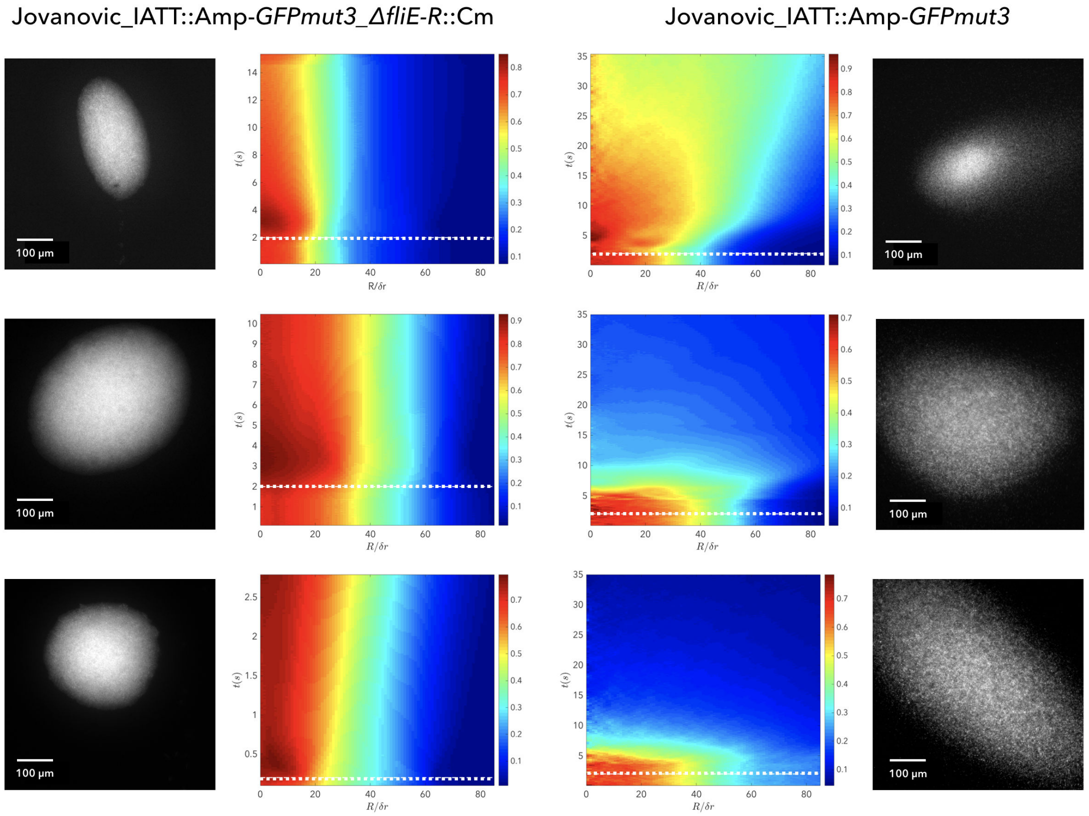

Jovanovic_IATT::Amp-*GFPmut3_ΔfliE-R*::Cm

Jovanovic_IATT::Amp-*GFPmut3*

Fig. 3.19 **Spreading processes of non-motile and motile strains** On the first two columns (left) images and heat-maps of 3 cluster of Jovanovic-GFP.non-motile. As seen here, the cluster do not spread but rather maintains it size, whereas the spreading of cluster formed with Jovanovic-GFP.motile cells disperse after the acoustic input is remove (dotted white line.). This phenomenon is conserved for all the cluster no matter the size.

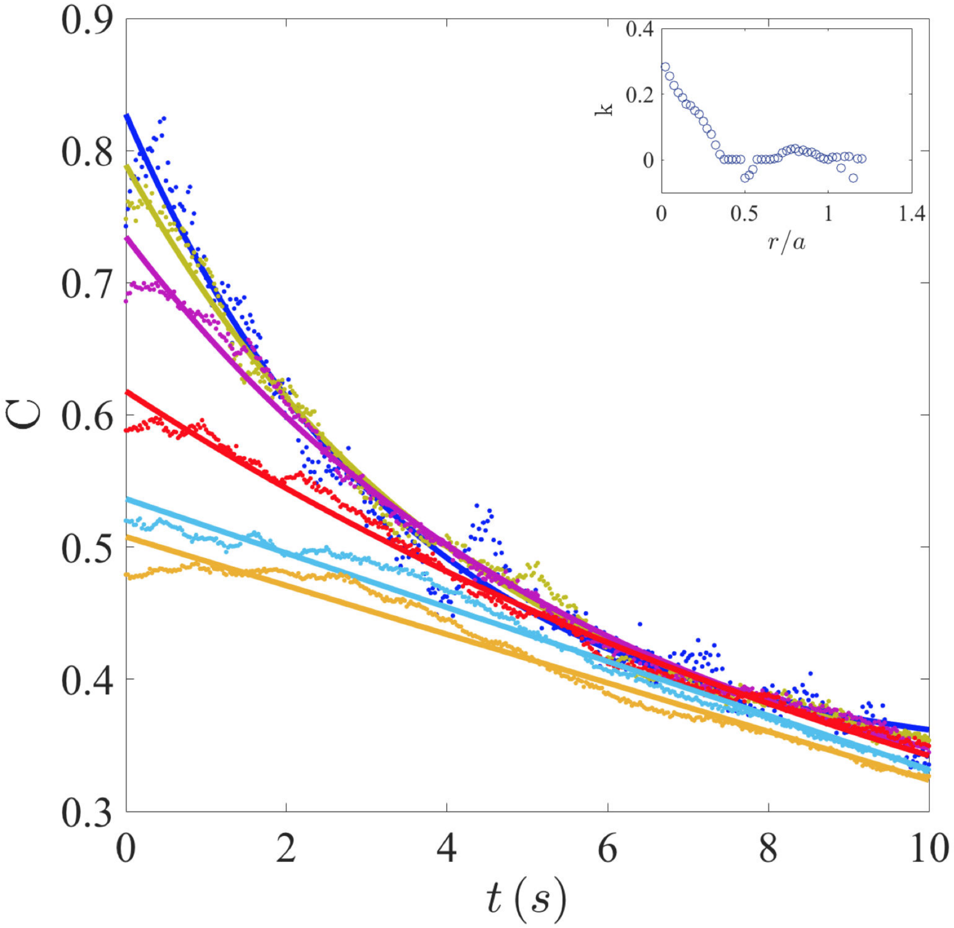

Fig. 3.20 **Bacteria concentration decays as a function of r.** The bacterial cluster is divided in 85 concentric rings of thickness q. In each one of them we estimated the bacteria concentration in terms of the intensity in grey scale normalised by the area of the ring. The temporal evolution of the concentration in each right was then assessed. Top-to-bottom curves correspond to inner-to-outer rings, i.e. from the centroid to the periphery. The decay in the inner rings is faster, whereas, decreases. In the inset the decay rate for each ring as a function of the ring radius is plotted. We see that with this strain the three characteristic spreading rates are not as clear as before.

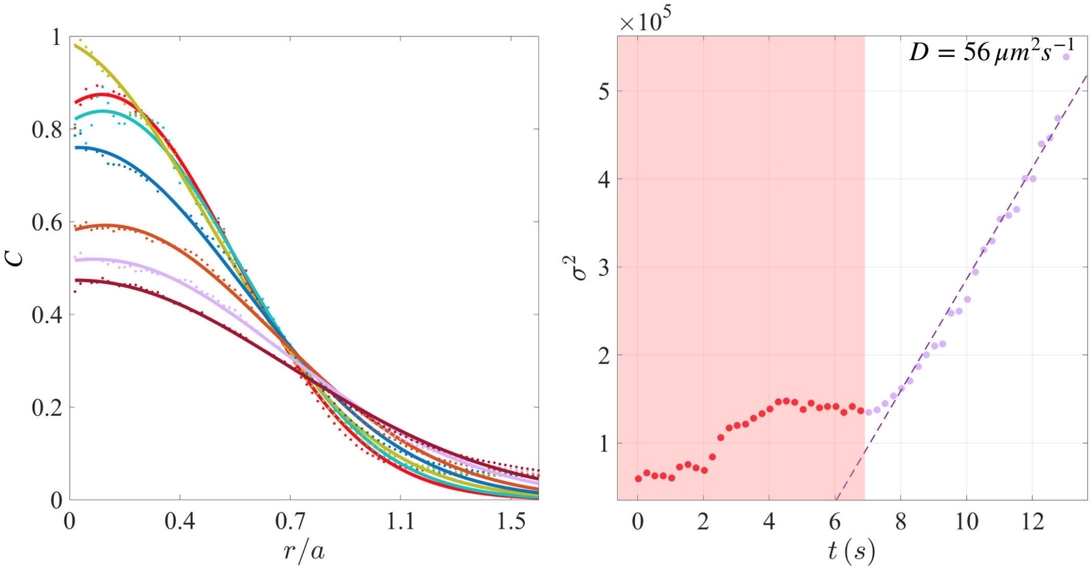

Fig. 3.21 **Spreading process as a function of the distance to the centre of the cluster** The cluster was evaluated after the relaxation process took place. The spreading as a function of the distance to the centre of the cluster can be described by a Gaussian function and a diffusion coefficient can be obtained. The red dash on the graph on the right correspond to the sigma values previous to the relaxation process where it cannot be consider diffusive, after the relaxation process a diffusive process took place and a coefficient value was found.

which is outside of the scope of this work.

3.8 Discussion

The use of acoustic waves to confine bacteria provided acoustic forces with magnitudes in the order of piconewtons (pN) enabling the redistribution of the cells in the cavity of the resonator. The acoustic forces that arise from the interaction of the acoustic field and the cells promoted the sudden increase of bacteria density at energetic hot spots in the nodal plane, triggering the emergence of thin disk-shaped clusters, restricting the degrees of freedom of bacteria.

The displacement towards the nodal plane, or clustering process, is effective for both motile and non-motile bacteria. So we can say that the acoustic confinement is phenotype and genotype independent.

Also, we observed that within the levitating cluster bacterial collective behaviours arose, but only for the flagellated phenotypes. The dynamics of the levitating bacteria resembles a self-assembled pump-like structure, comparable to the structure predicted by Nash et al. [198] in their simulations using a lattice Boltzmann in harmonic traps, where they associate the origin of the instabilities to a symmetry-breaking swarm of swimmers.

Moreover, we found that the mean kinetic energy and enstrophy as a function of the confinement strength increases. At strong confinement (20 U_{pp}) the energy and enstrophy values are higher than those exhibited at weak confinement (10 U_{pp}). Note that the values of voltage that we used correspond to those at which the cells are still in levitation, but as the voltage reduces the magnitude of the acoustic forces too. Hence, the transversal confinement becomes weaker, allowing the cells to disperse in the x and y axis, but also, the decrease of the force normal to the surface of the cavity allowed the displacement for bacteria the z-axis generating diluted cluster in the in-plane surface that was analysed. We also found that the velocity distributions showed a shift towards smaller values corroborating the fact than when more compacted bacteria can exhibit swarm-like patches than can swim in the same direction and at higher velocities than the one exhibited by single individuals. The longitude of this swarm.like patches was 20 bodies width.

To probe that the increase of the energy value is due to replication a viability assays is proposed as it could give insight of the initial concentration of bacteria in the cavity after and before the clustering and spreading dynamics.

Lastly, we also presented the first approaches towards the study of the spreading process, i.e. what happens when the acoustic input is withdraw from the cluster in levitation. However we came short, and we consider deeper and better techniques should be used for its better understanding as the phenomenon is quite complex.

Chapter 4

On the feasibility of enhancing biofilm development using acoustic forces

In this chapter, we discuss the possibility of developing biofilms in a manner than challenges the canonical developmental model. In our configuration the surface to which cells normally adhere is not present; instead, the cells remained confined at the pressure nodal plane of a standing wave that is created in the cavity of an acoustic resonator. Thus, we studied if the nodal plane could act as a virtual surface that promotes the primordial cell transition from planktonic to a sessile phenotype resulting in the formation of a biofilm.

As discussed in previous chapters, the primary and secondary radiation forces increase the local density of cells at hot-spots distributed along the nodal plane of a standing wave present inside the cavity of our acoustic resonator leading to the formation of free floating clusters and possibly biofilms. Under this configuration, acoustic forces counter-act the effect of gravity and the energetic hot-spots determine the virtual nucleation points.

4.1 A brief introduction to biofilms

As discussed in the introduction the discovery of biofilms dates back to the late 1600s [199], and since then, a myriad of research has been done to tackle the conundrum biofilm development is. It is widely acknowledged that the planktonic mode of growth does not provide a sufficient picture of bacteria in natural settings but rather an incomplete one [200]. Bacteria, as the social microorganisms they are, tend to live in complex multicellular communities known as biofilms.

A biofilm is an assemblage of irreversibly surface-associated microbial cells enclosed in an extracellular polymeric matrix [24, 200, 201]. Biofilm-associated microorganisms differ from their planktonic counterparts; for example, the genes that are transcribed are different [24, 58, 200], cells elongate, their mean velocity changes and as a consequence their tumble rate decreases[36]. These take place when the cells happen to be run-and-tumblers, when they are not, extra adhesive appendages are expressed [29, 39].

Biofilms are eclectic communities, their composition depends on the environment they inhabit; biofilms in water systems may contain corrosion products, clay material and freshwater diatoms [202], unlike biofilms in medical devices that normally contain coccoid organisms and extracellular polymeric substances (EPS) [24, 58, 203], or aquatic biofilms (air-water interface)that contain pieces of wood, small dead animals and plants [204, 205].

The accepted model of *in-vitro* biofilm development addresses the attachment of single planktonic bacteria cells to surfaces and the subsequent maturation into a multicellular three-dimensional structure [58, 186]. In real-life scenarios, such as ecological niches and infections, cells clump as multicellular aggregates and later can be attracted to surfaces. These aggregates can also be found when they slough off from a surface-attached biofilm, drift away and re-colonise a new surface [23, 206].

An excellent example of aggregates that arise from a surface-attached biofilm, and are also considered a new kind, are bacteria streamers. Also known as "free floating biofilms" that can appear in environments where a flow is present, like rivers or tubing [207–209]. As discussed earlier in the introduction under these conditions, the flow-induced shedding of extracellular matrix from the surface-attached biofilm generates a sieve-like network that captures cells and other biomass. It has been demonstrated that they affect the flow through porous materials [26]. In addition, free-floating aggregates have a profound effect on surface-attached biofilm development, out-competing the biofilm population arising from single cells attachment [206].

In the previous example, surface colonisation takes place prior to streamers formation [209]. In open sea or in any other air-water interface system, the seeding process begins around small particles of diverse material or around biofilms-chunks that were detached from a surface-attached biofiol and dispersed into the bulk suspension. [203, 210].

‘

4.1.1 *In vitro* biofilm development

In general, the systems that are used to study biofilms are either based on the surface attached growth of microbes under shear stress, the embedded growth of bacteria in a microfluidic agarose channel [211] or the recollection of biofilms produced in the air-water interface on a flask in a rotary shaker [212]. While these standard assays have enabled the identification of several genes involved in biofilm development [213, 214] the importance of the geometry and topology of the surface [59] and the long-distance electrostatic communication between bacteria [215, 216]. sometimes, biofilms form under very different conditions.

4.2 *Escherichia coli* biofilms

In biofilm research the most studied micro-organism is probably the opportunistic pathogen *Pseudomona aeruginosa* [32]. Nevertheless, *Escherichia coli* has also served as model organism for studying biofilm development, plenty of the genetic analysis in biofilms has been performed using *E. coli* as model microorganism. There are some advantages that *E. coli* presents when compared with *P. aerugionsa*; for example, the cells can be handled in the laboratory with relative ease and its genetic background is well characterised [217, 218]. Also, in addition to the harmless *E. coli* serotypes, [219, 32]. Therefore, its study and the understanding of the role they play is important to prevent biofilm-related casualties and to find new strategies to combat infections.

The biofilm formation of *Escherichia coli* and other self-propelled bacteria involves several stages, (i) transport, (ii) initial adhesion, (iii) substrate attachment, (iii) micro-colony formation (cell-cell adhesion) leading to mature biofilms and (v) dispersion, see Figure 4.1.

Primary adhesion to surfaces: reversible attachment

The first step in biofilm formation consists on the transport of the organisms to a solid surface [182, 221]. This can occur via the self-propulsion of the micro-organisms, diffusion of the bacteria cells through the environment, or natural or forced convection in the system [186]. The adhesion of bacteria to abiotic surfaces is highly dependent on physicochemical and electrostatic interactions between the bacteria envelope and the substrate, usually conditioned

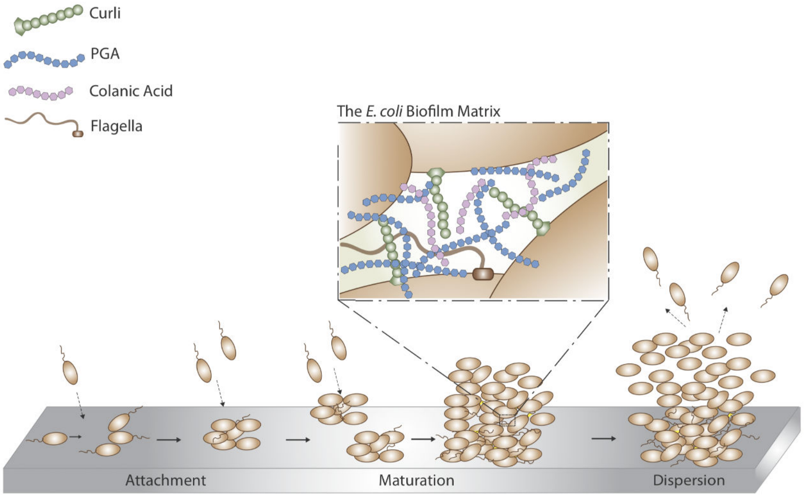

Fig. 4.1 **The phases of biofilm formation in *Escherichia coli***. Biofilm formation involves the attachment of planktonic cells at the surface (irreversible attachment phase), where cells aggregate and bacteria-surface interaction is strengthened by diverse adhesive organelles. Inter-bacterial adhesion leads to a progressive built of microcolonies and the excretion of EPS. Later, microcolonies mature into biofilms where cells form multi-layered clusters. Three-dimensional growth of the biofilms and its further maturation provides protection against host defence mechanisms and antibiotics. Later, the biofilm reaches a critical mass and planktonic bacteria living on its surface disperse to the surrounding areas ready to colonize other surfaces [220].

by the fluids to which the surface is exposed [32, 39].

The outer cover of both Gram (+) and Gram (-) bacteria is negatively charged [222]. In the case of Gram positive bacteria the negative charge is due to the presence of teichoic acids linked to either the peptidoglycan or to the underlying plasma membrane of the cells [223]. For Gram negative bacteria the charge is a consequence of the phospholipids and lipopolysaccharides of its outer cover [222]. The repulsive or attractive forces lead to reversible attachment of bacteria to the surfaces, with most of them leaving the surface to join the planktonic-phase community in the bulk either due to the shear stress or their own propulsion [224]. Ionic forces of the media and temperature also play an important role in this first step towards biofilm development [225]. Recently, it has been shown that the topology and wettability of the surface also impacts the first attachment, where rugosity increases surface adhesion and hydrophobic surfaces are more likely to be colonized than hydrophilic ones [58, 59].

Irreversible attachment

Once the organisms approach to the surface, physical interaction forces are thought to influence the initial adhesion of organisms. The interactions that can take place include Van der Waals interaction (>50 nm from the surface), repulsive or attractive electrostatic interactions (2-10 nm from the surface) and hydrophobic interactions (0.5-2 nm from surface) [226].

Van der Waals forces are due to dipole-dipole, induced dipole-dipole, and induced dipole-induced dipole interactions and are always attractive [227]. Electrostatic interactions comprise the interaction of the negatively charged surface of the cells and the surface which can be negatively or positively charged. Lastly, hydrophobic interactions between the cell membrane and the solid surface may be responsible for overcoming repulsive electrostatic forces. The origin of hydrophobic interactions is thought to be enthalpically driven, that is, the exclusion of water molecules between the two surfaces and the direct interaction of the bacteria and substrate surface is believed to lower the overall free energy of the system [228]. As a result bacteria adhere irreversibly.

The irreversible attachment to substrates corresponds to the main developmental step in biofilm formation. The transition of planktonic, often motile, to a sessile phenotype promotes the expression, or over expression, of adhesive organelles of the fimbriae family which contribute highly to the surface attachment [32]. Apart from the aforementioned organelles, flagella are also known to play an important role in the instantaneous attachment to surfaces [229]. It has been proved that deflagellated mutants attached to stainless steel surfaces at levels that were 10-fold lower than that for motile cells (flagellated cells) at short incubation times. However, at longer periods the surface coverage is similar for both phenotypes [226]. In respect of the fimbriae family organelles, three have a role in strengthening the bacteria-to-surface interaction:

i. Type 1 fimbriae or pili

Pili is a filamentous proteinaceous adhesin with tubular structure (5 nm x 2 µm) that can adhere to a variety of receptors molecules on the surface of eukaryotic cells. The presence of pilis is critical for biofilm formation in *E. coli* as it impacts the initial attachment to the surfaces and also can modify the composition of the outer membrane [32].

ii. Curli fimbriae or aggregative fimbriae

Curli aggregates at the proteins embedded in the cell surface, such as fibronectin, laminin and plasminogen, to form 6 nm diameter structures with 1 µm*m* lengths promoting the adhesion of bacteria to different cells. In addition, curli facilitates initial cell-surface interactions and subsequently cell-cell interactions impacting deeply in biofilm development. [32, 230, 231]

iii. Conjugative pili

The conjugative pili promote both initial adhesion and biofilm maturation stabilizing the structure of the latter [32].

Microcolonies proliferation

After the initial adhesion takes place bacteria begin to anchor themselves to the surface by synthesizing extracellular polymeric substances (EPS) like polygalacturonic acid (PGA) and colanic acid that facilitate irreversible bacterial attachment to the surface [32], see Figure 4.1. At this moment, inter-bacterial adhesion rather than direct contact with the surface leads to progressive build up of the mature biofilm [232]. Within the structure there are networks of vertical and horizontal channels to allow liquid flow to guarantee supply of nutrients and disposal of waste products that are generated as part of the natural respiratory activities of cells [74]. The composition and structure of the three dimensional matrix can vary greatly depending on the microorganism(s), their physiological status, the nutrients available, and the physical conditions [58, 186] where they are formed.

Mature biofilm

Biofilm maturation corresponds to the three-dimensional growth of the adherent colonies or aggregates. This takes place once the local density increases [233]. Mostly due to bacterium-bacterium interactions, this process leads to the formation of a heterogeneous physicochemical environment in which biofilm bacteria display characteristic physiological traits that distinguish them from their planktonic counterparts [32]. A general feature of mature biofilms is their highly heterogeneous architecture that partitions the microbial city into sectors with specific micro-environments. [233]

Dispersal

After maturation of the colonies individual cells or small aggregates disperse due to several factors such as the lack of nutrients, intense competition, outgrown population, among others [32]. The dispersion step is very important for the biofilm life cycle as these biofilms chunks will detach and drift away to colonize a new surface [58].

4.2.1 The impact of motility on biofilm development

There is evidence that shows that interfering with motility and its regulation results in changes in biofilm formation in several bacteria species [234–238]. Indeed, some *E. coli* strains with impaired motility exhibited reduced surface attachment and failed to develop biofilms, but even when this proves the importance of motility on biofilm development non-motile strains are able to develop biofilms using other mechanisms [220, 237, 238].

As discussed in Chapter 3 the motility of *Escherichia coli* is mediated by flagella that propel the cells forward in aqueous environments, where cells swim [239], and on surfaces where they swarm [240]. The key player in motility's regulation is the second-messenger c-di-GMP, which controls negatively flagellar motility via motor curbing and it is a positive regulator of biofilm matrix production. The matrix is required for biofilm maturation. The second-messenger reduces flagellar motility while it increases the production of EPS [241–245]. There is an interplay between the genes involved in motility and biofilm formation [246, 247], it has been showed that both short-term and long-term motility inhibition is quite important to stabilize cell aggregates and optimize resources investment within biofilms [248].

4.3 Models for exploring bacteria microenviroments

The development of simplified models to study how bacteria, including pathogens, can form biofilms started right after the demonstration of a link between sessile communities and human infections. The link was proven by the pioneer studies by A.T. Henrici [19], in the early 20th century, and later by J. W. Costerton [249, 250] pointed to the existence of populations of microorganisms living on surfaces.

In vitro **biofilm models**

Multiple *in vitro* models have emerged from scientists' creativity, each of them are especially adapted to observe biofilm formation of specific bacteria and within specific environments. A complete and comprehensive list of *in vitro* biofilms models is provided in the very detail work by Lebeaux [251]. In general, *in vitro* biofilm models can be classified in three distinct groups:

i. Closed or static models

This type of model corresponds to the one in which there are limited nutrients and aeration. It includes some of the most popular and successful models, such as the colony biofilm model and microtiter plates. In addition, these models enable direct rapid quantification of biofilm mass (see Figure 4.2A and B) [252, 253].

ii. Open models

The principle behind these models is similar to the one in continuous cultures, in which spent culture, consisting of wastes, metabolic by-products and dispersed and dead cells, are constantly replaced by fresh medium. These methods generally allow the control of environmental parameters, such as shear forces. Hence they have been extensively used to study the physical and chemical resistance of biofilms as in Figure 4.2C [253].

iii. Microcosms

Microcosms are the most sophisticated models, which aim to closely mimic *in situ* conditions. They often include several bacterial species and use material from the studied environment. For instance, the addition of hydroxyapatite and saliva enhances the modelling of dental biofilms [254], or covering abiotic surfaces with human cells in order to mimic an *in vivo* situation [255].

***Ex vivo* biofilm models.**

Midway between *in vitro* and *in vivo* lie the *ex vivo* models. Typically the models consist of tissues or organs that are extracted from macroorganisms (typically porcine or murine) and are placed in an artificial environment for further analysis and experimentation. They can be particularly useful to image or analyse the progression of bacterial colonisation of a given organ or tissue, such as tracheal epithelium, vaginal mucosa, kidneys or teeth [251].

***In vivo* biofilm models.**

Infection and pathogenesis result from a continuous interplay between the host and microbes and between microbes themselves influencing and determining the fate of infection. The complex dynamics makes difficult the use of *in vitro* models. To overcome this, non-mammalian models like the fruit fly, *Drosophila melanogaster*, or the zebrafish *Danio rerio*, have been adapted to study host-microbe interactions and immune system responses. There are also models where tissue can be present to make it more realistic [251].

All the methodologies described earlier have been proven to be quite effective to evaluate physical, chemical and genetic properties of biofilms. Also, they provide a robust technique to evaluate new drugs against persistent and resistant bacteria associated with biofilms and some major diseases.

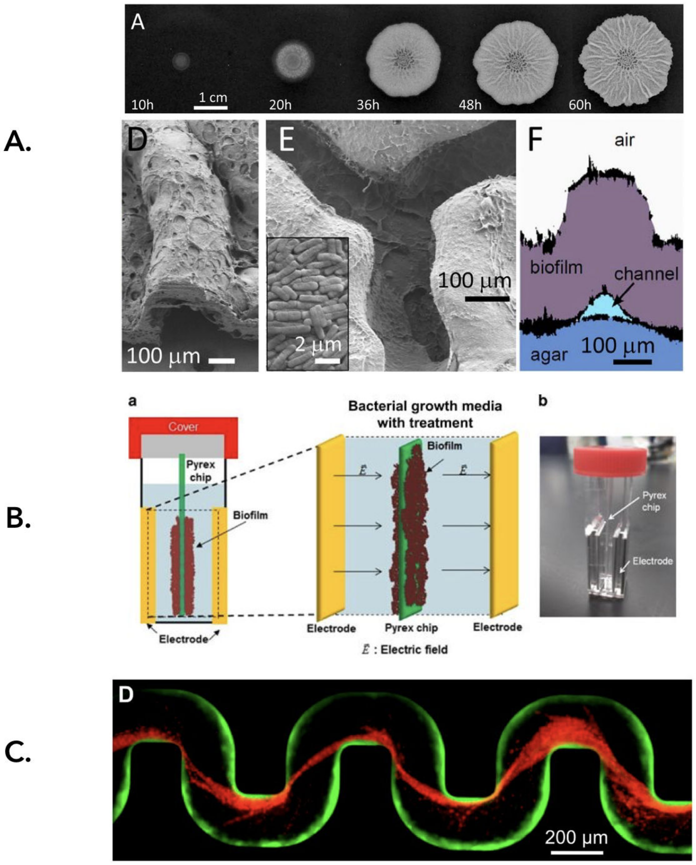

Fig. 4.2 ***In vitro* microenviroments to study biofilm development**. **A.** Closed model; agar plates are the most popular technique to evaluate biofilm development. The picture shows a *Bacillus subtilis* biofilm growing on the surface of an agar gel containing water and nutrients. The biofilm increases in height to hundreds of micrometers, later spreads to reach a diameter of several centimetres and forms macroscopic wrinkles. This techniques have allowed the characterization of channels within the biofilm [256]. **B.** Schematics of a static model. Glass chips/coupons placed inside electroporation cuvettes were *E.coli* biofilms developed. This technique was used to evaluate the electrical energy to treat biofilms using a bio-electric effect [257]. **C.** A clear example of an open model is a microfluidic channel used to evaluate, in this particular case, the formation of free-floating biofilms of *P. aureoginosa*. [26]

4.4 Shaping free-floating biofilms using acoustic forces

In Chapter 3 we found that the acoustic trapping of bacteria is a technique that is phenotype independent, i.e. we were able to manipulate motile and non-motile bacteria; also the effectiveness of the technique does no depends on the strain of bacteria.With guidance on the spreading dynamics results (see Figure **??**) that showed an irreversible attachment of cells within the cluster formed with the non-motile phenotype we decides to evaluate if it is possible to observe the same adhesion with motile cells over-expressing adhesion organelles related to biofilm development. Therefore by the end of this work we would have explored the feasibility of biofilm formation in levitation with motile and non-motile cells.

4.4.1 Model microorganisms

It is well-documented that the self-propulsion of bacteria and the adhesive organelles of the fimbriae family strengthen the attachment and development of biofilm on surfaces [241–245]. To study the likelihood of enhancing free-floating biofilm development using acoustic forces, two motile *Escherichia coli* K-12 MG1655 strains were selected.

***Escherichia coli*MG1655_IATT*gfp_ompR234_malA*::Km**

Escherichia coli K-12 strain carrying the mutant ompR234 allele. The mutant OmpR protein activates expression of CsgD, a transcriptional activator of the *csgA* gene, resulting in an increase in CsgA protein levels and promotion of biofilm formation. This strain typically clumps due to the over-expression of the curli gene.

***Escherichia coli*MG1655_IATTamp*gfp_ompR234_malA*::Km_csgA::aadA7**

Escherichia coli K-12 strain carrying the mutant ompR234 allele with a knock-out of *csgA* gene resulting in a phenotype with loss of adherence. This strain does not clump as it is a *csgA* mutant.

To avoid writing the complete name of the strains we re-name theme as:

***E. coli* CsgA+** for *E. coli*MG1655_IATT*gfp_ompR234_malA*::Km.

***E. coli* CsgA-**: *E. coli*MG1655_IATTamp*gfp_ompR234_malA*::Km_csgA::aadA7.

4.5 Methods

4.5.1 Experimental protocol

Planktonic cultures

E. coli (csgA+) and *E. coli* (csgA-) cells were streaked in LB agar plates (Sigma) with Ampicillin (50 µg/ml) and incubated overnight at 30° C. The following day, two isolated colonies of a given strain were picked from the plate, re-suspended in 5 ml of LB broth (Miller) and incubated overnight at 30°C on a rotary shaker at 250 rmp. Fourteen hours later, a fresh culture ($A_{600} = 0.05$) was re-started and incubated under the same conditions until mid-exponential phase ($A_{600} = 0.5$). Later the liquid culture was diluted five times ($A_{600} = 0.1$). The diluted suspension was used to inoculated, it has an approximated cell density of $1X10^8$ CFU/mL according to the McFarland standard, see Figure 4.3A.

Inoculation of the cavity

The acoustic resonator–previously sterilised via ultraviolet germicidal irradiation–was inoculated with 500 µl of the suspension and sealed with the reflector lid. In parallel, another acoustic resonator, with the same dimensions and also sterile, was inoculated with the same volume, sealed with the lid and placed on the bench, as depicted in Figure 4.3B. The second resonator (R_C) is the control to validate the experiments.

Acoustic trapping protocol

Forthwith, the first resonator (R_{Exp}) was placed in the microscope stage and a 30 s video was recorded, as a control of the motility of cells and to measure the velocity distribution of the bacteria cells. Right away, the sample is exposed to a continuous sinusoidal signal, that matches the driving frequency of the used transducer at 20 U_{pp}. When possible, a video of the clustering process was acquired, see supplementary movie 1 of [193] . Bacteria cells were acoustically confined for 20 minutes, the time typically required to get a stable aggregate. Immediately afterwards, based on the same conditions stated in Chapter 2, a cluster is chosen and a video to evaluate the dynamics within the cluster is captured. Next, the total area of the cavity is scanned to record all the aggregates that are formed at the nodal plane. The chosen cluster is later freed from the acoustic trap and the release up to the sedimentation towards the surface of the cavity of our acoustic trap is recorded. Once at the surface, the temporal evolution is evaluated for up to one hour. Finally, the distribution of bacteria in the surface is assessed to be later compared to that obtained in the control resonator (R_C) (Figure 4.3C).

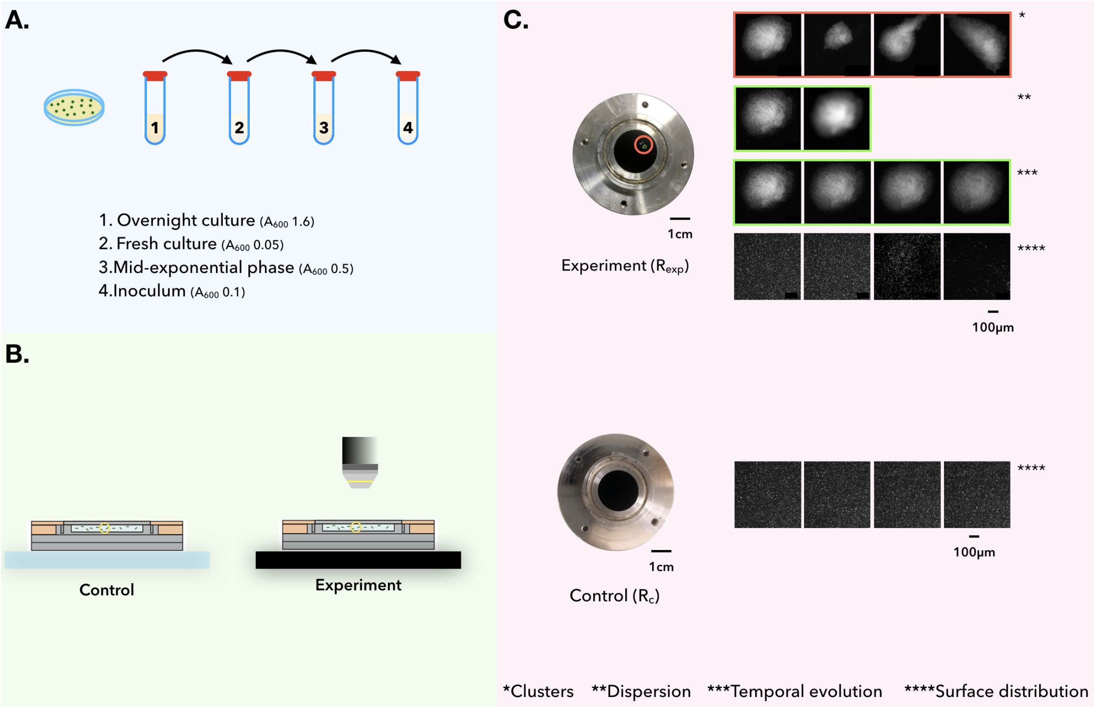

Fig. 4.3 **Experimental protocol to study biofilm formation in levitation. A.** To prepare the inoculum the chosen bacteria strain is streaked in LB agar plates and incubated overnight at 30°C. Afterwards, a single isolated colony is picked and re-suspended in 5ml of liquid LB and incubated overnight in a rotary shaker (30°C and 250 rpm). The following day, a fresh culture is re-started and incubated under the same conditions until it reaches mid-exponential phase. The latter is diluted five times to prepare the suspension to inoculate the cavity of the resonator. **B.** Two resonators are inoculated with 500 μl of the suspension and sealed with the lid holding the reflector. The control is placed on the bench and the other resonator is placed immediately on the stage of the reflected light microscope. **C.** Forthwith, the typical run-and-tumble behaviour of *Escherichia coli* is recorded–this video allows the quantification of the velocity distribution of the cells in the sample. Right away, the sample is exposed to a continuous sinusoidal signal, that matches the best driving frequency of the transducer at 20 U_{pp}, and, when possible, a video of the clustering process is acquired. Bacteria are acoustically confined for 20 minutes and, based on the same conditions stated in Chapter 2, a cluster is chosen and a video to evaluate the dynamics within itself is captured. Next, the total area of the cavity is examined and all the clusters at the nodal plane registered in video. The acoustic input is withdrawn, the sedimentation of the elected cluster is followed up and the temporal evolution of the cluster in the surface as well. To conclude, the distribution of bacteria on the surface of the cavity is compared to the one of the control resonator.

4.5.2 Clustering and dispersion

As previously established, bacteria cells inside the inoculated cavity were distributed homogeneously and, when motile, they swim with their standard (run-and-tumble) motion. They moved in this manner until the acoustic radiation force dragged them in the direction of the pressure node of the standing wave created by the interference of the emitted and reflected waves. The cells at the pressure node are also subject to the secondary force and to the transverse component of the primary radiation force, these forces promote the consolidation of the cluster.

As described in Chapter 3, at this point bacteria are not interacting with any surface, rather, they gathered in a virtual one created by the pressure minimum and a free-floating cluster is formed. The nucleation points where the clustering takes place are given by the energy hot-spot on the cavity of the resonator.

Once the bacteria cluster was consolidated, typically after 20 minutes, unless stated the contrary, the acoustic input was removed and the bacteria were free to disperse in all the volume or maintained attached if they have a strong bond due to adhesive forces. To characterise and quantify the dynamics of these phenomena the radial distribution of mass was calculated following the same protocol as in Chapter 3. We recall that this function is typically used to study the nucleation and aggregation on granular systems [196].

4.5.3 Temporal evolution on the bottom surface of the cavity

Once the floating-cluster settles on the surface of the acoustic cavity the evolution of its area was assessed over time. In this temporal evaluation time zero is considered as the moment when the cluster reaches the surface and it is on focus. At this moment a first picture was taken and every five minutes another one, we repeated this process up to one hour. All the pictures were acquired with an Hamamatsu Orca Flash 4.0 camera, fixing both, the exposure time at 1 second and the focal plane in the surface of the cavity. The latter implies that if some part of the cluster becomes out of focus: a vertical growth or a shrinking of the cluster is taking place leading to protrusions in the z-plane.

Afterwards, the obtained images sequence was processed using a in-house-made Matlab algorithm, based on the image analysis algorithm already existing in the software. The 8-bit gray scale images were binarized using Huang's fuzzy threshold method, as it has been proven robust in the analysis of bacteria isolates on agar plates [258]. The cut-off gray scale value was set at 33, that is, every pixel with and intensity value lower than 33 is considered as background, whilst the pixels with higher intensity are taken as foreground as depicted in Figure 4.4. The area of the binarized cluster was measured and its pixel value transformed into µm^2 using the proper scale. This methodology was used for all the experiments made using all the model strains in this section. Note that the cut-off value was the same for all experiments, unless stated otherwise.

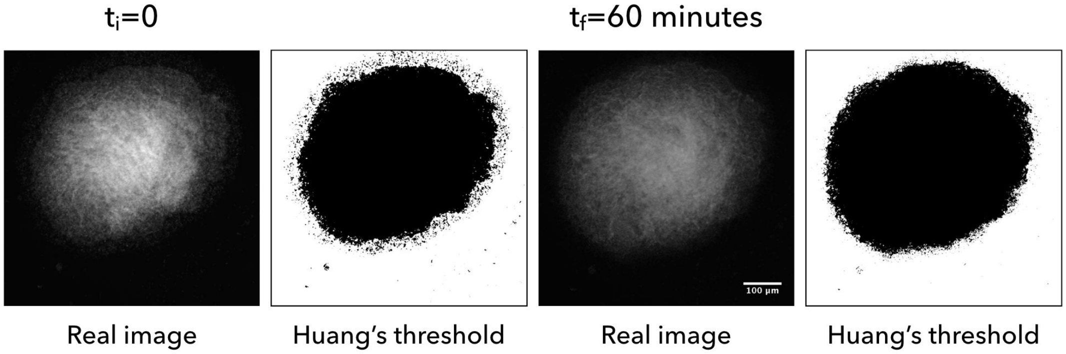

Fig. 4.4 **Estimation of the area temporal evolution using Huang's threshold method**. Every five minutes pictures of the cluster, settled on the surface of the acoustic resonator, were taken using the image acquisition component of the experimental set-up. The exposure time of was fixed at 1 second. The gray-scale images were binarized using Huang's fuzzy threshold method. The cut-off value was 33, such that every pixel less than 33 is considered as background, while the pixels with a greater intensity value are foreground. The area of the cluster is measured for all the images.

4.5.4 Density distribution on the bottom surface of the cavity

To have a quantitative idea of the distribution of the energetic hot-spots (i.e. places where the gathering of bacteria took place) along the bottom surface of the cavity we analysed the density distribution—as in intensity of pixels distribution on the cavity. First, we divided in thirty-six regions the total surface area of the resonator (Figure 4.5). The area of the resonator can be 3 cm^2 or 5cm^2 depending on the type of resonator that was use, see2.8; the area of each one of the 36 regions is 0.138 cm^2. Within each regions a picture is taken, covering an area of $4.48 \times 10^{-3} cm^2$ that corresponds to 3% of the total area of the each region. Therefore, after the pictures in each regions have been photographed the covered area is approximately 6% of the total surface of the cavity. The same procedure is performed in the control resonator; therefore, seventy-two images are acquired per experiment.

Later, all the images are processed using the Matlab image analysis algorithm. The 8-bit gray scale pictures are binarized using Huang's fuzzy threshold method, with an specific cut-off value depending on the experiment. The pixels occupied by bacteria are then transformed into white pixels and the background corresponds to black pixels. Afterwards, also with a Matlab algorithm, the number of white pixels, corresponding to bacteria cells, is counted and the ratio occupied by bacteria is registered.

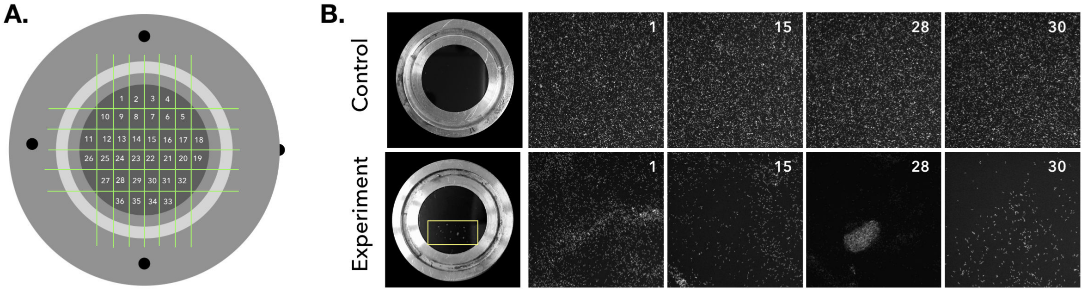

Fig. 4.5 **Density distribution on the cavity surface**. **A.** Schematics of a layered acoustic resonator. The surface-area of the cavity is 3 cm^2, which is divided into 36 regions to ease the mapping of the bacteria cells distribution after the cells are acoustically confined. **B.** For all the experiments two acoustic resonators are used; one as a control and other to confine the cells. Once the cells are settled on the surface a picture is taken at each of the regions. The area covered per picture is 4.48×10^{-3} cm^2 (1024×1024 px), hence, the mapped 36 regions covered a surface area corresponding to a 6% of the total. Later the distribution of both resonators is compared.

4.6 Results

4.6.1 Clustering

The clustering and spreading dynamics observed for $E.coliCsgA+andCsgA-$ differ greatly when compared to the ones observed for Jovanovic MG1655 motile bacteria. Firstly, it is important to know that the two model strains used in this section, considered as motile [], did not exhibited a run-and-tumble behaviour, rather, they acted as passive particles even when they have working flagella, they do however, exhibit Brownian motion. This was analysed by tracking their displacement with a basic 2D-tracking method using Fiji and Matlab. Their lack of self-propulsion can be explained considering that the adhesive organelle curli, that is over-expressed in CsgA+, impacts the motility of the cells typically reducing it or transforming the cells into a sessile phenotype variant. [32]

Nevertheless, even when the bacteria did not displayed the expected self-propulsion their confinement using acoustic forces was possible. The clustering process for both strains was similar to the one observed for non-motile Jovanovic cells.

As mentioned in Chapter 3, the recording of the clustering process always represents a challenge. The difficulty lies in the fact that we cannot accurately predict the spot where the aggregation would take place making the recording of the forced phase transition sometimes impossible. In this particular case the over-expression of CsgA in *E.coli* promotes the clumping of cells within the inoculation suspension; for that reason, once the cavity is inoculated the apparition of instantaneous clusters may take place.

During the clustering process small clumps of bacteria where transported in direction of the nodal plane and a lot of small floating aggregates arose, see Figure 4.6. The clusters at the nodal plane have a similar size than those formed by the Jovanonic strains. However, in some cases the size of the cluster formed by the strain over-expressing curli (CsgA+) is much larger.

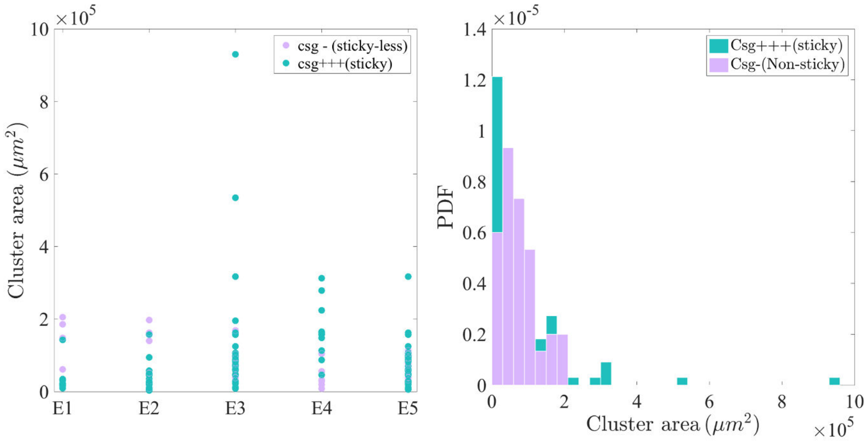

Fig. 4.6 **Measured surface area of the cluster.** Each box represents the distribution of the measured area of the clusters after 20 minutes of trapping. On each box, the central solid line indicates the median of the obtained values, the bottom and top whiskers indicate the 25th and 75th percentiles, respectively. **A.**The size of the CsgA- clusters lies between 0.3 X10^5 to 2 X10^5 μm^2 as for the one previously observed for non-motile cells. **B.** The CsgA+ clusters present a wide size distribution. It is possible to find small clusters with sizes ranging from 0.5 X10^5 to 1.5 X 10^5 up to big clusters with 9 X 10^5 µm^2.

‘

In Figure 3.5 we present a representative example of the clustering of *E. coli* CsgA+ and for *E. coli* CsgA-. The analysed clustering process did not began from a homogeneous distribution of the cells, instead from an already made cluster. This happened due to technical difficulties that implied recording the process for these strains, yet, we corroborated that the bacteria in the cavity were distributed homogeneously prior to acoustic trapping using optical microscopy.

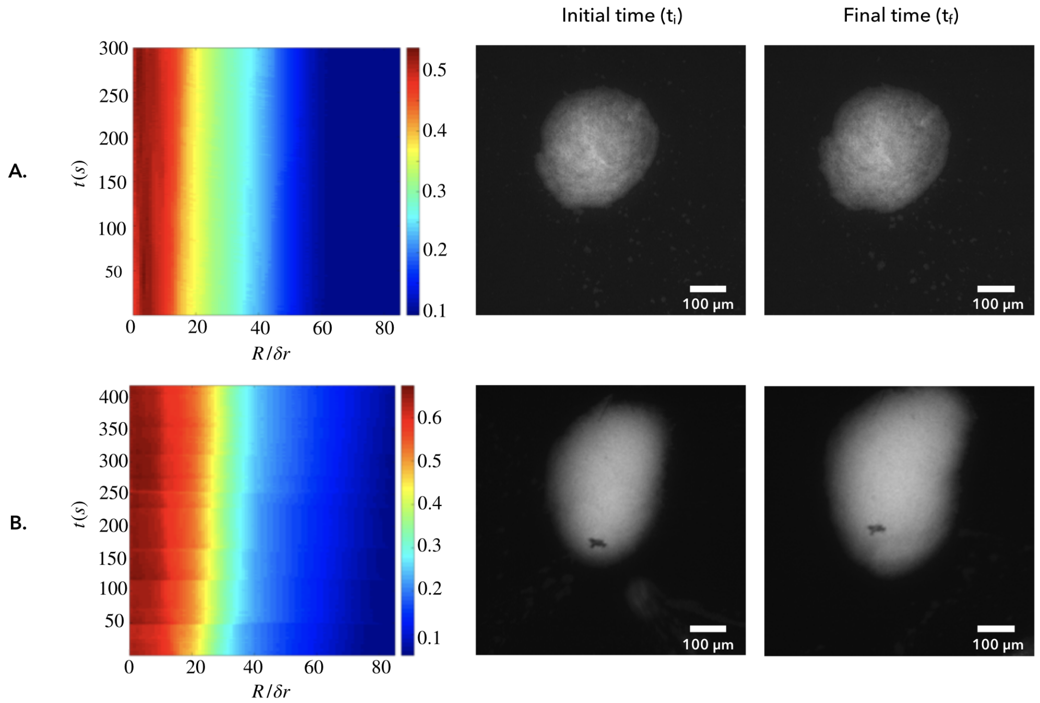

Fig. 4.7 **Examples of the clustering process of *Escherichia coli* CsgA+ (A) and CsgA-.(B)** **A.** The clustering dynamics for *E.coli* CsgA+ started from a initial cluster that has a considerable sized, it could even be considered as a stable one. **B.** For *E.coli* CsgA- the clustering process also started from a cluster of significant size but it grew larger. From the graph we can see that the bacteria distribution in the selected region of interest did not changed dramatically with time. Also, it is evident that the in-plane surface of the clusters differ and this may be due to the phenotype of bacteria.

The in-plane surfaces of the floating clusters of *Escherichia coli* CsgA+ and CsgA- contrast greatly, pointing that the observed characteristics are phenotype dependent, see Figure 4.8.

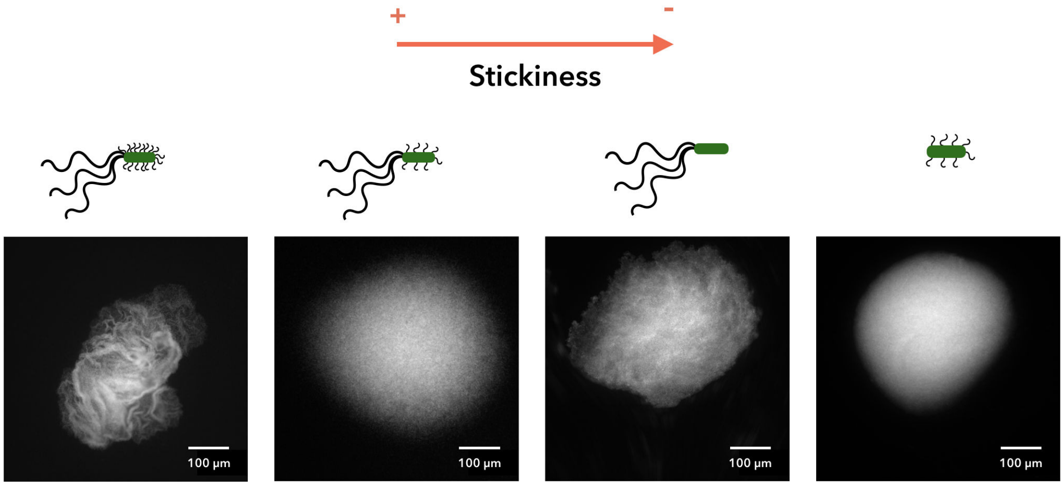

CsgA+ Jovanovic motile CsgA- Jovanovic non-motile

Fig. 4.8 **Cluster obtained with strains with different stickiness.** In-plane micrographs of typical clusters of different strains of bacteria after 20 minutes subject to acoustic confinement. The images are organized from the stickiest strain to the least.

We considered that adhesiveness of bacteria affects their clustering. For example, the stickiest strain (CsgA+) is a motile strain that over-expresses curli whose floating clusters exhibit wrinkled surfaces. The wrinkled surface is in accordance to the wrinkled surfaces observed biofilms evaluated on agar substrates [259]. The second most adhesive (Jovanovic motile) strain presents a smother surface with no visible wrinkles. The OmpR234 mutant (CsgA-) shows a more compact and not so rough surface when compared with its counterpart, the CsgA+ phenotype. Finally, the least adhesive (Jovanovic non-motile) displays a compact and smoother surface. The higher compaction could be due a consequence of its lack of flagella. As we discussed previously flagella and curli play a relevant role in surface colonization and biofilm development. In our experiments the over-expression of the adhesive organelle (curli) resulted in a decreased motility of the cells and adherence between them (cell-cell adhesion). The changes in the surfaces roughness could be explained by the presence or absence of curli and flagella in the membrane of bacteria.

Another phenomenon that appears to be phenotype-dependent is the number of floating clusters that are formed under 20 minutes of acoustic confinement. The stickiest strain produces on average 11 clusters per experiment, whereas, as showed in Chapter 3, motile cells formed from 3 to 4 clusters. Both CsgA- and Jovanovic non-motile cells formed 10 aggregates on average. We found that the clusters of CsgA+ occupied the 0.6% of the total surface cavity whereas CsgA- clusters only the 0.2%. The clusters formed by the Jovanovic non-motile bacteria is the 0.3% and for the clusters of the Jovanovic motile strain only 0.1%.

The contrast in the number of aggregates for each strain can be explained by the fact that in order to confine motile cells a higher magnitude of energy is necessary. Motile cells can exert an "active pressure" on the virtual walls of the confinement [260]. In our case, this so-called active pressure could counteract the effects of the transversal acoustic forces enabling bacteria to escape and to not be easily trapped. Also, as mentioned before, the acoustic forces can produce a stronger effect on a small cluster with higher surface than over single beads or cells. In the case of the non-motile Jovanovic and the CsgA+ and CsgA- phenotypes the clumping of cells is inevitable. Hence, the emergence of clusters with surface area bigger than that of single motile cells facilitated their capture at the nodal plane, which is in agreement with the acoustic forces theory **??**.

4.6.2 Spreading

The spreading process is similar to the one exhibited by non-motile bacteria, described in Chapter 3 **??**. When the acoustic input is removed from the acoustic trap the cells within the stable floating cluster did not diffuse back into the bulk, on the contrary, they remained entangled and sedimented towards the surface of the cavity. In Figure 4.9 we can see this phenomenon for both strains CsgA+ (A.) and CsgA- (B.).

It is important to remark that the turbulent behaviour observed for motile cells it is not displayed for these strains. This is a reaffirmation of the significant role played by motility on the emergence of this phenomenon.

So far we have shown that CsgA+ and CsgA- strains have flagella but are not motile. Probably, because the second-messenger c-di-GMP is controlling negatively flagellar motility and positively the expression of the adhesive organelles [39]. Surprisingly, after only 20 minutes of acoustic confinement consolidated clusters are formed at the pressure node. When the acoustic forces are no longer exerted on them the cells within the clusters do not disperse back into the bulk. A similar behaviour is observed for cluster formed by the non-motile strain, which makes sense, since CsgA+ and CsgA- exhibited down-regulated motility.

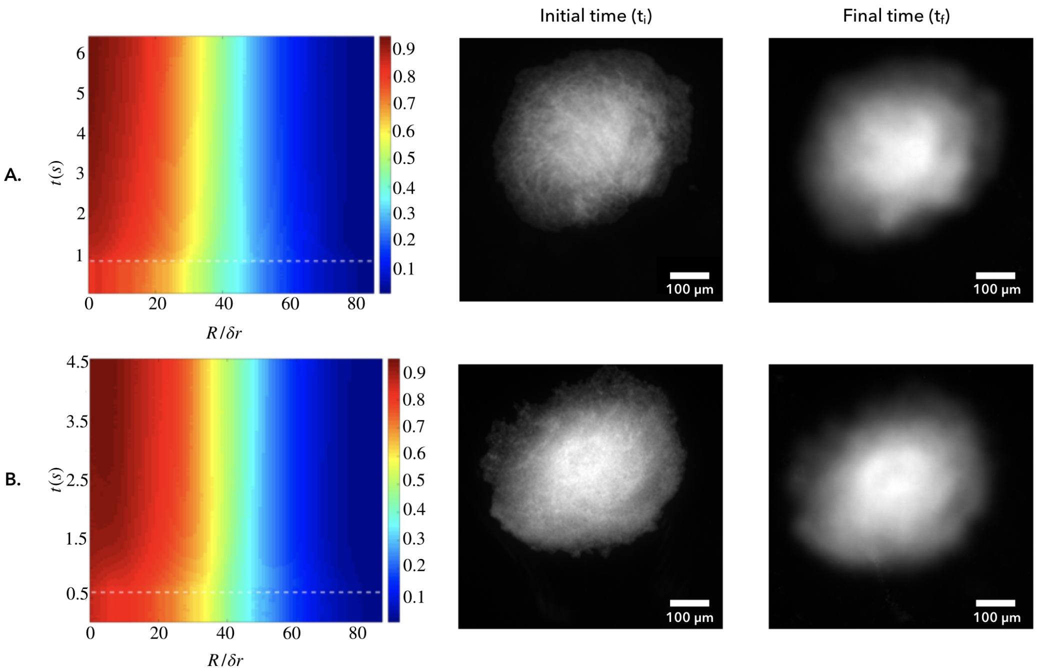

Fig. 4.9 **Spreading process of *Escherichia coli* (CsgA+) and (CsgA-)**. The spreading dynamics of both strains *E. coli* (CsgA+) **(A.)** and *E. coli* (CsgA-) **(B.)** exhibited the same dynamics as non-motile cells. The floating cluster (initial time) remained consolidated until the acoustic input was removed. Later the cluster followed sedimentation towards the surface of the cavity (final time).

Since the cells within the floating cluster do not diffuse back into the bulk we could say that we are dealing with a free-floating biofilm-like structure, where the adhesive forces maintain cells entangled. We think that this process is mediated by curli and flagella on the surface of these cells.

4.6.3 Temporal evolution on the surface

To evaluate the temporal evolution of the sedimented clusters five experiments per strain were performed. Note that we only performed this analysis for CsgA+, CsgA- and Jovanovic non-motile since only with those strains the cells within the cluster remained entangled allowing the sedimentation of the cluster. For all experiments it took less than a minute for the floating biofilm-like structures to sediment on the surface of the cavity.

From the temporal evaluation we found out that once the cluster reached the surface they did not disintegrated, see Figure 4.10. On the contrary, the cells remained entangled maintaining the initial shape. In some cases, cells were able to swim away leaving diluted cluster.

Even when it is hard to determine if the biofilm-like structure is still growing on the surface by just analyzing the temporal evolution of area density ρ_A in Figure 4.10, we see that ρ_A grows with time for all the biofilms. For example, one cluster formed with CsgA+ cells (Figure 4.10A.) presented 3% growth from its original size at levitation to its size when it reached the surface. After 60 minutes the cluster expanded 22% from its initial size at t_i. On the other hand, CsgA- clusters presented the same initial growth (3%) and it increased to 27% after one on the surface,see Figure 4.10B. Finally, clusters formed with non-motile cells exhibited a minimum of 2% and a maximum of 20%.

Unluckily, these minimal variations of growth for the different strains do not tell much about the impact of flagella or the over-expression or knockout of curli in the dispersion or growth on the surface. In order to have a clearer result a cellular arrest should be made, preventing the division of bacteria cells, so we could then conclude if the expansion of the clusters on the surface is due to dispersion of cells or cellular division and maturation of the biofilm.

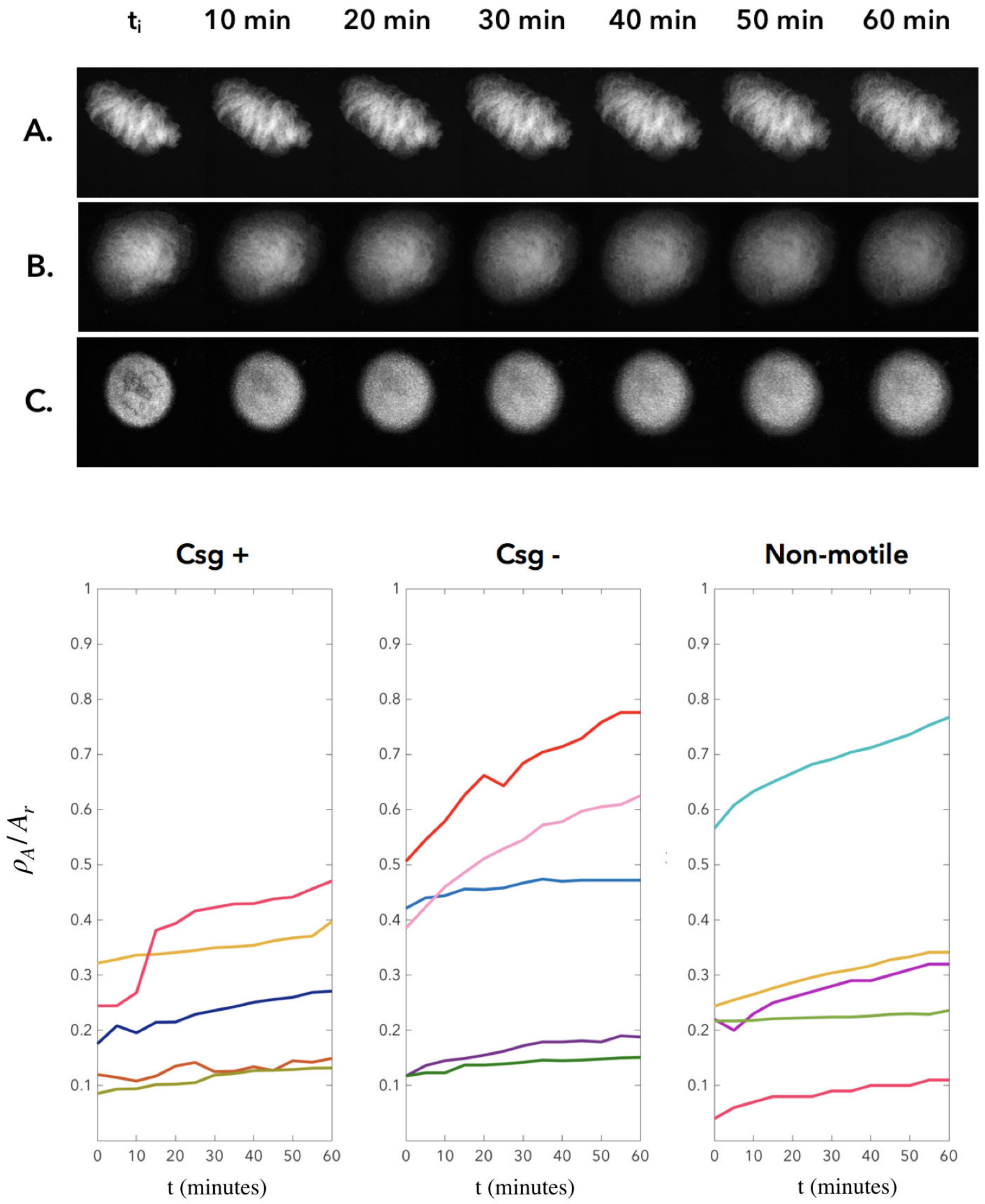

Fig. 4.10 **Temporal evolution of aggregates on the surface. Top panel.** Images showing the evolution of the sedimented cluster on the surface of the cavity at t_i up to one hour (A). A typical wrinkled cluster of CsgA+ did not disaggregate and kept its shape after one one on the surface, as it also occurred with the representative cluster of CsgA-(B) and Jovanovic non-motile strain (C). **Bottom panel.** The temporal evolution of the area density ρ_A, normalized with respect to the total area of the region , the area of the image in pixels (A_r), of the three strains shows that there is and increase of the aggregate size with time in all five replicates.

4.6.4 Density distribution on the cavity surface

The biofilm-like clusters are now settled on the surface of the cavity and their temporal evolution has been assessed. As reported in Chapter 1, the acoustic energy distribution in the cavity of our acoustic resonator is not homogeneous. In order to map where the energetic hot-spots were in each experiment we analyzed the density distribution, as in intensity of pixels distribution, on the cavity.

The density distribution in the 36 regions, in which our resonator is divided, showed a significant difference between the control resonator and the resonator used in our experiments. This implies that the distribution of the cells that were not exposed to acoustic fields differs from that where the cells were trapped. Figure 4.11 (B) shows that the density distribution of the control resonator, inoculated with CsgA- cells, was quasi-homogeneous, except in one experiment, whereas the density distribution of the resonator where the confinement took place has maximum at the regions where the cluster were formed. The minimum in the distributions correspond to the regions where the cell concentration (the number of pixels corresponding to bacteria) decreased because bacteria were dragged to more energetic hot-spots.

In the case of the experiments with CsgA+ cells, Figure 4.11(A), the density distribution on the surface of the control resonator is homogeneous and the quantity of cells in all regions is always greater than that of the surface of the resonator where the trapping took place. The fact that we do not have, in any region or experiments, peaks representing higher density on the treated cells than on the control tells us that the biofilm-like clusters are on zones that we could not map with our technique.

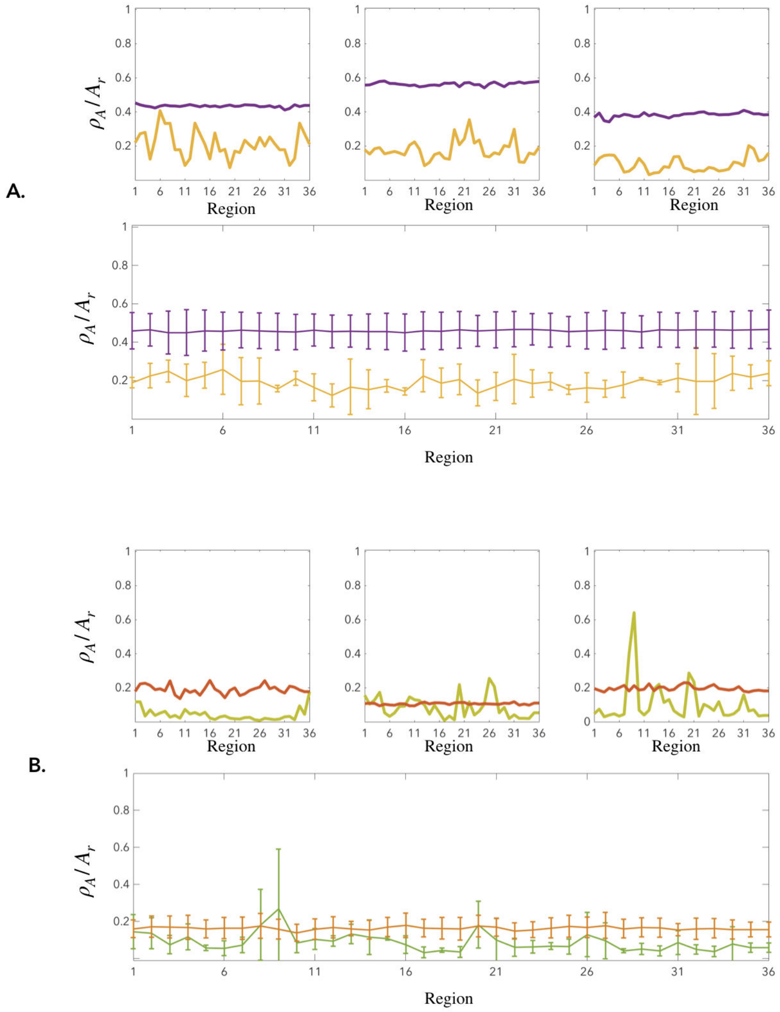

Fig. 4.11 **Density distribution of Csg A+ (A) and Csg A- (B) cells on the surface of the cavity.** Three representative experiments of the density distribution in the control resonator purple lines for the resonator inoculated with Csg A + and orange lines for the resonator inoculated with Csg A-. For the resonators where cells were acoustically confined for 20 minutes and previously release, yellow lines represent the distribution of Csg A+ cells and green lines the distribution of Csg A- cells . In the three cases the distribution on the control is quasi-homogeneous whereas the distribution of the cells treated acoustically showed a decrease in the density at the selected regions (A). For the curli knockout-cells (B) the distribution of the treated cells present peaks depending on the region. These peaks and valleys shows either a increase in the density (peaks) or regions where the density of cells is almost zero in some case. The bottom panel represents the average distribution for the 3 experiments where the error bar is the standard deviation.

4.6.5 Discussion

The formation of biofilm-like structures in a microgravity-like environment it is possible. By using acoustic forces to trap bacteria at nodal planes of standing waves the cell-to-cell interaction is enhance promoting the formation of consolidated floating-clusters.

In this chapter we had as model microorganism two motile strains of *Escherichia coli*, CsgA + and Csg -. We evaluated how the overexpression (CsgA +) and repression (CsgA -) of the adhesive organelle *curli* modifies the formation of consolidated cluster as the ones found in Chapter 3 using non-motile cells.

We found that whilst the clustering process is somehow similar to the one depicted by all the previously analysed motile strains (RP437 and Jovanovic) the spreading process resembles the one shown by the non-motile strain, which are deflagellated ones. At first instance this resulted surprising but it is easily explained taking into account that the genetic pathway that regulates the expression or repression of curli also regulates flagella rotation. The bacteria are genetically modify resulting in a down regulation of their motility acting as non-motile cells.

In addition we found that morphology of the in-plane surface of the biofilm-like structure depends on the phenotype of bacteria, where the cells that are more adhesive exhibited wrinkles in their surface whereas the least adhesive cells exhibited a smooth surface a less compressed clusters.

Chapter 5

Discussion and perspectives

By general consensus biofilms are defined as mature aggregates of bacteria adherent to each other surrounded by a self-produced matrix attached to a surface [24].

The canonical model of biofilm formation establishes that the most important step towards its development is the adhesion of bacteria to surfaces and the dispersion of mature biofilm-chunks, that serve as precursors for new ones, into the bulk [29, 32, 33]. However our results show that it is possible to produce biofilm-like structures in a levitating environment where neither surfaces nor biofilm-chunks are needed as seeds for its formation.

Acoustic trapping at pressure nodes of standing waves provides confinement and the formation of clusters in levitation. In our acoustic trapping system the magnitude of the vertical forces was found to be in the order of piconewtons. Even when the transverse forces were not measured, it is well known that they are two orders of magnitude smaller than the primary radiation force [261]. Also, it was found that the measured vertical forces and the acoustic energy density are dependent of the applied voltage (U_{pp}), results that are in agreement with those found by Bruus [119] and Barnkob [117]. Unluckily, the approach that was used to obtain the energy density and the vertical forces only provided their local value. On the other hand, the macro characterisation provided evidence of the non homogeneous distribution of the energy that resulted in the emergence of several clusters at hot spots within a fixed region.

The acoustic forces arising within the cavity of our acoustic trap can confine bacteria regardless of their phenotype by restricting their degrees of freedom. At the nodal plane thin disk-shaped bacterial clusters are formed, which indicates that when the acoustic field is activated it triggers a sudden increase in the local density at energetic hot spots distributed along the nodal plane. Whilst the confinement efficiency does not depend on the phenotype of bacteria the number and size of cluster that are formed does.

Motile bacteria with a mean speed of 20 µm formed less clusters that their non-motile phenotype. For cells with down regulated motility and over-expression of an adhesive organelle the distribution of the clusters size is wider than that of cells with a suppression of the same organelle. The fact that motile cells form less number of clusters could be a consequence of the balance between the acoustic forces and the self-propulsion of bacteria. Probably, motile bacteria can counter-act easier the effects of the drag force created by acoustic forces than their non motile counter-parts [89, 179, 262].

Within the levitating clusters formed by motile cells a collective dynamic emerged, but on clusters of non-motile bacteria it did not. This observation is in accordance with the literature on collective effects that emerge when bacteria are under confinement [61, 63, 85**?** , 183]. The turbulent flow within the cluster was characterised measuring the mean kinetic energy and enstrophy as a function of the confinement strength that is given by the applied voltage. This analysis showed us that when the transversal trapping weakened the mean kinetic energy measure on the complete cluster did not changed significantly. Wheres when we analysed specific regions we could see how the kinetic energy values and the enstrophy decrease as a function of the applied voltage. The kinetic energy was higher at strong confinement since they are closer to each other and they can interact creating swarming fronts where they might organise [81, 85, 75].

We consider that in order to have a better characterisation of the cluster a three-dimensional scan should be performed; we started working on that and the preliminary results show that the cluster are not as thin as we believe (around 100 µm) hence a three-dimensional flow might be present. It is on our interest to analyse the collective motion in different z-planes to better characterised the dynamics within the levitating clusters.

In addition we also found that bacteria remained organised in clusters as long as they were trapped acoustically. When the acoustic input in the trapping systems was withdrawn and the acoustic forces ceased bacteria spread into the bulk suspension. This statement is only true for motile cells, since for non-motile cells and cells with down-regulated motility the clusters did not disaggregate. These results point out that non-motile and down regulated motile cells experienced a strong entanglement with a concomitant irreversible aggregation.

From the spreading results we can conclude that after only twenty minutes of acoustic confinement we are able to form free-floating biofilm-like structures in a levitating environment. The formation of biofilm-like structures is phenotype-dependent as they were formed only with non-motile cells and with cells with down-regulated motility. Nevertheless, in some preliminary studies we found that if the confinement period increases up to 3 hours it is possible to observe a nucleation process within clusters of motile cells as presented in Figure 5.1.

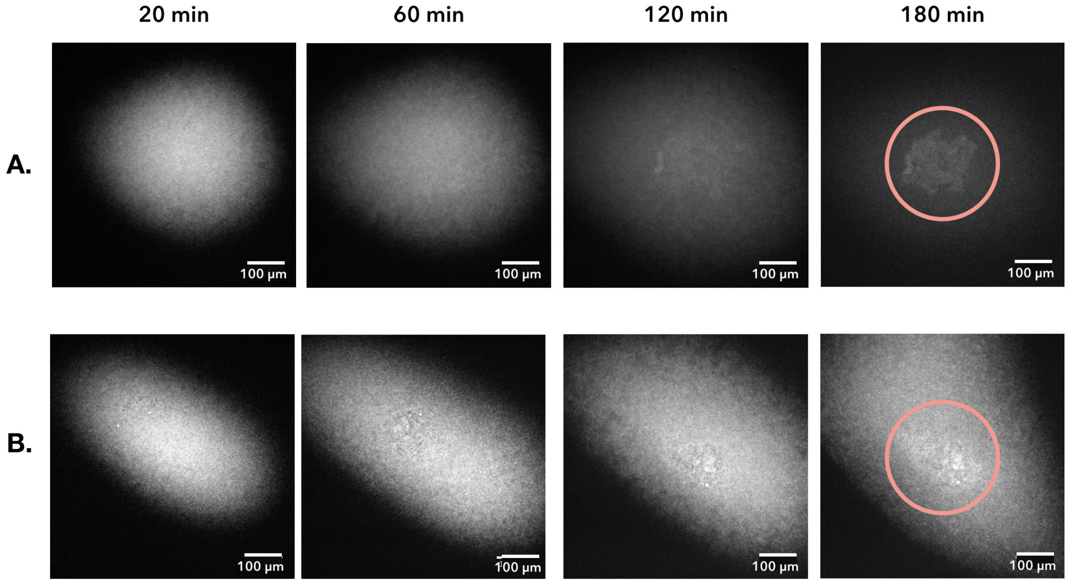

Fig. 5.1 **Examples of Jovanovic motile cluster under long confinement**

We did not perform the analysis of this phenomenon but it is a promising study for future research since it could be a way to study the transition from collective motion towards biofilm development.

Similarly, when bacteria are attracted to surfaces [32, 60], they also concentrate and lose motility [186], eventually forming free-floating biofilms [26].

Later the analysis of three other strains corroborated the formation of free-floating biofilms under acoustic confinement. It also proved that depending on the bacteria phenotype the biofilms presented specific characteristics.

We still need to perform the basic microbiological analysis such as the ones that we already standardised and describe in Appendix one and two which will permit in a straightforward manner to know if the biofilm-like structures are indeed cluster and also will hint us about the viability of bacteria after acoustic confinement. Also it could be interesting to perform biochemical analysis of the clustered bacteria, looking for genetic signals. Nevertheless, from a physical point of view, the first condition to create a biofilm has been attained: bacteria become crowded at a specific place and complex interactions modify their collective behaviour. In our case, this process was enhanced by an acoustic field where the surface interaction can be neglected and where there is no need of surface-attached biofilms or aggregates as seeds. This will give us crucial knowledge of biofilm development without surface interaction, possibly to produce models to evaluate antibiotics in a rapid and cheaper way.

Bibliography

[1] World Health Organization et al. *Antimicrobial resistance: global report on surveillance*. World Health Organization, 2014.

[2] World Health Organization et al. High levels of antibiotic resistance found worldwide, new data shows. *Saudi Medical Journal*, 39(4):430–431, 2018.

[3] Evelina Tacconelli, Elena Carrara, Alessia Savoldi, Stephan Harbarth, Marc Mendelson, Dominique L Monnet, Céline Pulcini, Gunnar Kahlmeter, Jan Kluytmans, Yehuda Carmeli, et al. Discovery, research, and development of new antibiotics: the who priority list of antibiotic-resistant bacteria and tuberculosis. *The Lancet Infectious Diseases*, 18(3):318–327, 2018.

[4] Timothy Kudinha, James R Johnson, Scott D Andrew, Fanrong Kong, Peter Anderson, and Gwendolyn L Gilbert. Escherichia coli sequence type 131 (st131) as a prominent cause of antibiotic resistance among urinary escherichia coli isolates from reproductive-age women. *Journal of clinical microbiology*, pages JCM–01315, 2013.

[5] Yolanda Sáenz, Laura Briñas, Elena Domínguez, Joaquim Ruiz, Myriam Zarazaga, Jordi Vila, and Carmen Torres. Mechanisms of resistance in multiple-antibiotic-resistant escherichia coli strains of human, animal, and food origins. *Antimicrobial agents and chemotherapy*, 48(10):3996–4001, 2004.

[6] Philip D Lister, Daniel J Wolter, and Nancy D Hanson. Antibacterial-resistant pseudomonas aeruginosa: clinical impact and complex regulation of chromosomally encoded resistance mechanisms. *Clinical microbiology reviews*, 22(4):582–610, 2009.

[7] Jean-Emmanuel Hugonnet, Lee W Tremblay, Helena I Boshoff, Clifton E Barry, and John S Blanchard. Meropenem-clavulanate is effective against extensively drug-resistant mycobacterium tuberculosis. *Science*, 323(5918):1215–1218, 2009.

[8] Federico Perez, Andrea M Hujer, Kristine M Hujer, Brooke K Decker, Philip N Rather, and Robert A Bonomo. Global challenge of multidrug-resistant acinetobacter baumannii. *Antimicrobial agents and chemotherapy*, 51(10):3471–3484, 2007.

[9] Lenie Dijkshoorn, Alexandr Nemec, and Harald Seifert. An increasing threat in hospitals: multidrug-resistant acinetobacter baumannii. *Nature reviews microbiology*, 5(12):939, 2007.

[10] Martin Exner, Sanjay Bhattacharya, Bärbel Christiansen, Jürgen Gebel, Peter Goroncy-Bermes, Philippe Hartemann, Peter Heeg, Carola Ilschner, Axel Kramer, Elaine Larson,

et al. Antibiotic resistance: What is so special about multidrug-resistant gram-negative bacteria? *GMS hygiene and infection control*, 12, 2017.

[11] Edo L Kussell, Roy Kishony, Nathalie Q Balaban, and Stanislas Leibler. Bacterial persistence: a model of survival in changing environments. *Genetics*, 2005.

[12] Thomas K Wood, Stephen J Knabel, and Brian W Kwan. Bacterial persister cell formation and dormancy. *Applied and environmental microbiology*, 79(23):7116–7121, 2013.

[13] Nadia R Cohen, Michael A Lobritz, and James J Collins. Microbial persistence and the road to drug resistance. *Cell host & microbe*, 13(6):632–642, 2013.

[14] Philip S Stewart and J William Costerton. Antibiotic resistance of bacteria in biofilms. *The lancet*, 358(9276):135–138, 2001.

[15] Andy Gardner, Stuart A West, and Ashleigh S Griffin. Is bacterial persistence a social trait? *PLoS One*, 2(8):e752, 2007.

[16] Pamela Lyon. The cognitive cell: bacterial behavior reconsidered. *Frontiers in microbiology*, 6:264, 2015.

[17] Eshel Ben-Jacob. Social behavior of bacteria: from physics to complex organization. *The European Physical Journal B*, 65(3):315–322, 2008.

[18] Niels Høiby. A short history of microbial biofilms and biofilm infections. *Apmis*, 125(4):272–275, 2017.

[19] Arthur T Henrici. Studies of freshwater bacteria: I. a direct microscopic technique. *Journal of bacteriology*, 25(3):277, 1933.

[20] H Heukelekian and A Heller. Relation between food concentration and surface for bacterial growth. *Journal of bacteriology*, 40(4):547, 1940.

[21] JW Costerton, JM Ingram, and KJ Cheng. Structure and function of the cell envelope of gram-negative bacteria. *Bacteriological reviews*, 38(1):87, 1974.

[22] Gary Dorken, Gail P Ferguson, Chris E French, and Wilson CK Poon. Aggregation by depletion attraction in cultures of bacteria producing exopolysaccharide. *Journal of The Royal Society Interface*, page rsif20120498, 2012.

[23] Shahrzad Yazdi and Arezoo M Ardekani. Bacterial aggregation and biofilm formation in a vortical flow. *Biomicrofluidics*, 6(4):044114, 2012.

[24] J William Costerton, Philip S Stewart, and E Peter Greenberg. Bacterial biofilms: a common cause of persistent infections. *Science*, 284(5418):1318–1322, 1999.

[25] Maxence Carrel, Verónica L Morales, Mario A Beltran, Nicolas Derlon, Rolf Kaufmann, Eberhard Morgenroth, and Markus Holzner. Biofilms in 3d porous media: Delineating the influence of the pore network geometry, flow and mass transfer on biofilm development. *Water research*, 134:280–291, 2018.

[26] Knut Drescher, Yi Shen, Bonnie L Bassler, and Howard A Stone. Biofilm streamers cause catastrophic disruption of flow with consequences for environmental and medical systems. *Proceedings of the National Academy of Sciences*, 110(11):4345–4350, 2013.

[27] Steven L Percival, David Williams, Tracey Cooper, and Jacqueline Randle. *Biofilms in infection prevention and control: a healthcare handbook*. Academic Press, 2014.

[28] Cristian Picioreanu, Mark CM Van Loosdrecht, and Joseph J Heijnen. Effect of diffusive and convective substrate transport on biofilm structure formation: A two-dimensional modeling study. *Biotechnology and bioengineering*, 69(5):504–515, 2000.

[29] Jacinta C Conrad and Ryan Poling-Skutvik. Confined flow: Consequences and implications for bacteria and biofilms. *Annual review of chemical and biomolecular engineering*, (0), 2018.

[30] Dewi P Bakker, Henk J Busscher, and Henny C van der Mei. Bacterial deposition in a parallel plate and a stagnation point flow chamber: microbial adhesion mechanisms depend on the mass transport conditions. *Microbiology*, 148(2):597–603, 2002.

[31] Jan JTM Swartjes, Deepak H Veeregowda, Henny C van der Mei, Henk J Busscher, and Prashant K Sharma. Normally oriented adhesion versus friction forces in bacterial adhesion to polymer-brush functionalized surfaces under fluid flow. *Advanced Functional Materials*, 24(28):4435–4441, 2014.

[32] Christophe Beloin, Agnès Roux, and J-M Ghigo. Escherichia coli biofilms. In *Bacterial biofilms*, pages 249–289. Springer, 2008.

[33] Alexandre Persat, Carey D Nadell, Minyoung Kevin Kim, Francois Ingremeau, Albert Siryaporn, Knut Drescher, Ned S Wingreen, Bonnie L Bassler, Zemer Gitai, and Howard A Stone. The mechanical world of bacteria. *Cell*, 161(5):988–997, 2015.

[34] GE c-authors Fox, E Stackebrandt, RB Hespell, J Gibson, J Maniloff, TA Dyer, RS Wolfe, WE Balch, RS Tanner, LJ Magrum, et al. The phylogeny of prokaryotes. *Science*, 209(4455):457–463, 1980.

[35] Matthew F Copeland and Douglas B Weibel. Bacterial swarming: a model system for studying dynamic self-assembly. *Soft matter*, 5(6):1174–1187, 2009.

[36] Jean-Marie Swiecicki, Olesksii Sliusarenko, and Douglas B Weibel. From swimming to swarming: Escherichia coli cell motility in two-dimensions. *Integrative Biology*, 5(12):1490–1494, 2013.

[37] Natalie Verstraeten, Kristien Braeken, Bachaspatimayum Debkumari, Maarten Fauvart, Jan Fransaer, Jan Vermant, and Jan Michiels. Living on a surface: swarming and biofilm formation. *Trends in microbiology*, 16(10):496–506, 2008.

[38] Joana Azeredo, Nuno F Azevedo, Romain Briandet, Nuno Cerca, Tom Coenye, Ana Rita Costa, Mickaël Desvaux, Giovanni Di Bonaventura, Michel Hébraud, Zoran Jaglic, et al. Critical review on biofilm methods. *Critical reviews in microbiology*, 43(3):313–351, 2017.

[39] Cécile Berne, Adrien Ducret, Gail G Hardy, and Yves V Brun. Adhesins involved in attachment to abiotic surfaces by gram-negative bacteria. *Microbiology spectrum*, 3(4), 2015.

[40] Philippe Thomen, Jérôme Robert, Amaury Monmeyran, Anne-Florence Bitbol, Carine Douarche, and Nelly Henry. Bacterial biofilm under flow: First a physical struggle to stay, then a matter of breathing. *PloS one*, 12(4):e0175197, 2017.

[41] Elke Peeters, Hans J Nelis, and Tom Coenye. Comparison of multiple methods for quantification of microbial biofilms grown in microtiter plates. *Journal of microbiological methods*, 72(2):157–165, 2008.

[42] Betsey Pitts, Martin A Hamilton, Nicholas Zelver, and Philip S Stewart. A microtiter-plate screening method for biofilm disinfection and removal. *Journal of microbiological methods*, 54(2):269–276, 2003.

[43] Srdjan Stepanović, Dragana Vuković, Veronika Hola, GIOVANNI DI BONAVENTURA, Slobodanka Djukić, Ivana Ćirković, and Filip Ruzicka. Quantification of biofilm in microtiter plates: overview of testing conditions and practical recommendations for assessment of biofilm production by staphylococci. *Apmis*, 115(8):891–899, 2007.

[44] H Ceri, ME Olson, C Stremick, RR Read, D Morck, and A Buret. The calgary biofilm device: new technology for rapid determination of antibiotic susceptibilities of bacterial biofilms. *Journal of clinical microbiology*, 37(6):1771–1776, 1999.

[45] Joe J Harrison, Howard Ceri, Jerome Yerly, Carol A Stremick, Yaoping Hu, Robert Martinuzzi, and Raymond J Turner. The use of microscopy and three-dimensional visualization to evaluate the structure of microbial biofilms cultivated in the calgary biofilm device. *Biological procedures online*, 8(1):194, 2006.

[46] Merle E Olson, Howard Ceri, Douglas W Morck, Andre G Buret, and Ronald R Read. Biofilm bacteria: formation and comparative susceptibility to antibiotics. *Canadian Journal of Veterinary Research*, 66(2):86, 2002.

[47] S Badel, C Laroche, C Gardarin, T Bernardi, and P Michaud. New method showing the influence of matrix components in leuconostoc mesenteroides biofilm formation. *Applied biochemistry and biotechnology*, 151(2-3):364–370, 2008.

[48] Patrick Chavant, Brigitte Gaillard-Martinie, Régine Talon, Michel Hébraud, and Thierry Bernardi. A new device for rapid evaluation of biofilm formation potential by bacteria. *Journal of microbiological methods*, 68(3):605–612, 2007.

[49] Elodie Olivares, Stéphanie Badel-Berchoux, Christian Provot, Benoît Jaulhac, Gilles Prévost, Thierry Bernardi, and François Jehl. The biofilm ring test®: a rapid method for the routine analysis of p. aeruginosa biofilm formation kinetics. *Journal of clinical microbiology*, pages JCM–02938, 2015.

[50] Moira D Johnston and Martin V Jones. Disinfection tests with intact biofilms: combined use of the modified robbins device with impedance detection. *Journal of microbiological methods*, 21(1):15–26, 1995.

[51] Arsalan Kharazmi, Birgit Giwercman, and Niels Høiby. [16] robbins device in biofilm research. In *Methods in enzymology*, volume 310, pages 207–215. Elsevier, 1999.

[52] Darla M Goeres, Martin A Hamilton, Nicholas A Beck, Kelli Buckingham-Meyer, Jackie D Hilyard, Linda R Loetterle, Lindsey A Lorenz, Diane K Walker, and Philip S Stewart. A method for growing a biofilm under low shear at the air–liquid interface using the drip flow biofilm reactor. *Nature protocols*, 4(5):783, 2009.

[53] Kelly Schwartz, Rachel Stephenson, Margarita Hernandez, Nicolays Jambang, and Blaise R Boles. The use of drip flow and rotating disk reactors for staphylococcus aureus biofilm analysis. *Journal of visualized experiments: JoVE*, (46), 2010.

[54] Rajbir Singh, Debarati Paul, and Rakesh K Jain. Biofilms: implications in bioremediation. *Trends in microbiology*, 14(9):389–397, 2006.

[55] Altan Ozkan, Kerry Kinney, Lynn Katz, and Halil Berberoglu. Reduction of water and energy requirement of algae cultivation using an algae biofilm photobioreactor. *Bioresource technology*, 114:542–548, 2012.

[56] Claus Sternberg, Bjarke B Christensen, Tove Johansen, Alex Toftgaard Nielsen, Jens Bo Andersen, Michael Givskov, and Søren Molin. Distribution of bacterial growth activity in flow-chamber biofilms. *Applied and Environmental Microbiology*, 65(9):4108–4117, 1999.

[57] Lukas Richter, Christoph Stepper, Andy Mak, Alessa Reinthaler, Rudolf Heer, Michael Kast, Hubert Brückl, and Peter Ertl. Development of a microfluidic biochip for online monitoring of fungal biofilm dynamics. *Lab on a Chip*, 7(12):1723–1731, 2007.

[58] Rodney M Donlan. Biofilms: microbial life on surfaces. *Emerging infectious diseases*, 8(9):881, 2002.

[59] Ya-Wen Chang, Alexandros A Fragkopoulos, Samantha M Marquez, Harold D Kim, Thomas E Angelini, and Alberto Fernández-Nieves. Biofilm formation in geometries with different surface curvature and oxygen availability. *New Journal of Physics*, 17(3):033017, 2015.

[60] Eric Lauga and Thomas R Powers. The hydrodynamics of swimming microorganisms. *Reports on Progress in Physics*, 72(9):096601, 2009.

[61] Eric Lauga. Bacterial hydrodynamics. *Annual Review of Fluid Mechanics*, 48:105–130, 2016.

[62] Eric Clement, Anke Lindner, Carine Douarche, and Harold Auradou. Bacterial suspensions under flow. *The European Physical Journal Special Topics*, 225(11-12):2389–2406, 2016.

[63] Tamás Vicsek and Anna Zafeiris. Collective motion. *Physics Reports*, 517(3-4):71–140, 2012.

[64] David Saintillan. Kinetic models for biologically active suspensions. In *Natural Locomotion in Fluids and on Surfaces*, pages 53–71. Springer, 2012.

[65] Edward M Purcell. Life at low reynolds number. *American journal of physics*, 45(1):3–11, 1977.

[66] Howard C Berg and Robert A Anderson. Bacteria swim by rotating their flagellar filaments. *Nature*, 245(5425):380, 1973.

[67] J Tailleur and ME Cates. Statistical mechanics of interacting run-and-tumble bacteria. *Physical review letters*, 100(21):218103, 2008.

[68] Howard C Berg. *Random walks in biology*. Princeton University Press, 1993.

[69] Linda Turner, William S Ryu, and Howard C Berg. Real-time imaging of fluorescent flagellar filaments. *Journal of bacteriology*, 182(10):2793–2801, 2000.

[70] Evelyn F Keller and Lee A Segel. Traveling bands of chemotactic bacteria: a theoretical analysis. *Journal of theoretical biology*, 30(2):235–248, 1971.

[71] Colin J Ingham and Eshel Ben Jacob. Swarming and complex pattern formation in paenibacillus vortex studied by imaging and tracking cells. *BMC microbiology*, 8(1):36, 2008.

[72] J Lega and T Passot. Hydrodynamics of bacterial colonies. *Nonlinearity*, 20(1):C1, 2006.

[73] Ruth A Lambert, Francesco Picano, Wim-Paul Breugem, and Luca Brandt. Active suspensions in thin films: nutrient uptake and swimmer motion. *Journal of Fluid Mechanics*, 733:528–557, 2013.

[74] Jasmine A Nirody, Yi-Ren Sun, and Chien-Jung Lo. The biophysicist's guide to the bacterial flagellar motor. *Advances in Physics: X*, 2(2):324–343, 2017.

[75] Hugo Wioland, Enkeleida Lushi, and Raymond E Goldstein. Directed collective motion of bacteria under channel confinement. *New Journal of Physics*, 18(7):075002, 2016.

[76] Jingjing Feng and Yan He. Collective motion of bacteria and their dynamic assembly behavior. *Science China Materials*, 60(11):1079–1092, 2017.

[77] Fernando Peruani, Jörn Starruß, Vladimir Jakovljevic, Lotte Søgaard-Andersen, Andreas Deutsch, and Markus Bär. Collective motion and nonequilibrium cluster formation in colonies of gliding bacteria. *Physical review letters*, 108(9):098102, 2012.

[78] He-Peng Zhang, Avraham Be'er, E-L Florin, and Harry L Swinney. Collective motion and density fluctuations in bacterial colonies. *Proceedings of the National Academy of Sciences*, 107(31):13626–13630, 2010.

[79] Andrey Sokolov, Igor S Aranson, John O Kessler, and Raymond E Goldstein. Concentration dependence of the collective dynamics of swimming bacteria. *Physical review letters*, 98(15):158102, 2007.

[80] Enkeleida Lushi, Hugo Wioland, and Raymond E Goldstein. Fluid flows created by swimming bacteria drive self-organization in confined suspensions. *Proceedings of the National Academy of Sciences*, page 201405698, 2014.

[81] Knut Drescher, Jörn Dunkel, Luis H Cisneros, Sujoy Ganguly, and Raymond E Goldstein. Fluid dynamics and noise in bacterial cell–cell and cell–surface scattering. *Proceedings of the National Academy of Sciences*, 108(27):10940–10945, 2011.

[82] Henricus H Wensink, Jörn Dunkel, Sebastian Heidenreich, Knut Drescher, Raymond E Goldstein, Hartmut Löwen, and Julia M Yeomans. Meso-scale turbulence in living fluids. *Proceedings of the National Academy of Sciences*, 2012.

[83] Igor S Aranson, Andrey Sokolov, John O Kessler, and Raymond E Goldstein. Model for dynamical coherence in thin films of self-propelled microorganisms. *Physical Review E*, 75(4):040901, 2007.

[84] Andrey Sokolov, Raymond E Goldstein, Felix I Feldchtein, and Igor S Aranson. Enhanced mixing and spatial instability in concentrated bacterial suspensions. *Physical Review E*, 80(3):031903, 2009.

[85] Hugo Wioland, Francis G Woodhouse, Jörn Dunkel, John O Kessler, and Raymond E Goldstein. Confinement stabilizes a bacterial suspension into a spiral vortex. *Physical review letters*, 110(26):268102, 2013.

[86] Luis H Cisneros, Ricardo Cortez, Christopher Dombrowski, Raymond E Goldstein, and John O Kessler. Fluid dynamics of self-propelled microorganisms, from individuals to concentrated populations. In *Animal Locomotion*, pages 99–115. Springer, 2010.

[87] Benoit Vincenti, Carine Douarche, and Eric Clement. Actuated rheology of magnetic micro-swimmers suspensions: Emergence of motor and brake states. *Physical Review Fluids*, 3(3):033302, 2018.

[88] Richard P Blakemore. Magnetotactic bacteria. *Annual Reviews in Microbiology*, 36(1):217–238, 1982.

[89] ME Cates and J Tailleur. When are active brownian particles and run-and-tumble particles equivalent? consequences for motility-induced phase separation. *EPL (Europhysics Letters)*, 101(2):20010, 2013.

[90] Sadayuki Ueha, Yoshiki Hashimoto, and Yoshikazu Koike. Non-contact transportation using near-field acoustic levitation. *Ultrasonics*, 38(1-8):26–32, 2000.

[91] Mary Ann H Weiser and Robert E Apfel. Extension of acoustic levitation to include the study of micron-size particles in a more compressible host liquid. *The Journal of the Acoustical Society of America*, 71(5):1261–1268, 1982.

[92] James Friend and Leslie Y Yeo. Microscale acoustofluidics: Microfluidics driven via acoustics and ultrasonics. *Reviews of Modern Physics*, 83(2):647, 2011.

[93] Henrik Bruus. Theoretical aspects of microscale acoustofluidics. *arXiv preprint arXiv:1802.05597*, 2018.

[94] Henrik Bruus, Jurg Dual, Jeremy Hawkes, Martyn Hill, Thomas Laurell, Johan Nilsson, Stefan Radel, Satwindar Sadhal, and Martin Wiklund. Forthcoming lab on a chip tutorial series on acoustofluidics: Acoustofluidics—exploiting ultrasonic standing wave forces and acoustic streaming in microfluidic systems for cell and particle manipulation. *Lab on a Chip*, 11(21):3579–3580, 2011.

[95] Björn Hammarström, Mikael Evander, Herve Barbeau, Mattias Bruzelius, Jörgen Larsson, Thomas Laurell, and Johan Nilsson. Non-contact acoustic cell trapping in disposable glass capillaries. *Lab on a Chip*, 10(17):2251–2257, 2010.

[96] Sho C Takatori, Raf De Dier, Jan Vermant, and John F Brady. Acoustic trapping of active matter. *Nature communications*, 7:10694, 2016.

[97] Johan Nilsson, Mikael Evander, Björn Hammarström, and Thomas Laurell. Review of cell and particle trapping in microfluidic systems. *Analytica chimica acta*, 649(2):141–157, 2009.

[98] D Bazou, W Terence Coakley, AJ Hayes, and Simon K Jackson. Long-term viability and proliferation of alginate-encapsulated 3-d hepg2 aggregates formed in an ultrasound trap. *Toxicology in Vitro*, 22(5):1321–1331, 2008.

[99] Björn Hammarström, Thomas Laurell, and Johan Nilsson. Seed particle-enabled acoustic trapping of bacteria and nanoparticles in continuous flow systems. *Lab on a Chip*, 12(21):4296–4304, 2012.

[100] Maria Sundvik, Heikki J Nieminen, Ari Salmi, Pertti Panula, and Edward Hæggström. Effects of acoustic levitation on the development of zebrafish, danio rerio, embryos. *Scientific reports*, 5:13596, 2015.

[101] August Kundt. Über eine neue art akustischer staubfiguren und über die anwendung derselben zur bestimmung der schallgeschwindigkeit in festen körpern und gasen. *Annalen der Physik*, 203(4):497–523, 1866.

[102] Mary Dyson, B Woodward, and JB Pond. Flow of red blood cells stopped by ultrasound. *Nature*, 232(5312):572, 1971.

[103] N Vashon Baker. Segregation and sedimentation of red blood cells in ultrasonic standing waves. *Nature*, 239(5372):398, 1972.

[104] EG Lierke. Acoustic levitation–a comprehensive survey of principles and applications. *Acta Acustica united with Acustica*, 82(2):220–237, 1996.

[105] Zhangming Mao, Yuliang Xie, Feng Guo, Liqiang Ren, Po-Hsun Huang, Yuchao Chen, Joseph Rufo, Francesco Costanzo, and Tony Jun Huang. Experimental and numerical studies on standing surface acoustic wave microfluidics. *Lab on a chip*, 16(3):515–524, 2016.

[106] JK Luo, Yong Qing Fu, and WI Milne. Acoustic wave based microfluidics and lab-on-a-chip. In *Modeling and Measurement Methods for Acoustic Waves and for Acoustic Microdevices*. InTech, 2013.

[107] Chunlong Fei, Jianguo Ma, Chi Tat Chiu, Jay A. Williams, Wayne Fong, Zeyu Chen, BenPeng Zhu, Rui Xiong, Jing Shi, Tzung K. Hsiai, K. Kirk Shung, and Qifa Zhou. Design of matching layers for high-frequency ultrasonic transducers. *Applied Physics Letters*, 107(12):123505, 2015.

[108] Louis Vessot King et al. On the acoustic radiation pressure on spheres. *Proc. R. Soc. Lond. A*, 147(861):212–240, 1934.

[109] K Yosioka and Y Kawasima. Acoustic radiation pressure on a compressible sphere. *Acta Acustica united with Acustica*, 5(3):167–173, 1955.

[110] L. P. Gor'kov. On the Forces Acting on a Small Particle in an Acoustical Field in an Ideal Fluid. *Soviet Physics Doklady*, 6:773, March 1962.

[111] WT Coakley, JJ Hawkes, MA Sobanski, CM Cousins, and J Spengler. Analytical scale ultrasonic standing wave manipulation of cells and microparticles. *Ultrasonics*, 38(1-8):638–641, 2000.

[112] W Terence Coakley, David W Bardsley, Martin A Grundy, Freidoun Zamani, and David J Clarke. Cell manipulation in ultrasonic standing wave fields. *Journal of Chemical Technology & Biotechnology*, 44(1):43–62, 1989.

[113] Jeremy J Hawkes, Robert W Barber, David R Emerson, and W Terence Coakley. Continuous cell washing and mixing driven by an ultrasound standing wave within a microfluidic channel. *Lab on a Chip*, 4(5):446–452, 2004.

[114] Jeremy J Hawkes and W Terence Coakley. Force field particle filter, combining ultrasound standing waves and laminar flow. *Sensors and Actuators B: Chemical*, 75(3):213–222, 2001.

[115] A. Lenshof, M. Evander, T. Laurell, and J. Nilsson. Acoustofluidics 5: Building microfluidic acoustic resonators. *Lab Chip*, 12:684–695, 2012.

[116] J. Nilsson, M. Evander, B. Hammarström, and T. Laurell. Review of cell and particle trapping in microfluidic systems. *Analytica Chimica Acta*, 649(2):141 – 157, 2009.

[117] Rune Barnkob, Per Augustsson, Thomas Laurell, and Henrik Bruus. Measuring the local pressure amplitude in microchannel acoustophoresis. *Lab on a chip*, 10 5:563–70, 2010.

[118] Henrik Bruus. Acoustofluidics 2: Perturbation theory and ultrasound resonance modes. *Lab Chip*, 12:20–28, 2012.

[119] S. M. Hagsater, T. Glasdam Jensen, H. Bruus, and J. P. Kutter. Acoustic resonances in microfluidic chips: full-image micro-piv experiments and numerical simulations. *Lab Chip*, 7:1336–1344, 2007.

[120] Henrik Bruus. Acoustofluidics 7: The acoustic radiation force on small particles. *Lab Chip*, 12:1014–1021, 2012.

[121] Sir James Lighthill. Acoustic streaming. *Journal of Sound and Vibration*, 61(3):391 – 418, 1978.

[122] Philipp Hahn, Ivo Leibacher, Thierry Baasch, and Jurg Dual. Numerical simulation of acoustofluidic manipulation by radiation forces and acoustic streaming for complex particles. *Lab on a Chip*, 15(22):4302–4313, 2015.

[123] Junjun Lei, Peter Glynne-Jones, and Martyn Hill. Acoustic streaming in the transducer plane in ultrasonic particle manipulation devices. *Lab on a Chip*, 13(11):2133–2143, 2013.

[124] Philipp Hahn, Olivier Schwab, and Jurg Dual. Modeling and optimization of acoustofluidic micro-devices. *Lab on a Chip*, 14(20):3937–3948, 2014.

[125] Satya VVN Kothapalli, Michael B Altman, Ari Partanen, Leighton Wan, H Michael Gach, William Straube, Dennis E Hallahan, and Hong Chen. Acoustic field characterization of a clinical magnetic resonance-guided high-intensity focused ultrasound system inside the magnet bore. *Medical physics*, 44(9):4890–4899, 2017.

[126] S Melker Hagsäter, T Glasdam Jensen, Henrik Bruus, and Jörg P Kutter. Acoustic resonances in microfluidic chips: full-image micro-piv experiments and numerical simulations. *Lab on a Chip*, 7(10):1336–1344, 2007.

[127] Henrik Bruus. Acoustofluidics 7: The acoustic radiation force on small particles. *Lab on a Chip*, 12(6):1014–1021, 2012.

[128] Rune Barnkob, Per Augustsson, Thomas Laurell, and Henrik Bruus. Measuring the local pressure amplitude in microchannel acoustophoresis. *Lab on a Chip*, 10(5):563–570, 2010.

[129] Alexander Doinikov. Acoustic radiation forces: Classical theory and recent advances. 1:39–67, 01 2003.

[130] Mikkel Settnes and Henrik Bruus. Forces acting on a small particle in an acoustical field in a viscous fluid. *Phys. Rev. E*, 85:016327, Jan 2012.

[131] MAH Weiser, RE Apfel, and EA Neppiras. Interparticle forces on red cells in a standing wave field. *Acta Acustica united with Acustica*, 56(2):114–119, 1984.

[132] Alexander A Doinikov. Acoustic radiation forces: Classical theory and recent advances. *Recent Res Devel Acoustics*, 1:39–67, 2003.

[133] Anna Garcia-Sabaté, Angélica Castro, Mauricio Hoyos, and Ricard González-Cinca. Experimental study on inter-particle acoustic forces. *The Journal of the Acoustical Society of America*, 135(3):1056–1063, 2014.

[134] Lord Rayleigh. On the circulation of air observed in kundt's tubes, and on some allied acoustical problem. *Phil. Trans. Roy. Soc*, 175:1–21, 1884.

[135] Michael Faraday et al. On a peculiar class of acoustical figures; and on certain forms assumed by groups of particles upon vibrating elastic surfaces. In *Abstracts of the Papers Printed in the Philosophical Transactions of the Royal Society of London*, volume 3, pages 49–51. The Royal Society, 1837.

[136] Said Boluriaan and Philip J Morris. Acoustic streaming: from rayleigh to today. *International Journal of aeroacoustics*, 2(3):255–292, 2003.

[137] Ernst Florens Friedrich Chladni. *Entdeckungen über die Theorie des Klanges*. Zentralantiquariat der DDR, 1787.

[138] Martin Wiklund, Roy Green, and Mathias Ohlin. Acoustofluidics 14: Applications of acoustic streaming in microfluidic devices. *Lab on a Chip*, 12(14):2438–2451, 2012.

[139] Wesley L Nyborg. Acoustic streaming near a boundary. *The Journal of the Acoustical Society of America*, 30(4):329–339, 1958.

[140] Hermann Schlichting. Berechnung ebener periodischer grenzschichtstromungen. *Phys. z.*, 33:327–335, 1932.

[141] Xudong Zhang, Eiji Ashida, Susumu Shono, and Fukuhisa Matsuda. Effect of shielding conditions of local dry cavity on weld quality in underwater nd: Yag laser welding. *Journal of Materials Processing Technology*, 174(1-3):34–41, 2006.

[142] Hao-Li Liu and Chao-Ming Hsieh. Single-transducer dual-frequency ultrasound generation to enhance acoustic cavitation. *Ultrasonics sonochemistry*, 16(3):431–438, 2009.

[143] Mathias Ohlin. *Ultrasonic Fluid and Cell Manipulation*. PhD thesis, KTH Royal Institute of Technology, 2015.

[144] Samuel A Elder. Cavitation microstreaming. *The Journal of the Acoustical Society of America*, 31(1):54–64, 1959.

[145] Maulik V Patel, Imaly A Nanayakkara, Melinda G Simon, and Abraham P Lee. Cavity-induced microstreaming for simultaneous on-chip pumping and size-based separation of cells and particles. *Lab on a Chip*, 14(19):3860–3872, 2014.

[146] Yu Wang, Bing Hu, Xuehong Diao, and Jizhen Zhang. Antitumor effect of microbubbles enhanced by low frequency ultrasound cavitation on prostate carcinoma xenografts in nude mice. *Experimental and therapeutic medicine*, 3(2):187–191, 2012.

[147] Ying-Zheng Zhao, Cui-Tao Lu, Xiao-Kun Li, and Jun Cai. Ultrasound-mediated strategies in opening brain barriers for drug brain delivery. *Expert opinion on drug delivery*, 10(7):987–1001, 2013.

[148] JF Spengler, WT Coakley, and KT Christensen. Microstreaming effects on particle concentration in an ultrasonic standing wave. *AIChE journal*, 49(11):2773–2782, 2003.

[149] Larisa A Kuznetsova and W Terence Coakley. Microparticle concentration in short path length ultrasonic resonators: Roles of radiation pressure and acoustic streaming. *The Journal of the Acoustical Society of America*, 116(4):1956–1966, 2004.

[150] Johannes F Spengler and W Terence Coakley. Ultrasonic trap to monitor morphology and stability of developing microparticle aggregates. *Langmuir*, 19(9):3635–3642, 2003.

[151] Kenneth D Frampton, Shawn E Martin, and Keith Minor. The scaling of acoustic streaming for application in micro-fluidic devices. *Applied Acoustics*, 64(7):681–692, 2003.

[152] Per Augustsson, Rune Barnkob, Steven T Wereley, Henrik Bruus, and Thomas Laurell. Automated and temperature-controlled micro-piv measurements enabling long-term-stable microchannel acoustophoresis characterization. *Lab on a Chip*, 11(24):4152–4164, 2011.

[153] Martin Wiklund, Roy Green, and Mathias Ohlin. Acoustofluidics 14: Applications of acoustic streaming in microfluidic devices. *Lab Chip*, 12:2438–2451, 2012.

[154] Kenji Yasuda, Shin-ichiro Umemura, Kenichi Kawabata, Kazuo Takeda, Kenko Uchida, Yoshinori Harada, Masao Kamahori, and Kazuaki Sasaki. Particle handling apparatus for handling particles in fluid by acoustic radiation pressure, April 17 2001. US Patent 6,216,538.

[155] J Hawkes Jeremy, Gröschl Martin, Benes Ewald, Nowotny Helmut, and Coakley W Terence. Positioning particles within liquids using ultrasound force fields.

[156] Bellebon Ludovic. Manipulation acoustique de cellules souches mesenchymateuses, 2017.

[157] George Biddell Airy. On the diffraction of an object-glass with circular aperture. *Transactions of the Cambridge Philosophical Society*, 5:283, 1835.

[158] Olivier Dron. *Micro-manipulation acoustique de particules: application aux mesures par micro-PIV*. PhD thesis, Paris 7, 2011.

[159] Steven M Woodside, James M Piret, Martin Gröschl, Ewald Benes, and Bruce D Bowen. Acoustic force distribution in resonators for ultrasonic particle separation. *AIChE journal*, 44(9):1976–1984, 1998.

[160] Martyn Hill. The selection of layer thicknesses to control acoustic radiation force profiles in layered resonators. *The Journal of the Acoustical Society of America*, 114(5):2654–2661, 2003.

[161] Zachary D Blount. The natural history of model organisms: The unexhausted potential of e. coli. *Elife*, 4:e05826, 2015.

[162] Carl Zimmer. *Microcosm: E-coli and the New Science of Life*. Random House, 2012.

[163] Jörg Hacker and Gabriele Blum-Oehler. In appreciation of theodor escherich, 2007.

[164] Nanne Nanninga. Morphogenesis of escherichia coli. *Microbiology and Molecular Biology Reviews*, 62(1):110–129, 1998.

[165] Willliam D Donachie. The cell cycle of escherichia coli. *Annual Reviews in Microbiology*, 47(1):199–230, 1993.

[166] Johanna Roostalu, Arvi Jõers, Hannes Luidalepp, Niilo Kaldalu, and Tanel Tenson. Cell division in escherichia coli cultures monitored at single cell resolution. *BMC microbiology*, 8(1):68, 2008.

[167] Jue D Wang and Petra A Levin. Metabolism, cell growth and the bacterial cell cycle. *Nature Reviews Microbiology*, 7(11):822, 2009.

[168] Howard C Berg. The rotary motor of bacterial flagella. *Annual review of biochemistry*, 72, 2003.

[169] Emily E Riley, Debasish Das, and Eric Lauga. Swimming of peritrichous bacteria is enabled by an elastohydrodynamic instability. *arXiv preprint arXiv:1806.01902*, 2018.

[170] Thierry Mora, Howard Yu, Yoshiyuki Sowa, and Ned S Wingreen. Steps in the bacterial flagellar motor. *PLoS computational biology*, 5(10):e1000540, 2009.

[171] Suddhashil Chattopadhyay, Radu Moldovan, Chuck Yeung, and XL Wu. Swimming efficiency of bacterium escherichiacoli. *Proceedings of the National Academy of Sciences*, 103(37):13712–13717, 2006.

[172] Gerald L Hazelbauer, Howard C Berg, and Phillp Matsumura. Bacterial motility and signal transduction. *Cell*, 73(1):15–22, 1993.

[173] Robert M Macnab. How bacteria assemble flagella. *Annual Reviews in Microbiology*, 57(1):77–100, 2003.

[174] Maryam Khatami, Katrin Wolff, Oliver Pohl, Mohammad Reza Ejtehadi, and Holger Stark. Active brownian particles and run-and-tumble particles separate inside a maze. *Scientific Reports*, 6:37670, 2016.

[175] Howard C Berg, Douglas A Brown, et al. Chemotaxis in escherichia coli analysed by three-dimensional tracking. *Nature*, 239(5374):500–504, 1972.

[176] Noreen R Francis, Gina E Sosinsky, Dennis Thomas, and David J DeRosier. Isolation, characterization and structure of bacterial flagellar motors containing the switch complex. *Journal of molecular biology*, 235(4):1261–1270, 1994.

[177] Sara Moens and Jos Vanderleyden. Functions of bacterial flagella. *Critical reviews in microbiology*, 22(2):67–100, 1996.

[178] T Tino. Genetics of structure and function of bacterial flagella. *Annual review of genetics*, 11(1):161–182, 1977.

[179] Michael E Cates. Diffusive transport without detailed balance in motile bacteria: does microbiology need statistical physics? *Reports on Progress in Physics*, 75(4):042601, 2012.

[180] Alasdair G Thompson, Julien Tailleur, Michael E Cates, and Richard A Blythe. Lattice models of nonequilibrium bacterial dynamics. *Journal of Statistical Mechanics: Theory and Experiment*, 2011(02):P02029, 2011.

[181] Adam Patch, David Yllanes, and M Cristina Marchetti. Kinetics of motility-induced phase separation and swim pressure. *Physical Review E*, 95(1):012601, 2017.

[182] Luanne Hall-Stoodley, J William Costerton, and Paul Stoodley. Bacterial biofilms: from the natural environment to infectious diseases. *Nature reviews microbiology*, 2(2):95, 2004.

[183] Knut Drescher, Raymond E Goldstein, Nicolas Michel, Marco Polin, and Idan Tuval. Direct measurement of the flow field around swimming microorganisms. *Physical Review Letters*, 105(16):168101, 2010.

[184] GLENN L Cooper, AL Schiller, and CYRUS C Hopkins. Possible role of capillary action in pathogenesis of experimental catheter-associated dermal tunnel infections. *Journal of clinical microbiology*, 26(1):8–12, 1988.

[185] GDJF Harkes, J Dankert, and Jan Feijen. Bacterial migration along solid surfaces. *Applied and environmental microbiology*, 58(5):1500–1505, 1992.

[186] George O'Toole, Heidi B Kaplan, and Roberto Kolter. Biofilm formation as microbial development. *Annual Reviews in Microbiology*, 54(1):49–79, 2000.

[187] Jana Schwarz-Linek, Jochen Arlt, Alys Jepson, Angela Dawson, Teun Vissers, Dario Miroli, Teuta Pilizota, Vincent A Martinez, and Wilson CK Poon. Escherichia coli as a model active colloid: A practical introduction. *Colloids and Surfaces B: Biointerfaces*, 137:2–16, 2016.

[188] Peter Model, Goran Jovanovic, and Jonathan Dworkin. The escherichia coli phage-shock-protein (psp) operon. *Molecular microbiology*, 24(2):255–261, 1997.

[189] Nuris Figueroa-Morales, Thierry Darnige, Carine Douarche, Vincent Martinez, Rodrigo Soto, Anke Lindner, and Eric Clément. 3d spatial exploration by e. coli echoes motor temporal variability. *arXiv preprint arXiv:1803.01295*, 2018.

[190] Daniel J Ferullo, Deani L Cooper, Hayley R Moore, and Susan T Lovett. Cell cycle synchronization of escherichia coli using the stringent response, with fluorescence labeling assays for dna content and replication. *Methods*, 48(1):8–13, 2009.

[191] Kotakonda Arunasri, Mohammed Adil, Pathan Akbar Ali Khan, and Sisinthy Shivaji. Global gene expression analysis of long-term stationary phase effects in e. coli k12 mg1655. *PloS one*, 9(5):e96701, 2014.

[192] Scott Sutton. Measurement of microbial cells by optical density. *Journal of Validation technology*, 17(1):46–49, 2011.

[193] Salomé Gutiérrez-Ramos, Mauricio Hoyos, and JC Ruiz-Suárez. Induced clustering of escherichia coli by acoustic fields. *Scientific reports*, 8(1):4668, 2018.

[194] Paul N Danese, Leslie A Pratt, Simon L Dove, and Roberto Kolter. The outer membrane protein, antigen 43, mediates cell-to-cell interactions within escherichia coli biofilms. *Molecular microbiology*, 37(2):424–432, 2000.

[195] JOHN S Parkinson. Complementation analysis and deletion mapping of escherichia coli mutants defective in chemotaxis. *Journal of bacteriology*, 135(1):45–53, 1978.

[196] Jorge González-Gutiérrez, JL Carrillo-Estrada, and JC Ruiz-Suárez. Nucleation, aggregation, annealing, and disintegration of granular clusters. *Physical Review E*, 89(5):052205, 2014.

[197] Jörn Dunkel, Sebastian Heidenreich, Knut Drescher, Henricus H Wensink, Markus Bär, and Raymond E Goldstein. Fluid dynamics of bacterial turbulence. *Physical review letters*, 110(22):228102, 2013.

[198] R. W. Nash, R. Adhikari, J. Tailleur, and M. E. Cates. Run-and-tumble particles with hydrodynamics: Sedimentation, trapping, and upstream swimming. *Phys. Rev. Lett.*, 104:258101, Jun 2010.

[199] Harold C Slavkin. Biofilms, microbial ecology and antoni van leeuwenhoek. *The Journal of the American Dental Association*, 128(4):492–495, 1997.

[200] Enrique Hernández-Jiménez, Rosa del Campo, Victor Toledano, Maria Teresa Vallejo-Cremades, Aurora Muñoz, Carlota Largo, Francisco Arnalich, Francisco García-Rio, Carolina Cubillos-Zapata, and Eduardo López-Collazo. Biofilm vs. planktonic bacterial mode of growth: Which do human macrophages prefer? *Biochemical and biophysical research communications*, 441(4):947–952, 2013.

[201] Hans-Curt Flemming, Thomas R Neu, and Daniel J Wozniak. The eps matrix: the "house of biofilm cells". *Journal of bacteriology*, 189(22):7945–7947, 2007.

[202] Bruce E Rittmann. Biofilms in the water industry. In *Microbial biofilms*, pages 359–378. American Society of Microbiology, 2004.

[203] Hongyue Dang and Charles R Lovell. Microbial surface colonization and biofilm development in marine environments. *Microbiology and Molecular Biology Reviews*, 80(1):91–138, 2016.

[204] U Münster, E Heikkinen, and J Knulst. Nutrient composition, microbial biomass and activity at the air–water interface of small boreal forest lakes. *Hydrobiologia*, 363(1-3):261–270, 1997.

[205] Thomas Schwartz, Wolfgang Kohnen, Bernd Jansen, and Ursula Obst. Detection of antibiotic-resistant bacteria and their resistance genes in wastewater, surface water, and drinking water biofilms. *FEMS microbiology ecology*, 43(3):325–335, 2003.

[206] KN Kragh, JB Hutchison, G Melaugh, C Rodesney, AE Roberts, Y Irie, PØ Jensen, SP Diggle, RJ Allen, V Gordon, et al. Role of multicellular aggregates in biofilm formation. mbio 7: e00237-16, 2016.

[207] Minyoung Kevin Kim, Knut Drescher, On Shun Pak, Bonnie L Bassler, and Howard A Stone. Filaments in curved streamlines: rapid formation of staphylococcus aureus biofilm streamers. *New journal of physics*, 16(6):065024, 2014.

[208] Zbigniew Lewandowski and Paul Stoodley. Flow induced vibrations, drag force, and pressure drop in conduits covered with biofilm. *Water Science and Technology*, 32(8):19–26, 1995.

[209] Roberto Rusconi, Sigolene Lecuyer, Laura Guglielmini, and Howard A Stone. Laminar flow around corners triggers the formation of biofilm streamers. *Journal of The Royal Society Interface*, 7(50):1293–1299, 2010.

[210] Carla CCR de Carvalho. Marine biofilms: A successful microbial strategy with economic implications. *Frontiers in Marine Science*, 5:126, 2018.

[211] Yong-Gyun Jung, Jungil Choi, Soo-Kyoung Kim, Joon-Hee Lee, and Sunghoon Kwon. Embedded biofilm: a new biofilm model based on the embedded growth of bacteria. *Applied and environmental microbiology*, pages AEM–02311, 2014.

[212] Margaret C Henk. Capturing air–water interface biofilms for microscopy and molecular analysis. In *Microbial Biofilms*, pages 301–322. Springer, 2014.

[213] Suresh Neethirajan, David Karig, Aloke Kumar, Partha P Mukherjee, Scott T Retterer, and Mitchel J Doktycz. Biofilms in microfluidic devices. In *Encyclopedia of Nanotechnology*, pages 213–219. Springer, 2012.

[214] Marvin Whiteley, M Gita Bangera, Roger E Bumgarner, Matthew R Parsek, Gail M Teitzel, Stephen Lory, and EP Greenberg. Gene expression in pseudomonas aeruginosa biofilms. *Nature*, 413(6858):860, 2001.

[215] Arthur Prindle, Jintao Liu, Munehiro Asally, San Ly, Jordi Garcia-Ojalvo, and Gürol M Süel. Ion channels enable electrical communication in bacterial communities. *Nature*, 527(7576):59, 2015.

[216] Jintao Liu, Arthur Prindle, Jacqueline Humphries, Marçal Gabalda-Sagarra, Munehiro Asally, D Lee Dong-yeon, San Ly, Jordi Garcia-Ojalvo, and Gürol M Süel. Metabolic co-dependence gives rise to collective oscillations within biofilms. *Nature*, 523(7562):550, 2015.

[217] Marianne Sunde and Madelaine Norström. The genetic background for streptomycin resistance in escherichia coli influences the distribution of mics. *Journal of Antimicrobial Chemotherapy*, 56(1):87–90, 2005.

[218] Frederick R Blattner, Guy Plunkett, Craig A Bloch, Nicole T Perna, Valerie Burland, Monica Riley, Julio Collado-Vides, Jeremy D Glasner, Christopher K Rode, George F Mayhew, et al. The complete genome sequence of escherichia coli k-12. *science*, 277(5331):1453–1462, 1997.

[219] David van Duin and David L Paterson. Multidrug-resistant bacteria in the community: trends and lessons learned. *Infectious Disease Clinics*, 30(2):377–390, 2016.

[220] Verena Maria Suchanek. *Role of Motility and its Regulation in Escherichia coli Biofilm formation*. PhD thesis, 2017.

[221] Ronn S Friedlander, Nicolas Vogel, and Joanna Aizenberg. Role of flagella in adhesion of escherichia coli to abiotic surfaces. *Langmuir*, 31(22):6137–6144, 2015.

[222] Thomas J Silhavy, Daniel Kahne, and Suzanne Walker. The bacterial cell envelope. *Cold Spring Harbor perspectives in biology*, page a000414, 2010.

[223] Stephanie Brown, John P Santa Maria Jr, and Suzanne Walker. Wall teichoic acids of gram-positive bacteria. *Annual review of microbiology*, 67:313–336, 2013.

[224] Olga E Petrova and Karin Sauer. Sticky situations-key components that control bacterial surface attachment. *Journal of bacteriology*, pages JB–00003, 2012.

[225] Trevor Roger Garrett, Manmohan Bhakoo, and Zhibing Zhang. Bacterial adhesion and biofilms on surfaces. *Progress in Natural Science*, 18(9):1049–1056, 2008.

[226] L McLandsborough, A Rodriguez, D Pérez-Conesa, and J Weiss. Biofilms: at the interface between biophysics and microbiology. *Food Biophysics*, 1(2):94–114, 2006.

[227] Jacob N Israelachvili. Van der waals forces in biological systems. *Quarterly reviews of biophysics*, 6(4):341–387, 1973.

[228] Malte Hermansson. The dlvo theory in microbial adhesion. *Colloids and Surfaces B: Biointerfaces*, 14(1-4):105–119, 1999.

[229] Robert Belas. Biofilms, flagella, and mechanosensing of surfaces by bacteria. *Trends in microbiology*, 22(9):517–527, 2014.

[230] Olivier Vidal, Robert Longin, Claire Prigent-Combaret, Corinne Dorel, Michel Hooreman, and Philippe Lejeune. Isolation of an escherichia coli k-12 mutant strain able to form biofilms on inert surfaces: involvement of a new ompr allele that increases curli expression. *Journal of bacteriology*, 180(9):2442–2449, 1998.

[231] Adrian L Cookson, William A Cooley, and Martin J Woodward. The role of type 1 and curli fimbriae of shiga toxin-producing escherichia coli in adherence in abiotic surfaces. *International Journal of Medical Microbiology*, 292(3/4):195, 2002.

[232] Hannah H Tuson and Douglas B Weibel. Bacteria–surface interactions. *Soft matter*, 9(17):4368–4380, 2013.

[233] Hans-Curt Flemming and Jost Wingender. The biofilm matrix. *Nature Reviews Microbiology*, 8(9):623, 2010.

[234] George A O'toole and Roberto Kolter. Flagellar and twitching motility are necessary for pseudomonas aeruginosa biofilm development. *Molecular microbiology*, 30(2):295–304, 1998.

[235] Leslie A Pratt and Roberto Kolter. Genetic analyses of bacterial biofilm formation. *Current opinion in microbiology*, 2(6):598–603, 1999.

[236] Mikkel Klausen, Arne Heydorn, Paula Ragas, Lotte Lambertsen, Anders Aaes-Jørgensen, Søren Molin, and Tim Tolker-Nielsen. Biofilm formation by pseudomonas aeruginosa wild type, flagella and type iv pili mutants. *Molecular microbiology*, 48(6):1511–1524, 2003.

[237] Thomas K Wood, Andrés F González Barrios, Moshe Herzberg, and Jintae Lee. Motility influences biofilm architecture in escherichia coli. *Applied microbiology and biotechnology*, 72(2):361–367, 2006.

[238] Emma Tabe Eko Niba, Yoshiaki Naka, Megumi Nagase, Hirotada Mori, and Madoka Kitakawa. A genome-wide approach to identify the genes involved in biofilm formation in e. coli. *DNA research*, 14(6):237–246, 2007.

[239] Ken F Jarrell and Mark J McBride. The surprisingly diverse ways that prokaryotes move. *Nature Reviews Microbiology*, 6(6):466–476, 2008.

[240] Daniel B Kearns. A field guide to bacterial swarming motility. *Nature Reviews Microbiology*, 8(9):634, 2010.

[241] Berenike Maier and Gerard CL Wong. How bacteria use type iv pili machinery on surfaces. *Trends in microbiology*, 23(12):775–788, 2015.

[242] Leslie A Pratt and Roberto Kolter. Genetic analysis of escherichia coli biofilm formation: roles of flagella, motility, chemotaxis and type i pili. *Molecular microbiology*, 30(2):285–293, 1998.

[243] Urs Jenal and Jacob Malone. Mechanisms of cyclic-di-gmp signaling in bacteria. *Annu. Rev. Genet.*, 40:385–407, 2006.

[244] Regine Hengge. Principles of c-di-gmp signalling in bacteria. *Nature Reviews Microbiology*, 7(4):263, 2009.

[245] Ute Römling, Michael Y Galperin, and Mark Gomelsky. Cyclic di-gmp: the first 25 years of a universal bacterial second messenger. *Microbiology and Molecular Biology Reviews*, 77(1):1–52, 2013.

[246] Joerg Overhage, Shawn Lewenza, Alexandra K Marr, and Robert EW Hancock. Identification of genes involved in swarming motility using a pseudomonas aeruginosa pao1 mini-tn5-lux mutant library. *Journal of bacteriology*, 189(5):2164–2169, 2007.

[247] Michael J Pehl, William David Jamieson, Karen Kong, Jessica L Forbester, Richard J Fredendall, Glenn A Gregory, Jacob E McFarland, Jessica M Healy, and Paul M Orwin. Genes that influence swarming motility and biofilm formation in variovorax paradoxus eps. *PloS one*, 7(2):e31832, 2012.

[248] Sarah B Guttenplan and Daniel B Kearns. Regulation of flagellar motility during biofilm formation. *FEMS microbiology reviews*, 37(6):849–871, 2013.

[249] J William Costerton, GG Geesey, and K-J Cheng. How bacteria stick. *Scientific American*, 238(1):86–95, 1978.

[250] GG Geesey, WT Richardson, HG Yeomans, RT Irvin, and JW Costerton. Microscopic examination of natural sessile bacterial populations from an alpine stream. *Canadian Journal of Microbiology*, 23(12):1733–1736, 1977.

[251] David Lebeaux, Ashwini Chauhan, Olaya Rendueles, and Christophe Beloin. From in vitro to in vivo models of bacterial biofilm-related infections. *Pathogens*, 2(2):288–356, 2013.

[252] Tom Coenye and Hans J Nelis. In vitro and in vivo model systems to study microbial biofilm formation. *Journal of microbiological methods*, 83(2):89–105, 2010.

[253] Andrew J McBain. In vitro biofilm models: an overview. *Advances in applied microbiology*, 69:99–132, 2009.

[254] JD Rudney, R Chen, P Lenton, J Li, Y Li, RS Jones, C Reilly, AS Fok, and C Aparicio. A reproducible oral microcosm biofilm model for testing dental materials. *Journal of applied Microbiology*, 113(6):1540–1553, 2012.

[255] Ruth E Berry, David J Klumpp, and Anthony J Schaeffer. Urothelial cultures support intracellular bacterial community formation by uropathogenic escherichia coli. *Infection and immunity*, 77(7):2762–2772, 2009.

[256] James N Wilking, Vasily Zaburdaev, Michael De Volder, Richard Losick, Michael P Brenner, and David A Weitz. Liquid transport facilitated by channels in bacillus subtilis biofilms. *Proceedings of the National Academy of Sciences*, 110(3):848–852, 2013.

[257] Young Wook Kim, Sowmya Subramanian, Konstantinos Gerasopoulos, Hadar Ben-Yoav, Hsuan-Chen Wu, David Quan, Karen Carter, Mariana T Meyer, William E Bentley, and Reza Ghodssi. Effect of electrical energy on the efficacy of biofilm treatment using the bioelectric effect. *npj Biofilms and Microbiomes*, 1:15016, 2015.

[258] Silvio D Brugger, Christian Baumberger, Marcel Jost, Werner Jenni, Urs Brugger, and Kathrin Mühlemann. Automated counting of bacterial colony forming units on agar plates. *PloS one*, 7(3):e33695, 2012.

[259] Michelle M Barnhart and Matthew R Chapman. Curli biogenesis and function. *Annu. Rev. Microbiol.*, 60:131–147, 2006.

[260] Alexandre P Solon, Y Fily, Aparna Baskaran, Mickael E Cates, Y Kafri, M Kardar, and J Tailleur. Pressure is not a state function for generic active fluids. *Nature Physics*, 11(8):673, 2015.

[261] Martin Gröschl. Ultrasonic separation of suspended particles-part i: Fundamentals. *Acta Acustica united with Acustica*, 84(3):432–447, 1998.

[262] G Thalhammer, R Steiger, M Meinschad, M Hill, S Bernet, and M Ritsch-Marte. Combined acoustic and optical trapping. *Biomedical optics express*, 2(10):2859–2870, 2011.

[263] Sukant Garg, He Huifu, Sunil C Kaul, and Renu Wadhwa. Integration of conventional cell viability assays for reliable and reproducible read-outs: experimental evidence. *BMC research notes*, 11(1):403, 2018.

[264] Irith Wiegand, Kai Hilpert, and Robert EW Hancock. Agar and broth dilution methods to determine the minimal inhibitory concentration (mic) of antimicrobial substances. *Nature protocols*, 3(2):163, 2008.

[265] Shriti Singh, Santosh Kumar Singh, Indrajit Chowdhury, and Rajesh Singh. Understanding the mechanism of bacterial biofilms resistance to antimicrobial agents. *The open microbiology journal*, 11:53, 2017.

Appendix A

Viability essays

There are different methods to determine the number of micro-organisms that are present in a given population. This can be accomplished by using the spectrophotometer to measure the optical density of the population [192], by directly counting the microorganisms using a haemocytometer [263], or by serial diluting the bacteria and plating on media that supports the growth of the microorganisms [263]. The latter method is somewhat more time consuming, but provides statistically accurate and repeatable results. This method is also the ideal method for enumerating microorganisms in a given population because it only identifies the living organisms in that population. After the confinement of bacteria cells we used serial dilutions, plating and counting the number of colony forming units (CFU's) to determine the number of bacteria present in our cavity and their viability. In other words, we checked if the interaction with acoustic waves damages the cell, either by disrupting its membrane or producing a side effect due to the environmental stress.

To this end, the treated cells were recollected and saved in an 1 ml Eppendorf tube, this suspension contains an unknown number of bacteria. The same was done for the control resonator which contains cells that were not exposed to the acoustic wave. The collected volume contains n_0 colony forming units (CFU). Before we started diluting, we prepared k_1^i dilution blanks, which are Eppendorf tubes containing α ml of the diluting liquid. The first step is to gently shake or swirl the tube containing the recollected cells. This will ensure that the cells are evenly distributed because if the cells settle to the bottom, the number of cells that we get via pipetting is not enough invalidating the final count. Once swirled 100 µl of the collected inoculum were added to 900 µl of diluting liquid in the next tube k_2. This is a 1 in 10 dilution, this step is repeated up to k_i where i is the total number of dilutions.Later, after swirling all the Eppendorf tubes, we took a fraction β=100 µl of the total volume (1 ml) and spread it on agar plates– this means that only 10% of the volume is plated as in Figure A.1.

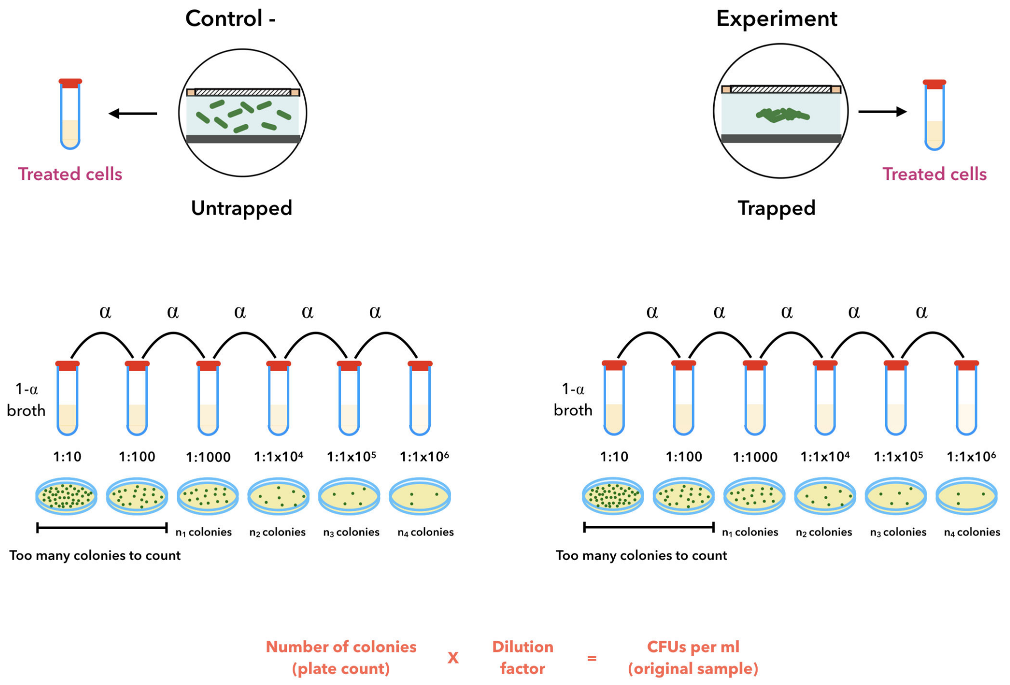

Fig. A.1 The serial dilution method is employed to estimate the concentration of bacteria by counting the number of colonies cultured from the dilutions of the inoculum and then back tracked the measured counts to the initial concentration. In this work, for every experiment we use an inoculated resonator-same geometry and inoculated protocol- that is not exposed to ultrasonic waves as a negative control and a resonator where the cells are exposed to acoustic waves as the experiment. In the experiment resonator the bacterial cells are trapped, following the protocol described earlier, and after the acoustic input is turned off, the incoculum is pipetted from the cavity and placed in an Eppendorf tube (Treated cells tube in the figure). The collected volume contains n_0 colony forming units (CFU), later a series of k dilutions are made sequentially each with a dilution factor α. From each of the k dilutions a fraction β is taken and spread on agar plates where colonies are counted. Let's consider the first tube in the figure (either the control - or the experiment) where the first dilution $\alpha = 10$ indicates a 10-fold dilutions i.e. by diluting 100 µm of the collected inoculum into 900 µm of media; and $\beta = 100$ means that only 10% of the volume is plated. In our case we make plating triplicates for each dilution.

Appendix B

Minimum inhibitory concentration

The aim of the broth dilution method know as minimal inhibitory concentration (MIC) is to determine the lowest concentration of the assayed antimicrobial agent that, under defined test conditions, inhibits the visible growth of the bacteria being investigated [264]. In this work, MIC values are used to determine both the susceptibility of *Escherichia coli* to gentamicin (gen) and whereas the clumped cells, due to acoustic forces, present a higher tolerance to the antibiotic.

It is known that one of the main characteristics of the cells in biofilms is the decrease of susceptibility to antibiotics [265], therefore, a difference in MIC values for cells trapped acoustically and not trapped could implicate the formation mediated via acoustic forces of free-floating biofilm-like structures.

To determine the MIC, overnight liquid cultures in LB broth were made for each of the model strains, at 30° and 250 rpm rotatory shaking. A fresh culture, under the same culture conditions, was re-started until it reached mid-exponential phase ($OD_{600nm} = 0.05$). Later the suspension was diluted 5000 times to have a suitable sample for inoculation. A 96-well plate was done per strain.

As always, the manipulation of microorganisms was performed in a sterile zone, either in a laminar flow hood or in the bench using a Bunsen burner to create a sterile zone. Later, a 96-well U-Bottom plate was inoculated with 100 µl from the second to the last column. Afterwards the first column was inoculated with 180 µl. From the gentamicin stock solution (10X), that was prepared beforehand and stored in the proper temperature, 20 µl were added to the first column of the plate. Using a multichannel pipette, the antibiotic and the cells were mixed gingerly by sucking up-and-down six times.

Next, 100 µl from the first column were transferred to the second one (this is a two-fold dilution for column one), the pipette tips were ejected and with new and sterile pipette tips the wells in column two were carefully mixed. The procedure was repeated down to the 11th column, the volume coming from this column was discarded, i.e. the 100 µ*l* were not added to the 12th column as shown in Figure B.1. Finally, the plate was incubated overnight at 30°.

Notice that in this protocol the first column is a positive control, where bacteria are treated with the highest dose of antibiotic, and the 12th column is the negative control as bacteria are not treated with antibiotics. This precise method of susceptibility testing allows for quantification of the exact concentration (in µg/ml) of the antibiotic.

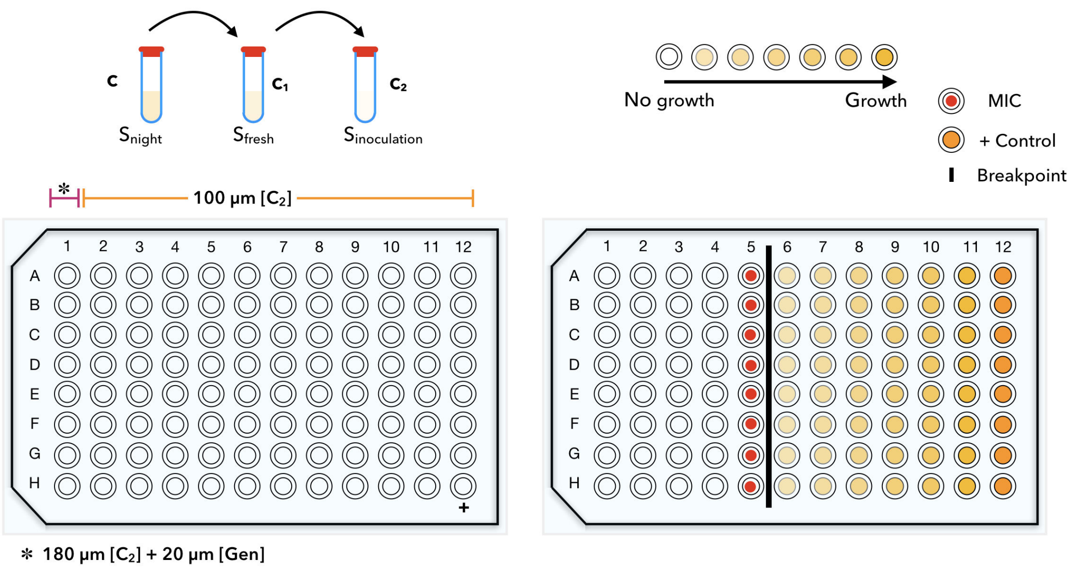

Fig. B.1 **Minimal Inhibitory Concentration**. MIC testing allows for quantification of the exact antibiotic concentration, in µg/ml, needed to inhibit bacteria growth. The figure shows a typical 96-well plate, used for MIC assays, divided in twelve columns for micro-dilutions and eight rows normally used for replicates. To test the susceptibility to gentamicine of the strains we used throughout this work, wells 2 to 12 are inoculated with $100\mu l$, whereas the volume for the first well is 180 µl. Next, 20µl of gentamicine at 1 mg/ml is deposited in the first well and mixed gingerly. Later 100 µl were transfered into the second well and mixed gently, the transfer procedure to one well to the following was done up to the 11th-the volume coming from this well is discarded. Column 12 serves as a positive control i.e. the cells are not treated with antibiotic. Finally the plate is incubated overnight at 30°. The figure on the right illustrates a plate after incubation, where the white circles represent no bacteria growth, meaning the antibiotic succeeded in inhibiting the bacteria growth for a given concentration. The yellow circles depict bacteria growth, where the light shades indicate less growth and the darker shades more growth. The darkest one (column 12) is the positive control that is used to validate the test. The vertical black line represents the breakpoint-concentration at which the bacteria are no longer susceptible to the antimicrobial but become resistant. The red point indicates the MIC value i.e., the lowest concentration at which the bacteria are susceptible to gentamicine.